To the Graduate Council:
I am submitting herewith a dissertation written by Alaska Subedi entitled "Interplay between structure and chemistry of materials and their physical properties." I have examined the final paper copy of this dissertation for form and content and recommend that it be accepted in partial fulfillment of the requirements for the degree of Doctor of Philosophy, with a major in Physics.

_____

George Siopsis, Major Professor

We have read this dissertation
and recommend its acceptance:

_____

David J. Singh

_____

John J. Quinn

_____

Takeshi Egami

Accepted for the Council:

_____

Carolyn R. Hodges

Vice Provost and Dean of the Graduate School

To the Graduate Council:
I am submitting herewith a dissertation written by Alaska Subedi entitled "Interplay between structure and chemistry of materials and their physical properties." I have examined the final electronic copy of this dissertation for form and content and recommend that it be accepted in partial fulfillment of the requirements for the degree of Doctor of Philosophy, with a major in Physics.

George Siopsis, Major Professor

We have read this dissertation
and recommend its acceptance:

David J. Singh

John J. Quinn

Takeshi Egami

Accepted for the Council:

Carolyn R. Hodges

Vice Provost and Dean of the Graduate School

(Original signatures are on file with official student records.)

Interplay between structure and chemistry of materials and their physical properties

A Dissertation

Presented for the

Doctor of Philosophy

Degree

The University of Tennessee, Knoxville

Alaska Subedi

August 2010

© by Alaska Subedi, 2010

All Rights Reserved.

Acknowledgements

I wish to thank my advisor Dr. David J. Singh for his kindness, patience and generosity. Despite his astonishingly high productivity and many responsibilities at the lab, he has always been available for discussions and questions. I have benefited greatly from these discussions and hope that his simple approach and intuitive insight to physics problems have rubbed off on me.

I also admire and thank David for giving me complete freedom to organize my research. He suggested interesting problems that would be nice to solve, but never asked me to work on a particular project. He also rarely inquired about the progress on my projects even though I talked to him almost every day he was at the lab. This encouraged me to be more independent and responsible. However, this also led me to develop one undesirable habit — I usually went to bed after four in the morning and rarely came to work before noon.

My friends at the university and Oak Ridge lab have also made the last four years enjoyable. Thank you Markus, Di, Aurelian, Shigeyuki, Hiroyuki, Andrew, Valentino and Mao-Hua for discussions and explanations, which were not always about physics. Thank you Laurene for making me chocolate mousse that helped maintain a steady supply of sugar to my brain while I wrote the thesis.

Finally, I would like to thank my parents for their encouragement and support. I also thank my sister for her love and affection. Without the strong support of my family, even from two oceans away in Nepal, this work would not have been possible.

Abstract

First principles calculations provide a powerful tool for sorting out the interplay of chemical composition and structure with the physical properties of materials. In this dissertation, I discuss the physical properties and their microscopic basis within this framework for following illustrative examples. (i) The Zintl phase hydrides, where I find H is anionic and the formation of covalent sp^2 bonds in the Al/Ga/Al-Si planes, which is a highly unusual bonding configuration for these elements. (ii) PbTe, which shows strong coupling between the longitudinal acoustic and transverse optic modes that may explain its low thermal conductivity. (iii) The double perovskites $BiPbZnNbO_6$ and $BiSrZnNbO_6$, where introducing size disorder at A-site prevents the BO_6 octahedra from tiling and enhances the polar behavior. (iv) FeSe, which shares the salient electronic and magnetic features of other Fe superconductors and cannot be described as a conventional electron phonon superconductor. (v) $NbFe_2$, which is near a magnetic quantum critical point and shows strong competition between various magnetic orderings that may explain its unusual non-Fermi liquid behavior at very low temperatures. (vi) The nickel analogues of Fe superconductors LaNiPO and $BaNi_2As_2$, where I show that superconductivity is of conventional electron-phonon type in contrast to the Fe-based superconductors. (vii) Noncentrosymmetric $LaNiC_2$, which I find is a conventional electron-phonon superconductor with intermediate coupling.

Contents

List of Tables

List of Figures

Chapter 1

Introduction

The structure of materials plays a major role in determining their properties. For example, diamond and graphite have very different properties even though they are both composed of carbon. Diamond, which has a face centered cubic structure, is an insulator and transparent to light. Graphite, however, has a hexagonal structure and is an electrical conductor and opaque to light. Similarly, small variations in chemical composition of a material can also have major effects on its physical properties. The high temperature cuprate superconductors are well known examples of sensitivity to chemistry. The parent compounds are insulators but they become superconducting when doped.

Understanding how various physical properties of materials derive from their structure and chemical composition has proven to be one of the most important and difficult challenges in physics and chemistry. There are many examples that illustrate the strong connection between the structure and physical properties of materials. A large number of ferroelectric materials have a perovskite structure. The filled skutterudites $CeFe_{4-x}Co_xSb_{12}$ and $LaFe_{4-x}Co_xSb_{12}$ have low thermal conductivity and high values thermoelectric figure of merit. The high temperature cuprate superconductors have a layered perovskite structure. It would be of

great value to resolve the role of the structure of materials in governing their properties such as thermal conductivity, ferroelectricity and superconductivity. Does the structure of a material play a fundamental role? This might be the case in the unconventional superconductor FeSe which is superconducting in the tetragonal structure but becomes non-magnetic semiconductor when transformed to a hexagonal structure with the application of high pressure. On the other hand, a large and complex structure does not seem to be a prerequisite for a material to have low thermal conductivity. PbTe exists in a simple face centered cubic structure but has a low thermal conductivity of 2.3 W/(m K).

In the other direction, once we know how the structure influences certain physical features, can we devise mechanisms to finely tune the structure and produce new materials with those features highly enhanced? In Chapter 5, we will find that the lattice instabilities of perovskite oxides ABO_3 can be understood using the tolerance factor, which is a simple function of ionic radii of the constituent elements. When the tolerance factor is less than 1, there are two possibilities for lattice distortions — either the BO_6 octahedra are tilted or, rarely, the ion at A-site off-centers to form a ferroelectric. However, we can prevent the octahedra from tilting and instead induce the ion at A-site to off-center by introducing size disorder at the A-site.

Furthermore, once we understand the interplay between structure and physical properties, is it possible to formulate principles and methods to design materials with desired characteristics? Some of the most challenging problems in condensed matter physics are developing room temperature superconductors, thermoelectrics with figure of merit that is greater than 3, materials with strongly coupled ferroelectricity and ferromagnetism, and materials that are transparent and also have high electrical conductivity. Can we discover or design materials with these features?

To achieve these goals, we need to understand the interactions of electrons and nuclei in solids and their response to external influences. In principle we just need to solve the Schrodinger equation for the electrons and nuclei in solids. Unfortunately, this is impractical because of the strong nature of interaction between electrons and nuclei and, therefore, we need to use sufficiently accurate approximate methods.

My research uses approximations based on the density functional theory (DFT)[1, 2] to unravel the role of structure and chemistry on the physical properties of a material. Density functional theory is a first principles method that allows us to determine properties of materials using only their structure and chemical composition. This method makes the strongly interacting many body problem of electrons and nucleus in solids tractable by transforming it into an equivalent problem of noninteracting particles. This method enables us to see how the electrons in solids are arranged in real, momentum and spin spaces, and thus gives us a microscopic basis to explain various properties of solids. A brief overview of DFT will be given in the next chapter.

First principles calculations are useful in interpreting and clarifying experimental results. In addition, they can be used to study how certain properties of materials change when the structure and chemistry are varied. In a later chapter I will describe my calculations that show extreme sensitivity of certain phonon modes in PbTe to changes in the lattice parameter. I will also describe how the nature of superconductivity changes when Fe in $BaFe_2As_2$ is substituted by Ni. Similarly, DFT also enables us to do various gedanken experiments that would be difficult to perform in a laboratory. For example, we can study the effects of lattice expansion on ferroelectric materials by performing calculations at lattice parameters that are larger than the experimental value.

When we do measurements in the lab, we mainly observe the low energy excitations of the ground state of a material. However, in many cases we are unable to study competing phases that may be close to the ground state but not connected to it. Density functional theory makes it possible to study the states that are energetically close to the ground state and also the competition between these states as the chemistry and structure is varied. In a later chapter, I will describe competition between various magnetic orderings in $NbFe_2$ that may help explain its unusual non-Fermi liquid behavior at very low temperatures.

In a nutshell, we can easily use density functional theory to calculate the ground state electronic, magnetic and phonon properties of most materials. Unfortunately, such calculations do not always make obvious the underlying physics and the interactions that most dominate the physical properties. Most often, the way to understand the underlying physics and microscopic mechanism is by studying how the electronic, magnetic and phonon properties vary when we change chemical composition and structure. In this dissertation, I discuss the physical properties and their microscopic basis within this framework for the following illustrative examples.

The Zintl phase hydrides $SrAl_2H_2$, $BaGa_2H_2$, $SrGa_2H_2$ and SrAlSiH have a layered hexagonal structure.[3, 4, 5] One layer consists of Sr/Ba and H. Another layer is made up of hexagonal sheets of Al/Ga/Al-Si. Initial first principles studies of the electronic structure of these compounds suggested H is covalently bonded and part of a polyanionic network composed of Al/Ga/Al-Si.[4, 5] I studied how the electronic structure of these compounds changes when H is removed and/or replaced by F. I find that Ba and Sr are cationic while H is anionic. I also find the formation of covalent sp^2 bonds in the Al/Ga/Al-Si planes, which is a highly unusual bonding configuration for these elements.

PbTe has a simple and high symmetry rock salt structure, yet it has low thermal conductivity of 2.3 W/(m K).[6] In general, materials with large complex unit cells, and with rattling ions, such as filled clathrates have low thermal conductivity.[7] I studied the lattice dynamics of PbTe at various lattice parameters and found strong coupling between longitudinal acoustic and transverse optic modes that may explain its low thermal conductivity.

Many perovskite oxides ABO_3 show lattice instabilities that cause BO_6 octahedra to be tilted. However, according to first principles calculations, if the octahedra are prevented from tilting by mixing large and small A-site ions they may become ferroelectrics.[8] For example, recent experiments found that ferroelectricity in (Ba,Ca)TiO_3 solid solution is strongly enhanced compared to what would be expected interpolating between the properties of the end-point compounds.[9] Inspired by this finding, I studied the polar behavior of double perovskites $BiPbZnNbO_6$ and $BiSrZnNbO_6$ using first principles density functional calculations. I find strong ferroelectric distortion in both materials. The polarization of the Pb and Sr materials are 85 and 79 $\mu C/cm^2$, respectively, along the rhombohedral direction

After the initial discovery of superconductivity in LaFeAsO and $BaFe_2As_2$ in 2008,[10, 11] superconductivity was also found in much simpler FeSe.[12] Like other Fe superconductors, FeSe is made up of the structural motif of square planar sheets of Fe coordinated tetrahedrally by chalcogen anions. However, FeSe lacks the intercalating layers, which suggests the Fe layer drives much of the physics of these materials. I studied the electronic structure, magnetism and phonons of FeS, FeSe and FeTe, and found that these compounds share the salient features of Fe pnictide superconductors.

Nuclear magnetic resonance studies show that pure hexagonal C14 Laves phase $NbFe_2$ is a weak antiferromagnet below 13 K with magnetic moment per

Fe of no more than 0.1 μ_B.[13] However, the material becomes ferromagnetic by slight overdoping of either Nb or Fe, indicating the existence of a quantum critical point at or very close to stoichiometric $NbFe_2$.[14] I studied the total energy of $NbFe_2$ at various magnetic orderings to better understand the dominant magnetic interactions in pure $NbFe_2$. The magnetism is itinerant in the sense that the moments are highly dependent on ordering and go to zero for some configurations. There is an overestimation of the magnetic tendency within the local spin density approximation, similar to other metals near magnetic quantum critical points. I also find a competition between different magnetic states due to band-structure effects. These lead to competing magnetic tendencies due to competing interlayer interactions, one favoring a ferrimagnetic solution and the other an antiferromagnetic state.

As already mentioned, superconductivity was discovered in LaFeAsO, $BaFe_2As_2$, and related materials in 2008. Around the same time, superconductivity in their nickel analogues, including LaNiPO and $BaNi_2As_2$ was also discovered.[15] I found that electronic properties of the Ni superconductors are very different compared to the Fe superconductors because Ni contains two more electrons than Fe. This has the effect of moving the Ni superconductors further from magnetism and enhancing the electron-phonon coupling. The superconductivity in Ni compounds are readily explained by the conventional electron-phonon picture, unlike their Fe analogues.

$LaNiC_2$ forms in the base centered orthorhombic structure that lacks inversion symmetry.[16] It is superconducting at $T_c = 2.7$ K[17, 18] but experimental studies of specific heat that could help in determining the nature of superconductivity have so far been inconclusive. Lee *et al.*[17] found nonexponential decay of specific heat below T_c and based on this argued that $LaNiC_2$ is an unconventional superconductor. However, Pecharsky *et al.*[18] observed the usual exponential decay of specific heat below T_c, consistent with the conventional BCS superconductivity.

I performed first principles calculations of the electronic structure and electron-phonon coupling. My calculations show that the material is a conventional electron-phonon superconductor with intermediate coupling. I find there are large contributions to the coupling by two low frequency C nonbond-stretching modes, one of which has strong Kohn anomalies.

Chapter 2

Methods

We need to solve the following Hamiltonian to calculate the energy of a system from the first principles

$$\mathcal{H}\Psi = \left(-\frac{\hbar^2}{2m} \sum_i \nabla_i^2 - \sum_{i,I} \frac{Z_I e^2}{|\vec{r}_i - \vec{R}_I|} + \frac{1}{2} \sum_{i \neq j} \frac{e^2}{|\vec{r}_i - \vec{r}_j|} + \frac{1}{2} \sum_{I \neq J} \frac{Z_I Z_J e^2}{|\vec{R}_I - \vec{R}_J|} \right) \Psi \quad (2.1)$$

where lowercase subscripts denote electrons and uppercase subscripts denote nuclei with charge Z_I and mass M_I. Here we have ignored the kinetic energy of nuclei since nuclei are much more massive than electrons. However, a direct solution of this equation is computationally prohibitive for real-world systems that contain more than a few atoms.

Modern methods of solving the many-body Schrödinger equation, such as the density functional theory, rely on a theorem by Hohenberg and Kohn. They proved that the total energy of a system of interacting electrons in an external potential is a functional of the electron density.[1] This is helpful but the utility of this result depends on finding the form of the energy functional. The exact expression of the functional has still not been found, but a simple approximation for the energy

functional was provided by Kohn and Sham:[2]

$$\mathcal{E}[\rho] = T_s + \frac{e^2}{2}\int\int \frac{\rho(\vec{r})\rho(\vec{r}\,')}{|\vec{r}-\vec{r}\,'|}\mathrm{d}\vec{r}\mathrm{d}\vec{r}\,' + \int \rho(\vec{r})V_{\mathrm{ext}}(\vec{r})\mathrm{d}\vec{r} + \mathcal{E}_{\mathrm{xc}}[\rho] \tag{2.2}$$

where T_s is the kinetic energy functional of noninteracting electrons, ρ is the electron density, V_{ext} is the potential due to nuclei and any other external fields, and $\mathcal{E}_{\mathrm{xc}}$ is the unknown exchange-correlation functional that captures all electron interactions beyond that expressed by the second term in the equation (called the Hartree term). In the Kohn-Sham method, the electron density is expressed by a sum of non-interacting single particle ground state densities. Kohn and Sham showed that the correct ground state density of the interacting electrons is given by the Fermi sum

$$\rho(\vec{r}) = \sum_{occ} \psi_l^* \psi_l, \tag{2.3}$$

where ψ_l are the self-consistent solutions of the Kohn-Sham equations

$$\mathcal{E}_l\psi_l = \left\{T_s + e^2\int \frac{\rho(\vec{r}\,')}{|\vec{r}-\vec{r}\,'|}\mathrm{d}\vec{r}\,' + V_{\mathrm{ext}}(\vec{r}) + \frac{\delta\mathcal{E}_{\mathrm{xc}}[\rho]}{\delta\rho(\vec{r})}\right\}\psi_l. \tag{2.4}$$

The Kohn-Sham formalism is exact if we know the correct exchange-correlation functional. Unfortunately, the $\mathcal{E}_{\mathrm{xc}}$ is also unknown. However, there are simple approximations to it that give useful results. The simplest approximation is the local density approximation (LDA) where the functional depends only on a function of the local density. In LDA,

$$\mathcal{E}_{\mathrm{xc}}[\rho] = \int \epsilon_{\mathrm{xc}}[\rho]\rho(\vec{r})\mathrm{d}\vec{r}, \tag{2.5}$$

where $\epsilon_{\mathrm{xc}}[\rho]$ is the exchange-correlation energy per particle of a homogeneous system of density ρ. Other widely used approximations are the generalized gradient

approximations (GGA) where the functional depends also on the local gradient of the density, *i.e.* $\epsilon_{\rm xc} = \epsilon_{\rm xc}[\rho, |\nabla\rho|]$.

The Kohn-Sham formalism greatly reduces the complexity of the original problem. To make this formalism useful for applications, the next important consideration we have to make is the choice of basis upon which the eigenfunction and density are expanded. An efficient choice of basis set is crucial because a basis that can approximate the electron density using a minimal number of functions can reduce the computational complexity and increase the accuracy dramatically. The simplest basis is the set of planewaves. However, the potential is steeply decreasing near the nucleus which causes the electrons near the nucleus to be more localized and have larger mean kinetic energy. Therefore, we need a large number of planewaves to describe core electrons.

The pseudopotential method gets around this difficulty by replacing the strong core potential by a pseudopotential whose ground state wavefunctions match the all electron valence wavefunction outside some core radius. This method reduces the basis set by removing the core electrons as well as the orthogonalization wiggles in the valence electrons.

The linearized augmented planewave (LAPW) method gets around the problem in a different way.[19] In this method, space is divided into two regions: non-overlapping atom centered spheres and an interstitial region. Inside the spheres (S), radial solutions of Schrödinger equation and their first derivatives are used, while planewaves are employed in the interstitial region (I). The functions in the basis are of the form

$$\phi(\vec{r}) = \begin{cases} \Omega^{-1/2} \sum_{\vec{G}} c_{\vec{G}} e^{i(\vec{G}+\vec{k}).\vec{r}} & \vec{r} \in I \\ \sum_{lm} [A_{lm} u_l(r) + B_{lm} \dot{u}_l(r)] Y_{lm}(\hat{r}) & \vec{r} \in S, \end{cases} \tag{2.6}$$

where Ω is the cell volume, u_l is the solution of the radial Schrödinger equation, Y_{lm} is the spherical harmonic, $\vec{G}$ is the reciprocal lattice vector, and $c_{\vec{G}}$, A_{lm} and B_{lm} are the expansion coefficients.

Once we obtain self-consistent solutions of the Kohn-Sham equations, we can calculate the responses of solids to a small perturbation at a wavevector $\vec{q}$ using the linear response theory.[20] Let V^1_{ext} be a perturbation on the external potential. The lowest order variation of the unperturbed Kohn-Sham Hamiltonian is given by

$$\mathcal{H}^1(\vec{r}) = V^1_{ext}(\vec{r}) + e^2 \int \frac{\rho^1(\vec{r})}{|\vec{r} - \vec{r}'|} \mathrm{d}\vec{r}' + \int \frac{\delta V_{xc}}{\delta \rho(\vec{r}')} \rho^1(\vec{r}') \mathrm{d}\vec{r}', \tag{2.7}$$

where ρ^1 is the first order variation in the density. This is given by

$$\rho^1(\vec{r}) = \sum_{occ} [\psi^{1*}_i(\vec{r})\psi_i(\vec{r}) + \psi^*_i(\vec{r})\psi^1_i(\vec{r})], \tag{2.8}$$

where ψ^1 is the first order perturbation of Kohn-Sham orbitals due to V^1_{ext}. Since $\mathcal{H}^1$ and ρ^1 depend on each other, Eqns. 2.7 and 2.8 must be solved self-consistently.

We can apply the linear response theory to calculate electron-phonon matrix elements which can be used to calculate the superconducting T_c in the conventional electron-phonon scenario. This widely used framework was developed by Savrasov *et al.* and is described in detail in Ref. [21]. The matrix element for scattering of an electron in the state $|\mathbf{k}j\rangle$ to the state $|\mathbf{k}+\mathbf{q}j'\rangle$ via a phonon mode $\omega_{\mathbf{q}\nu}$ is given by

$$g^{\mathbf{q}\nu}_{\mathbf{k}+\mathbf{q}j',\mathbf{k}j} = \langle \mathbf{k}+\mathbf{q}j' | \delta^{\mathbf{q}\nu} V_{\mathrm{eff}} | \mathbf{k}j \rangle, \tag{2.9}$$

where $\delta^{\mathbf{q}\nu}V_{\text{eff}}$ is the perturbation potential. The phonon linewidth can be calculated using the Fermi golden rule and is given by

$$\gamma_{\mathbf{q}\nu} = 2\pi \sum_{\mathbf{k}jj'} |g^{\mathbf{q}\nu}_{\mathbf{k}+\mathbf{q}j',\mathbf{k}j}|^2 \delta(\varepsilon_{\mathbf{k}j} - \varepsilon_F)\delta(\varepsilon_{\mathbf{k}+\mathbf{q}j'} - \varepsilon_F), \tag{2.10}$$

where ε_F is the Fermi energy and $\varepsilon_{\mathbf{k}j}$ and $\varepsilon_{\mathbf{k}+\mathbf{q}j'}$ are the energies of the respective single particle states. This can be used to calculate the electron-phonon spectral distribution functions

$$\alpha^2F(\omega) = \frac{1}{2\pi N(\varepsilon_F)} \sum_{\mathbf{q}\nu} \frac{\gamma_{\mathbf{q}\nu}}{\omega_{\mathbf{q}\nu}} \delta(\omega - \omega_{\mathbf{q}\nu}), \tag{2.11}$$

where $N(\varepsilon_F)$ is the electronic density of states per atom per spin at the Fermi level. The electron-phonon coupling constant, which plays the role of BCS parameter $N(\varepsilon_F)V$, can be obtained using

$$\lambda = 2 \int \frac{\alpha^2F(\omega)}{\omega} \, \mathrm{d}\omega. \tag{2.12}$$

The superconducting T_c is calculated using the Allen-Dynes formula [22]

$$k_BT_c = \frac{\hbar\omega_{\ln}}{1.2} \exp\left\{-\frac{1.04(1+\lambda)}{\lambda - \mu^*(1+0.62\lambda)}\right\}, \tag{2.13}$$

where $\omega_{\ln}$ is the logarithmically averaged phonon frequency and μ^* is the effective screened Coulomb pseudopotential.

Obviously, the usefulness of these methods depends on their ability to reasonably explain the experimental results and illuminate the underlying physics that is responsible for various properties of materials. Over the last three decades, DFT based methods have been employed to study many materials and they have

achieved varying levels of success in determining their properties. However, the real utility of DFT based methods comes from their ability to calculate the arrangement of electrons in the momentum and spin spaces as it makes it possible to study underlying physics at the microscopic level. These electronic structure calculations have been key to better understanding of metals and insulators. Studying the changes in electronic structure when chemistry and structure are changed has given insight into the dominant interactions and underlying physics of many magnets, ferroelectrics and superconductors.

There have also been some glaring failures of DFT based methods and we need to have a good understanding of the limitations of these approximations to be able to confidently apply them. The cuprates and other transition metal oxides are one example where DFT based methods have so far been inadequate. The undoped cuprates are antiferromagnetic Mott insulators but are predicted to be paramagnetic metals within the LDA. In the cuprates, strong onsite Coulomb correlations induce a tendency towards localization and moment formation. This is not captured by the LDA which is parameterized to accurately capture the correlation in the regime of uniform electron density.

DFT based methods fail in another way in materials such as Ni_3Al and $Sr_3Ru_2O_7$ that are near a magnetic quantum critical point by overestimating their tendency towards magnetism. In these materials, the magnetic interaction is strongly renormalized by spin fluctuations, which reduce the inclination towards moment formation and ordering. This inaccuracy is related to the way the LDA is parameterized. The LDA accurately describes the exchange and correlation interactions in a uniform electron gas, which has been solved exactly by Ceperley and Alder.[23] Their calculations predict that the uniform electron gas is paramagnetic at high densities but becomes spin-polarized at a density less than 2×10^{20} cm^{-3}. When the density is decreased further below 2×10^{18} cm^{-3}, the electron

gas crystalizes in a body centered cubic structure known as the Wigner crystal. In metals, the electron density is usually much higher than 1×10^{21} cm^{-3}. For example, in bcc Fe, which is the prototypical ferromagnet, average electron density is 7×10^{23} cm^{-3}. In FeSe and $NbFe_2$, which we will discuss in Chapters 7 and 6, the average electron densities are 1×10^{24} cm^{-3} and 5×10^{23} cm^{-3}, respectively. At these value of electron density, the LDA behaves like a mean field theory and, therefore, does not take into account the spin fluctuations that are relevant to metals near a magnetic quantum critical point.

Chapter 3

Bonding in Zintl phase hydrides

A similar version of this chapter appeared as *"Bonding in Zintl phase hydrides: Density functional calculations for SrAlSiH, $SrAl_2H_2$, $SrGa_2H_2$, and $BaGa_2H_2$"*, Alaska Subedi and David J. Singh, Phys. Rev. B **78**, 045106 (2008)

3.1 Introduction

The electronic and chemical behavior of hydrogen in the solid state has been extensively studied and remains a very active area of research. This is due to fundamental interest in hydrogen chemistry and because of its technological importance, e.g. in passivating semiconductor defects, in metallurgy and in various niche applications such as hydrogen storage. In fact the chemistry of H is perhaps richer than that of any other element with the exception of C. Remarkably, this richness is related to the simplicity of the H atom itself, which consists of a single valence electron and no core electrons.[24] The absence of a core allows very short bond lengths between H and other elements. The one electron nature of H also leads to a great deal of chemical flexibility with ionization energy and electron affinity compatible with charge transfer in either direction depending

on the chemical environment. This underlies the amphoteric behavior of H in many semiconductors leading to its importance in passivating defects. In addition to behaving as a cation or an anion, H can participate in covalent and metallic bonding and also in so called H bonding. However, even in ionic situations, H is unlike other elements. For example, while the structure of many anionic hydrides have parallels in F chemistry,[25, 26] H^- is a much more flexible ion than F^-, e.g. in the range of bond lengths that it can take.[27, 28]

Thus the discovery of the first Zintl phase hydride, $SrAl_2H_2$, by Gingl and co-workers[3] attracted significant interest. This was followed by the discovery of additional members of this family: $SrGa_2H_2$, $BaGa_2H_2$ and SrSiAlH, as well as first principles studies of the electronic structures of these compounds.[4, 5] SrSiAlH is semiconducting in contrast to the other members of the family, which are metallic. In this chapter, we try to better elucidate the bonding of these compounds, and especially the role of hydrogen, based on density functional calculations. We find that the bonding has mixed character, which is characteristic of other Zintl type compounds. In particular that Ba and Sr are cationic while H is anionic, and that these ions provide charge balance to support covalent sp^2 bonds among the Al, Ga and Si atoms.

3.2 Method

The main results presented here are based on calculations of electronic structures and phonon frequencies in the various compounds and comparisons with model hypothetical compounds to elucidate the bonding. All the calculations were performed within density functional theory with the generalized gradient approximation (GGA) of Perdew, Burke and Ernzerhof (PBE).[29] The electronic structures and related quantities were obtained using the general potential

linearized augmented planewave (LAPW) method[19] as implemented in the WIEN2k code.[30] This is an all electron method that uses a flexible basis and makes no shape approximations to the potential and charge density. Significantly for the present study, the LAPW method uses a partitioning of space into atom centered spheres and an interstitial region, which as will be discussed facilitates analysis of bonding by providing a way of assigning the H contributions. Well converged basis sets were used with LAPW sphere radii of $2.2, 2.3, 2.1, 2.1, 2.15$ and 1.0 a_0 for Sr, Ba, Al, Si, Ga and H, respectively. The phonon dispersions were computed using linear response[20] as implemented in the quantum espresso package. [31] We used GGA ultrasoft pseudopotentials[32] with an energy cutoff of 40 Ry. Special attention was paid to the convergence of the grid that represents the charge density as is important when using ultrasoft pseudopotentials in phonon calculations. A $(6, 6, 6)$ grid was used for the Brillouin zone sampling. The atomic positions were separately relaxed at the experimental lattice parameters for use in calculation of phonon dispersions. There were no significant differences in relaxed positions obtained from the LAPW and pseudopotential calculations.

3.3 Structure

$SrAl_2H_2$, $BaGa_2H_2$ and $SrGa_2H_2$ occur in a hexagonal structure, spacegroup $P\bar{3}m1$, as shown in Fig. 3.1. The structure consists consists of triangular lattice sheets of Sr atoms and dimpled hexagonal sheets of Al atoms. H atoms occur close to the Sr plane in a dimpled hexagonal sheet so that alternating H atoms are closer to the Al either above or below the Sr plane, with the corresponding Al atom moving towards its nearest H. This leads to the formation of alternating short and long Al-H distances along the c-axis. This structure is closely related to the structure of intermetallic hydride $ZrBe_2H_x$, although as will be shown below the bonding is

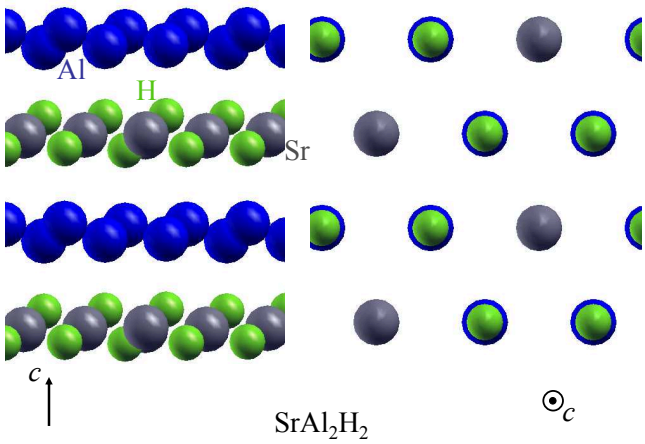

Figure 3.1: (color online) The crystal structure of $SrAl_2H_2$.

very different from the metallic bonding based on strong hybridization of Zr and Be states found in that material.[33, 34, 35, 36] The structure of SrAlSiH is similar to that of $SrAl_2H_2$ with the replacement of every other Al atom by Si, and removal of the H atom that was closest to the replaced Al, yielding a non-centrosymmetric $P3m1$ spacegroup.

The structures used in the present calculations are given in Table 3.1. The atomic positions were relaxed at the experimental lattice parameters, except as noted. These structures agree with prior determinations.[3, 4, 5] For example, the experimentally determined nearest neighbor Al-H distances in $SrAl_2H_2$ and SrAlSiH are 1.71 and 1.77 Å, respectively[3, 4], while the calculated values are 1.72 and 1.76 Å, respectively. It is noteworthy that the Al-H and Ga-H distances in these compounds range from 1.702 Å, in $BaGa_2H_2$ to 1.761 Å, in SrAlSiH. These distances are substantially longer than the sums of the covalent radii, which are 1.55 Å, for Al-H, and 1.63 Å, for Ga-H, and furthermore that the trend in the bond

Table 3.1: Structures of $ABB'X_n$, A=Sr,Ba, B=Al,Ga, B'=Al,Ga,Si, X=F,H, and $n = 0$ for KAlSi and SrAlSi, $n = 1$ for other B'=Si compounds, and $n = 2$ for B=B'=Al,Ga. The internal coordinates are from GGA structure relaxation, except for KAlSi, while the lattice parameters are from experimental data. d_{B-X} denotes the distance between the B and X atoms, e.g. the shortest Al-H bond length in $SrAl_2H_2$. "h" is used to denote hypothetical compounds.

	a(Å)	c(Å)	z_B	$z_{B'}$	z_X	d_{B-X}(Å)
$SrAl_2H_2$	4.528	4.722	0.4608		0.0964	1.721
$SrGa_2H_2$	4.401	4.711	0.4646		0.1026	1.705
$BaGa_2H_2$	4.533	4.907	0.4694		0.1226	1.702
SrAlSiH	4.214	4.955	0.5403	0.4454	0.8956	1.761
KAlSi (h)	4.214	4.955	0.5403	0.4454		
SrAlSiF (h)	4.214	4.955	0.5225	0.4401	0.9040	1.891
SrAlSi	4.215	4.770	0.4994	0.5005		

length between Al and Ga is opposite to the trend in the covalent radii of Al and Ga.*

3.4 Electronic Structure of SrAlSiH

We start our discussion with SrAlSiH. The electronic density states (DOS) of this material is shown in Fig. 3.2, along with the projection onto the H LAPW sphere. The corresponding band structure is shown in the left panel of Fig. 3.3. We find a band structure similar to that reported previously, and in particular there is a modest semiconducting gap in agreement with prior results.[4, 37] The lowest band shown, centered at -8 eV with respect to the valence band maximum is of mixed Si s and Al s character. The next band, which extends from ~ -6 eV to ~ -4 eV is H s derived and accounts for the great majority of the H s character seen in the valence bands. The three remaining occupied bands, extending up to the valence

*Here we use the usual covalent radii of Al, Ga, and H of 1.18 Å, 1.26 Å, and 0.37 Å, based on non-polar compounds and in particular the H_2 molecule for H. Generally polar bonds will be shorter, and in fact a value of 0.30Å, for H is often used, e.g. Ref. [24].

band edge, are two bands of mixed Si p and Al p character, and one band of mainly Si p_z character (p_z is the p orbital directed along the c-axis while p_x and p_y are the p orbitals directed in the Si-Al plane). The conduction bands have mixed character of mainly Al s, and Al and Si p character. As may be seen, the character within the H LAPW sphere is almost entirely located below the Fermi energy, and in particular there is practically no H s character to the DOS above E_F. The nominal occupied band electron counting is then, two H s electrons filling the H s orbital, two Al/Si s electrons, for average half filling of the Al/Si s orbitals, four Al/Si p_x/p_y electrons, for half filling of those orbitals, and two Si p_z electrons, filling that shell. This electronic structure is then consistent with a view in which there are covalent bonds between Al and Si, in particular σ bonding of sp^2 hybrids, while the Sr is close to a Sr^{2+} cation, as might be expected, and H occurs as the H^- anion. In addition, the electronic structure is consistent with the existence of weaker Si p_z - Al p_z π bonding, but the present results are not sufficient for analyzing this in detail. In this picture there are not substantial covalent bonds between Al and H.

In order to better define this picture in relation to an alternate scenario with largely covalent Al-H interactions, we begin with projected density of states. Qualitatively, the feature of having little H s character above the Fermi energy is similar to what is found in model compounds with anionic H, in particular tetragonal MgH_2[38] and face centered cubic LiH[39, 40]. This is in contrast to more covalent systems where antibonding states with significant H character can generally be found in the unoccupied spectrum. In hydrogen anion based materials, the H^- ion is stabilized by the Ewald field. Thus we consider an ionic model, based on the charge density of a H^- ion stabilized by the Ewald field, as simulated by a Watson sphere of radius 2.0 a_0.[41] For such a H^- ion in the local density approximation, the charge inside the muffin tin radius of 1.0 a_0 is 0.482e. Dividing

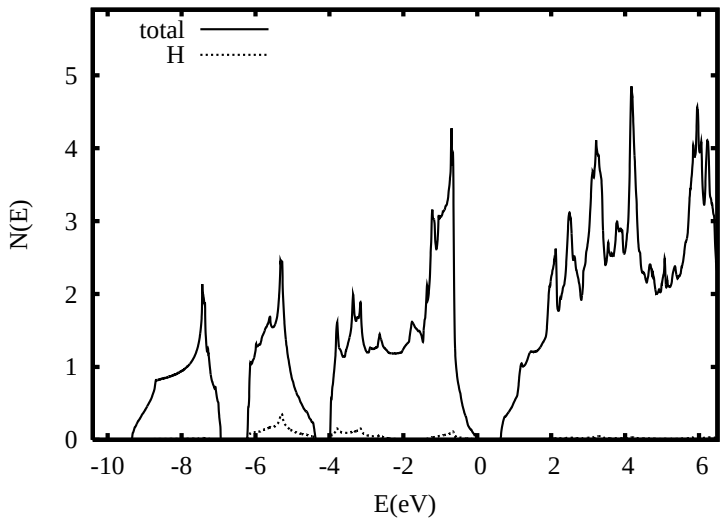

Figure 3.2: Electronic density of states of SrAlSiH, and projection onto the H LAPW sphere.

the integrated DOS of H below the Fermi energy (0.460) by $0.482e/2$ gives $1.910e$. Thus, we can infer that H acquires an electron to fill its $1s$ orbital.

It is helpful to compare the band structure of SrAlSiH (Fig. 3.3) in relation to real and hypothetical model compounds in order to gain further insight into the bonding. First we consider SrAlSi, whose band structure is shown in Fig. 3.4. This band structure is qualitatively very similar to that of SrAlSiH (Fig. 3.3) except for the missing H s derived band and an upward shift of the Fermi energy by one electron in the non-hydrogen containing compound, and is close to that obtained previously.[42, 43, 44] This implies that the bonding nature of Al and Si in SrAlSiH and SrAlSi is similar and the presence of H in SrAlSiH has little effect on the bonding of Al and Si. Instead H behaves as an anion whose removal thus electron dopes the band structure. Next we consider the band structure of hypothetical KAlSi, which is show in Fig. 3.3. This band structure was obtained at the same lattice parameters as SrAlSiH with the K placed in the Sr site, followed by relaxation of the internal coordinates. This relaxation yields very small shifts

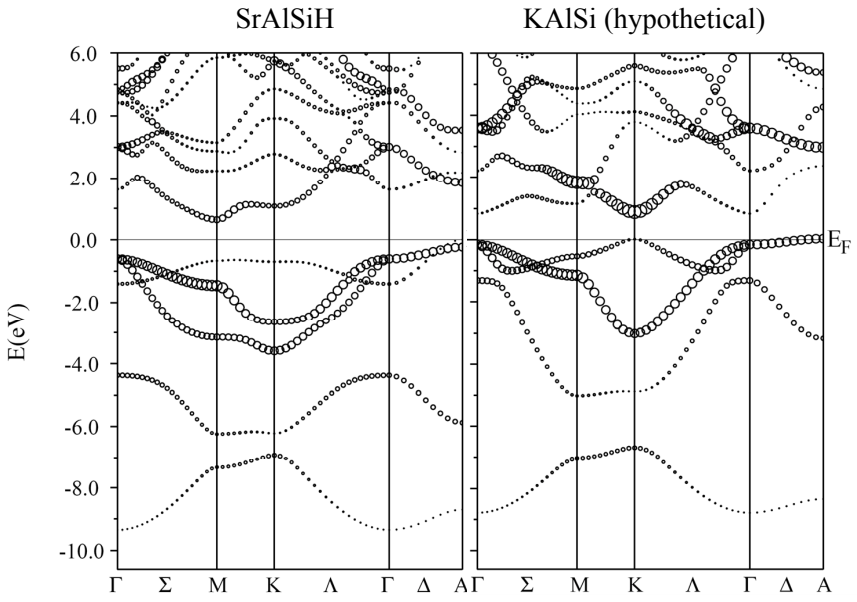

Figure 3.3: Electronic band structures of SrAlSiH (left) and hypothetical KAlSi (right), plotted with circles of size proportional to the Al p character, as defined by projection onto the Al LAPW sphere. The band structures are plotted along the path (0,0,0) $\rightarrow$ ($\frac{1}{2}$,0,0) $\rightarrow$ ($\frac{2}{3}$,$\frac{1}{3}$,0) $\rightarrow$ (0,0,0) $\rightarrow$ (0,0,$\frac{1}{2}$).

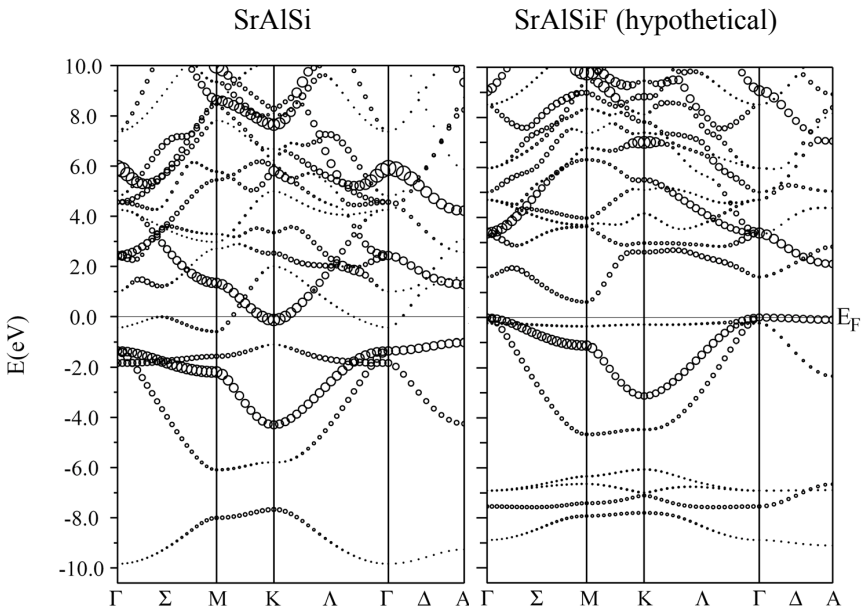

Figure 3.4: Electronic band structures of SrAlSi (left) and hypothetical SrAlSiF (right) plotted with symbols of size proportional to the Al p orbital character (plus a very small size to show the position of bands with no Al p character). The band structures are plotted along the path (0,0,0) $\rightarrow$ ($\frac{1}{2}$,0,0) $\rightarrow$ ($\frac{2}{3}$,$\frac{1}{3}$,0) $\rightarrow$ (0,0,0) $\rightarrow$ (0,0,$\frac{1}{2}$).

of the atomic positions relative to those of SrAlSiH. Again the band structure is similar to SrAlSiH except for the missing H s band. The main difference is a lowering in energy and increase in dispersion of the Si p_z derived bands. The greater sensitivity of the Si p_z orbital to the details of the Sr-H plane is as would be expected considering that this orbital is directed towards that plane. Like SrAlSi, KAlSi has only four bands below the Fermi energy between 0 and -10.0 eV. These mixed s and p bands of Al and Si will be discussed later when we describe the bonding between Al and Si. The fact that, excepting the H s band, the band structure of SrAlSiH can be reasonably reproduced with the Sr-H layer replaced by monovalent K is a strong indication that the H is at best weakly covalent with Al and that its main role is in accepting charge.

Finally, we consider the band structure of hypothetical SrAlSiF, which is shown in Fig. 3.4. As mentioned, in many cases there are close analogies between compounds based on H^- and fluorides. This calculation was done similarly to that of hypothetical KAlSi, with fixed lattice parameters and relaxed internal coordinates. Again we find a band structure rather similar to that of SrAlSiH, with the exception that the H s band is removed and three additional bands derived from the three occupied p orbitals of F^- occur in the valence bands. These three F p bands occur between -6 and -8 eV. Like SrAlSiH, hypothetical SrAlSiF is a semiconductor, which is perhaps not surprising if one considers that the fluoride anion is replacing a hydride anion of the same charge. The main difference in the occupied Sr-Al derived bands is a small upward shift and decrease in the dispersion of the Si p_z derived band, which as noted above is expected to be particularly sensitive to the details of the Sr-H layer. Since the three bands showing F p character all lie below the Fermi energy, F obtains one electron from Sr to get its p orbital filled. This is not surprising considering the high electronegativity of F. The Pauling electronegativity of H is also higher than Al and Si. This suggests that normally charge transfer onto Al-H units would preferentially go to H rather than Al. The similarities between SrAlSiH, KAlSi and SrAlSiF therefore support the view that H obtains one electron to fill its s orbital and is anionic.

We now return to the bonding between Al and Si in SrAlSiH. As mentioned above, the s character of both Al and Si is prominent in the lowest band that is centered at -8.0 eV. The Si p character is pronounced in the three bands below the Fermi energy that lie between 0.0 and -4.0 eV. However, Al p character is conspicuous in only two of these bands that dip below -2.0 eV. Let us remind ourselves that the Al-Si layer has a hexagonal structure. We have also shown that only s, p_x and p_y orbitals of Al and Si take part in the bonding. This implies that there is σ bond between hybridized sp^2 orbitals of Al and Si. It is also notable that

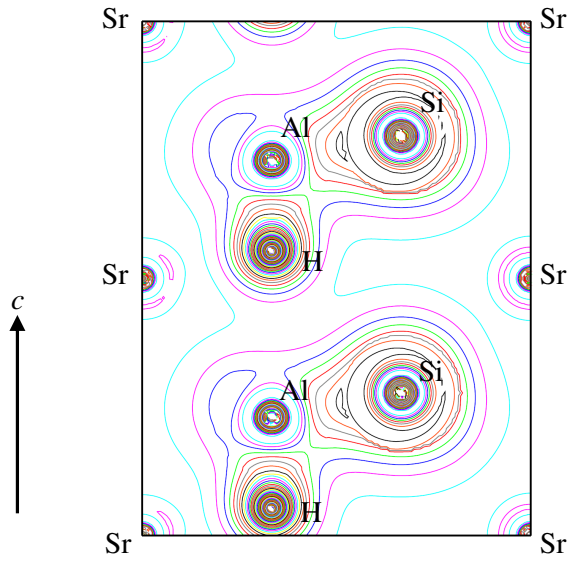

Figure 3.5: (color online) Valence charge density (not including semi-core states) for SrAlSiH in a plane passing through the atoms. The contours are in equally spaced increments of 0.05 $e/\text{Å}^3$ and start at 0.05 $e/\text{Å}^3$. Note the bond charge between Si and Al, but not between Al and H, and also the buildup of valence charge around H and Si.

there is more Si character than Al in each of these three bands, implying a polar σ bond. This is not surprising since Si is more electronegative than Al. The extra electron from Sr is transferred primarily to the Si so that there are two electrons in its p_z orbital. However, there is little covalent bonding between the Sr-H and Al-Si layers as there is no mixing of H s with s and p orbitals of Al and Si. Hence, SrAlSiH is perhaps better described as having mixed bonding character as in other Zintl type phases rather than as a polyanionic compound.

The band structure of SrAlSi (Fig. 3.4) also has four bands between 0.0 and -10.0 eV that are similar to the bands of SrAlSiH (Fig. 3.3). These bands have Al and Si s and p characters. The lowest band lies between -7.0 and -10.0 eV and has mixed Al s and Si s character. The three bands just below the Fermi energy have Si p character, which is mixed with Al p character for two of them. This again suggests that there is σ bonding between hybridized sp^2 orbitals of Al and Si, and

Si obtains one electron from Sr so that there are two electrons in its p_z orbital, which then is the origin of the third band.

The band structure of SrAlSiF (Fig. 3.4) has seven bands between 0.0 and −10.0 eV. However, except for the three bands between −6.0 and −8.0 eV that show F p character, this band structure is remarkably similar to those of KAlSi and SrAlSi. The lowest band still shows Al and Si s character. Two of the first three bands below the Fermi energy again has mixed Al and Si p character. The third band shows very dominant Si p character from the p_z orbital. Thus the Al and Si layer in SrAlSiF is bonded by σ bonds between hybridized sp^2 orbitals. The substitution of H by F in SrAlSiH does not seem to change the bonding behavior of Al and Si in these compounds. Therefore, we can now conclude that H does not play a substantial role in the bonding of Al and Si other than providing for charge balance.

Fig. 3.5 shows the valence charge density for SrAlSiH. As may be seen there is a noticable bond charge between Al and Si with a maximum in the valence charge density between the atoms. This feature is absent between Al and H but rather there is a build-up of charge centered at the H site. One may note that the Al-H bond lengths in SrAlSiH and $SrAl_2H_2$ (see below) are similar to those in $NaAlH_4$ and Li_3AlH_6. The electronic structure of $NaAlH_4$ was studied in detail by Ozolins and co-workers[45] who described the compound as polar covalent and also as having a highly ionic nature and by Aguayo and co-workers who made arguments that the compound is largely ionic.[46] A more detailed analysis was applied to Li_3AlH_6 also finding substantial ionic character in that case.[47] Those results are consistent with what is found here for the Al-H interaction. Thus the Zintl hydride SrAlSiH differs from complex hydrides, such as $NaAlH_4$ mainly in having a covalently bonded Si-Al backbone, which may offer different possibilities for chemical tuning of the properties.

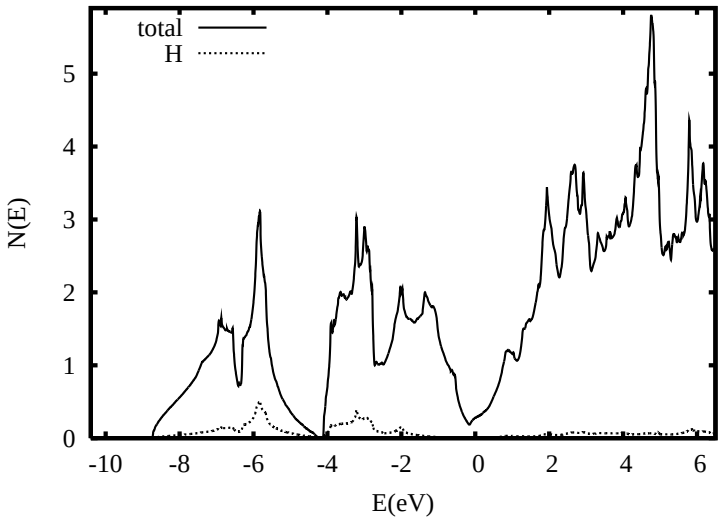

Figure 3.6: Electronic density of states of $SrAl_2H_2$, and projection onto the H LAPW sphere.

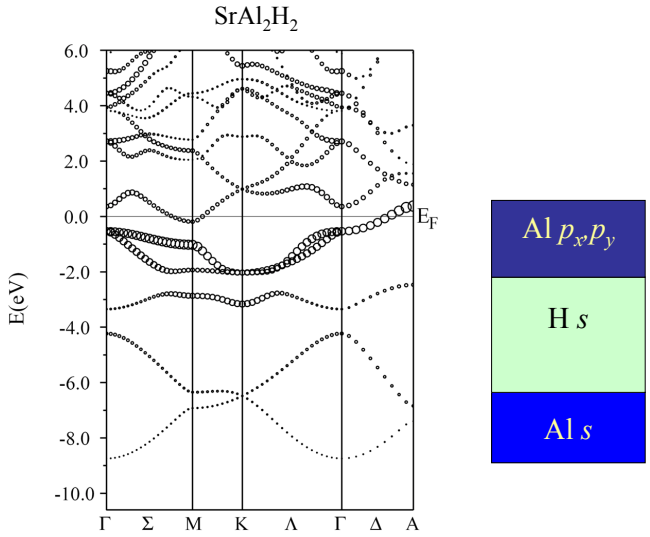

Figure 3.7: (color online) Electronic band structure of $SrAl_2H_2$ (left) plotted with symbols of size proportional to the Al p orbital character (plus a very small size to show the position of bands with no Al p character). The band structure is plotted along the path (0,0,0) $\rightarrow$ ($\frac{1}{2}$,0,0) $\rightarrow$ ($\frac{2}{3}$,$\frac{1}{3}$,0) $\rightarrow$ (0,0,0) $\rightarrow$ (0,0,$\frac{1}{2}$). The right panel is a schematic showing the regions in the valence bands where various orbital characters are dominant.

3.5 $SrAl_2H_2$

We now discuss the bonding of $SrAl_2H_2$. Our density of states and band structure are similar to that obtained previously by Orgaz and Aburto.[48] As mentioned earlier, this material is very similar to SrAlSiH. The Si is replaced by Al and H, so we now have Al-Al and Sr-H_2 layers instead of Al-Si and Sr-H ones. The electronic density of states of $SrAl_2H_2$ is shown in Fig. 3.6. Almost all of the H character occurs below Fermi energy indicating that H atoms are anionic. Again, we consider the ionic model where H^- ion is stabilized by the Ewald field. As mentioned above, the charge inside the radius of 1.0 a_0 is $0.482e$. The integrated DOS of H below the Fermi energy is 0.897. Dividing this number by $0.482e/2$ and recalling that there are two H per cell one obtains $1.86e$/H, i.e. very close to H^-.

We can gain more insight about the bonding in $SrAl_2H_2$ by studying its band structure, which is shown in Fig. 3.7. Near the Fermi energy, there are two bands of Al p character that stay mostly below the Fermi level, but cross along Γ-A, leading to semimetallic character. In particular these two bands lead to hole Fermi surfaces around A, which are compensated by an electron pocket around M.

The next lower two bands that lie between -2.0 and -7.0 eV have H s character, confirming that s orbitals of two H atoms are filled. Finally, Al s character is prominent in the fifth band below Fermi level which reaches a high of approximately -6.5 eV at the K point and a low of approximately -9.0 eV at Γ. As in SrAlSiH, there is little H s character in the conduction bands. As mentioned earlier, the Al-Al layer has a hexagonal structure. This suggests that the s, p_x and p_y orbitals of Al hybridize into sp^2 orbitals and each Al atom is σ bonded with three other Al atoms. Within this scenario the main difference between semiconducting SrAlSiH and metallic $SrAl_2H_2$ is that in the silicide the p_z orbital of Si is occupied, and the sp^2 σ bonds are take some polar character, this latter

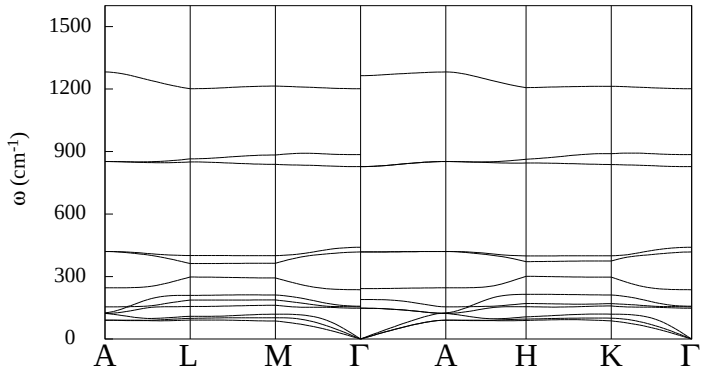

Figure 3.8: Calculated phonon dispersion for SrAlSiH along the path $(0,0,\frac{1}{2}) \rightarrow (\frac{1}{2},0,\frac{1}{2}) \rightarrow (\frac{1}{2},0,0) \rightarrow (0,0,0) \rightarrow (0,0,\frac{1}{2}) \rightarrow (\frac{2}{3},\frac{1}{3},\frac{1}{2}) \rightarrow (\frac{2}{3},\frac{1}{3},0) \rightarrow (0,0,0)$.

feature leading to the semiconducting gap. In both compounds the role of Sr and H is to provide charge balance. In particular, we note that in $SrAl_2H_2$ the Al layers are nominally neutral (i.e. not polyanionic).

3.6 Phonon Dispersions and Gallium Compounds

Phonon dispersions are often useful in understanding bonding. Generally speaking, a covalent H bond is stronger than an anionic H bond, and has both a shorter bond length and higher force constants. For comparison, experimental vibrational frequencies of symmetric stretching modes of the covalently bonded NH_3 and H_2O molecules are 3336 and 3657 cm^{-1}, respectively (Ref. [49]). On the other hand, the largest vibrational frequencies of fcc LiH and tetragonal MgH_2 obtained from the calculated phonon dispersion curves are around 1100 and 1500 cm^{-1}, respectively.[50, 51] The phonon dispersion curves of SrAlSiH and $SrAl_2H_2$ are shown in Figs. 3.8 and 3.9, respectively. From these plots, the largest phonon frequencies for SrAlSiH and $SrAl_2H_2$ are approximately 1280 and 1430 cm^{-1}, respectively. For comparison, the bond stretching frequency of the GaH dimer is

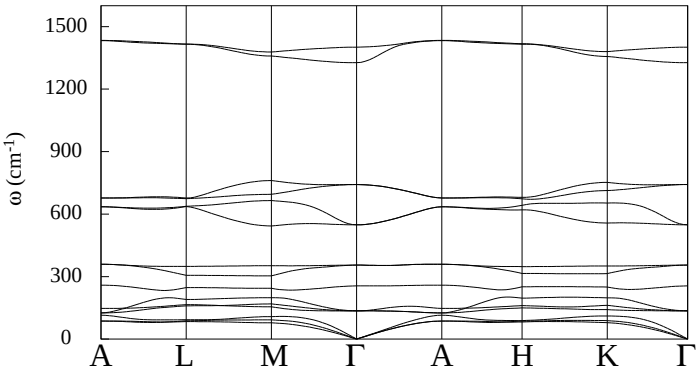

Figure 3.9: Calculated phonon dispersion curves for $SrAl_2H_2$ along the path $(0,0,\frac{1}{2}) \rightarrow (\frac{1}{2},0,\frac{1}{2}) \rightarrow (\frac{1}{2},0,0) \rightarrow (0,0,0) \rightarrow (0,0,\frac{1}{2}) \rightarrow (\frac{2}{3},\frac{1}{3},\frac{1}{2}) \rightarrow (\frac{2}{3},\frac{1}{3},0) \rightarrow (0,0,0)$.

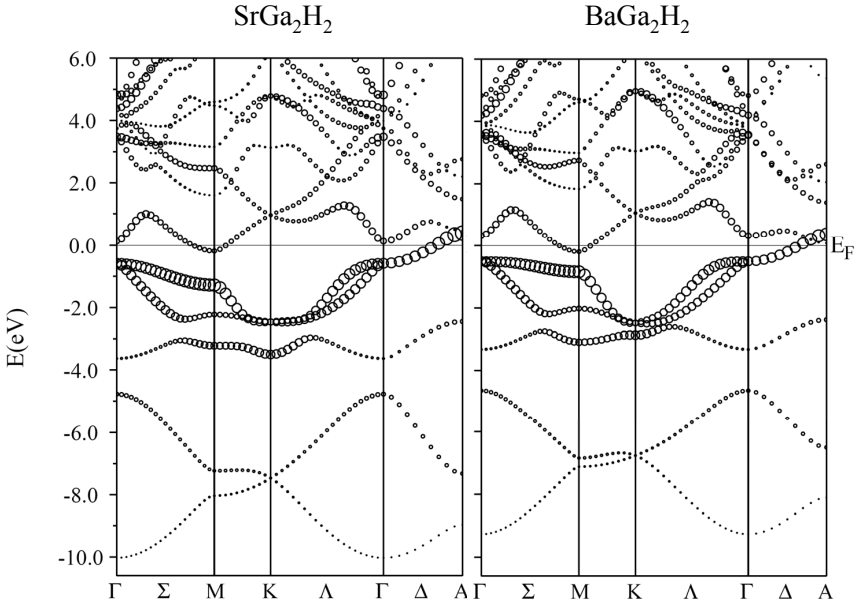

Figure 3.10: Electronic band structures of $SrGa_2H_2$ (left) and $BaGa_2H_2$ (right) plotted with symbols of size proportional to the Ga p orbital character (plus a very small size to show the position of bands with no Ga p character). The band structures are plotted along the path $(0,0,0) \rightarrow (\frac{1}{2},0,0) \rightarrow (\frac{2}{3},\frac{1}{3},0) \rightarrow (0,0,0) \rightarrow (0,0,\frac{1}{2})$.

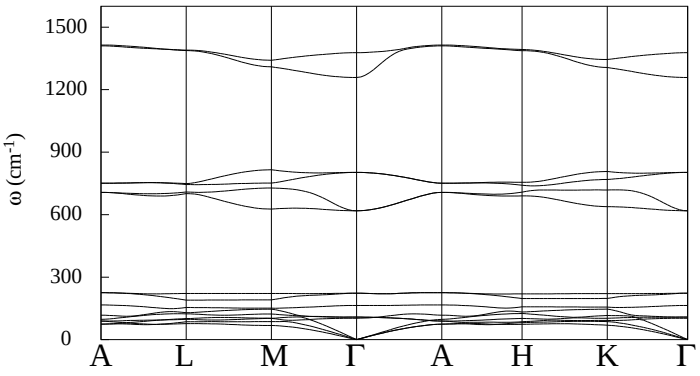

Figure 3.11: Calculated phonon dispersion curves for $SrGa_2H_2$ along the path $(0,0,\frac{1}{2}) \rightarrow (\frac{1}{2},0,\frac{1}{2}) \rightarrow (\frac{1}{2},0,0) \rightarrow (0,0,0) \rightarrow (0,0,\frac{1}{2}) \rightarrow (\frac{2}{3},\frac{1}{3},\frac{1}{2}) \rightarrow (\frac{2}{3},\frac{1}{3},0) \rightarrow (0,0,0)$.

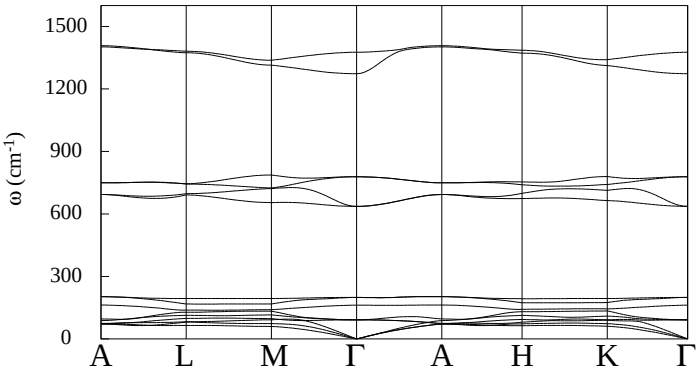

Figure 3.12: Calculated phonon dispersion curves for $BaGa_2H_2$ along the path $(0,0,\frac{1}{2}) \rightarrow (\frac{1}{2},0,\frac{1}{2}) \rightarrow (\frac{1}{2},0,0) \rightarrow (0,0,0) \rightarrow (0,0,\frac{1}{2}) \rightarrow (\frac{2}{3},\frac{1}{3},\frac{1}{2}) \rightarrow (\frac{2}{3},\frac{1}{3},0) \rightarrow (0,0,0)$.

1605 cm^{-1} and that of AlH is 1670 cm^{-1}. We note that these maximum frequencies are close to the maximum frequencies reported in the calculations of Ref. [37], but that our dispersions have some minor but possibly significant quantitative differences, especially non-analytic character at Γ for SrAlSiH, as would be anticipated for an ionic insulator. The differences between our calculation and that of Lee and co-workers are, however, too small to distinguish based on existing neutron scattering data.[37]

Our results for the electronic structure and phonon dispersions of the gallium compounds, $SrGa_2H_2$ and $BaGa_2H_2$ are given in Figs. 3.10, 3.11 and 3.12. As may be seen, the electronic structures have strong similarities to those of the $SrAl_2H_2$ in the valence region and that the phonon dispersions are also similar to those of the Al based compound with the exception that the metal derived phonon frequencies of the gallium compounds are lower due to the heavier mass of Ga relative to Al. As for the Al compounds, the H derived phonon bands consist of two narrow bands - a longitudinal band at the highest frequencies and a transeverse band with twice as many modes at lower frequency. Both of these bands are well above the highest metal atom derived phonon band in these materials. This separation into narrow well separated phonon bands is characteristic of materials with large mass differences between the atoms and relatively weak bonding. In any case, the bonding of the gallium compounds can therefore be analyzed in a similar way to that of $SrAl_2H_2$ with the conclusion that the Ga layers are sp^2 σ bonded and that H occurs as the H^- anion.

3.7 Discussion and Conclusions

We have presented a series of electronic structure calculations for the Zintl phase hydrides and model compounds. Comparison of the electronic structures leads

to the conclusion that in these phases the Al/Si/Ga layers are stabilized by sp^2 covalent bonding, and that the Sr and H atoms occur as ions that provide charge balance. Within this framework the semiconducting nature of SrAlSiH is due to polarization of the Al-Si bond. We note that the concept of electronegativity is an important one in chemistry, and especially solid state chemistry where the long range Ewald potential favors larger charge transfers than in molecules. The present conclusion that these phases are based on the hydride anion is consistent with the high electronegativity of H relative to Al and Ga.

Characterizing the nature of bonds in solids in terms of charge transfer involves ambiguity since there is no unique way of partitioning space into regions that can be associated with the atoms and because expansions around atomic sites become overcomplete as basis functions are added. However, such characterizations are often very useful in understanding the properties of compounds, the relationships between different compounds, and in finding new related phases. We hope that the present characterization of the bonding in the Zintl phase hydrides will be useful in identifying new members of this family and better understanding their chemical and physical properties.

We find that SrAlSiH is stabilized by ionic bonds and occurs in a non-centrosymmetric polar structure. This structure is generated from an ideal non-polar structure with $z_{\mathrm{H}} = 0.0$ and $z_{\mathrm{Al}} = z_{\mathrm{Si}} = 0.5$ by displacements of H and Al in opposite directions by $\sim$ 0.5 Å, in the case of H and $\sim$ 0.2 Å, for Al, accompanied by a displacement of Si by $\sim$ 0.25 Å, in the same direction as H. Considering that in our picture of the bonding, Si and H take the charge provided by Sr, this is a structure in which the anions (H and Si) move opposite to the Al and Sr. The fact that the displacements are in the several tenths of Angstrom range suggests that the structure may be switchable, as in e.g. $BiFeO_3$ and $LiNbO_3$. This is an interesting result because while ferroelectrics containing hydrogen are known,

they are phases containing complex anions such as hydrogen phosphate. To our knowledge, if SrAlSiH is ferroelectric, it would be the first inorganic ferroelectric based on the hydride anion. It would be of interest to perform high electric field low temperature measurements on SrAlSiH to determine if it can be poled and dielectric measurements to determine if ferroelectric switching and hysteresis loops can be obtained.

In this regard, we calculated the energy of the fully symmetric structure in which Al, Si and H were all placed on the reflection planes. This is intermediate between the up and down polarized SrAlSiH structures, and therefore provides an upper bound on the energy barrier for switching. The calculated energy is 0.27 eV above the relaxed structure consistent with ferroelectric switching.[†] The calculated electronic dielectric constant as obtained from linear response is high reflecting the relatively small gap: ϵ_{xx}=ϵ_{yy}=13.4 and ϵ_{zz}=11.3. The Born effective charges also obtained from the linear response calculations without enforcing the acoustic sum rule are Z^*_{xx}(Sr)=2.1, Z^*_{zz}(Sr)=2.3, Z^*_{xx}(Al)=2.2, Z^*_{zz}(Al)=1.3, Z^*_{xx}(Si)=−2.7, Z^*_{zz}(Si)=−2.7, Z^*_{xx}(H)=−1.4, and Z^*_{zz}(H)=−1.7. One may note that the Born charges are enhanced over the nominal values and are anisotropic. Enhancement of Born charges is characteristic of ionic materials with cross-gap hybridization, such as oxide ferroelectrics.[52] In contrast, covalent materials such as GaAs generally have Born effective charges that are reduced from the nominal values.

As mentioned, the Ewald potential, which is important in the stabilization of ionic structures, is long ranged. Therefore, the bonding of such materials is typically quite sensitive to chemical substitutions. While for example, partial substitution in the Sr site might not be expected to be very important in the stabilization of a supposed Al-H covalent bond, they could well have a large effect

[†]Note that 180° switching in ferroelectrics is normally by domain wall motion, which would be the expected switching mechanism here.

on the stability of hydride anions in the structure based on the bonding that we find. In addition, ionic bonding can be strongly affected by dielectric screening. So for example, it may be that chemical modification that improves the metallicity of the semimetallic Al layers in $SrAl_2H_2$ or that metalizes the Al-Si layer in SrAlSiH would destabilize the hydride anions in those compounds. Also, it may be that small scale nanostructuring to produce interfaces with metallic compounds including carbons, would also destablize the hydride anions – a result that would not be expected in a covalently bonded system.

Chapter 4

Ab Initio phonon dispersions for PbTe

A similar version of this chapter appeared as *"Ab initio phonon dispersions for PbTe"*, Jiming An, Alaska Subedi, and David J. Singh, Solid State Commun. **148**, 417 (2008).

4.1 Introduction

The thermoelectric performance of a material is quantified using a dimensionless, temperature dependent figure of merit, $ZT = \sigma S^2 T/\kappa$, where σ is the electrical conductivity, κ is the thermal conductivity, and S is the thermopower. Thus it is clear that high thermoelectric performance is generally found in materials with low thermal conductivity, and in fact various strategies for lowering thermal conductivity based on phonon scattering have been employed.[53, 54, 55, 7] These include alloying to produce mass disorder as in SiGe, the use of materials with large complex unit cells, and the use of materials with rattling ions, such as filled clathrate materials.[7] In this regard rocksalt structure PbTe is a remarkable

thermoelectric material. It is based on a small, high symmetry unit cell, has high coordination of both atomic species (6-fold), and contains no obvious rattling ion. Nonetheless, n-type PbTe has high values of ZT above room temperature and as such was used in spacecraft power generators.[56, 57] It also has low thermal conductivity, reported as 2.3 W/(m K) at ambient temperature.[6] More recently, a family of so-called LAST compounds based on intergrowths of PbTe and Ag_xSbTe_2 have been shown to have values of ZT well above unity,[58] and additionally quantum dot systems based on PbTe have also shown high values of ZT.[59]

Thermal properties of materials in general rest on the phonon dispersions. While electronic and related properties of PbTe has been rather extensively studied using first principles methods,[60, 61, 62, 63, 64] the phonon dispersions have not been reported. In this chapter, we report these dispersion as obtained within density functional theory and discuss its relevance to the thermal properties of PbTe.

4.2 Approach

The calculations reported here were done within the framework of density functional theory primarily using the local density approximation. The quantum espresso code was used with norm conserving pseudopotentials to obtain the phonon dispersions via linear response.[31] Convergence tests were performed to determine the needed planewave basis cut-off and zone sampling. The results shown used a planewave basis set with a 60 Ry cutoff and an $(6, 6, 6)$ special $\mathbf{k}$-points Brillouin zone sampling. We performed convergence tests with a 75 Ry cutoff and an $(8, 8, 8)$ special $\mathbf{k}$-points Brillouin zone sampling but found no significant differences in phonon frequencies. In addition, some calculations were done with the linearized augmented planewave (LAPW) method including local orbitals.[19]

These provide a check for the pseudopotential results. Calculations were performed as a function of lattice parameter. The calculated LAPW LDA lattice parameter is 6.39 Å, which is slightly more than 1% smaller than the experimental room temperature lattice parameter of 6.464 Å,[65] and within 1% of the 120K value of 6.438Å.[66] For comparison the calculated LAPW lattice parameter within the generalized gradient approximation of Perdew, Burke and Ernzerhof[29] is 6.57 Å, which as is sometimes that case for materials with heavy elements[67] is further from experiment than the LDA. We therefore use the LDA, and perform calculations as a function of lattice parameter. Assuming that PbTe behaves like other materials with soft phonons, comparison with experiment should be done for the phonon dispersions calculated at the experimental lattice parameter.[68]

4.3 Results and Discussion

Our main results are the phonon dispersions, which are given in Fig. 4.1. As may be seen, PbTe is near a zone center phonon instability, associated with the transverse optic (TO) mode. This is an inversion center breaking phonon, and would lead to a ferroelectric ground state if it were actually unstable. This is not a surprising result and in particular is in accord with experimental studies of NaCl structure group IV tellurides. The related materials SnTe and GeTe are in fact ferroelectric, with rhombohedral ground states corresponding to freezing in of the soft TO mode with displacements along a [111] direction.[69, 70, 71]

The ferroelectricity of GeTe has been studied in detail using first principles calculations by Rabe and co-workers,[72, 73, 74] who showed quantitative agreement between the predictions of LDA calculations and experiment. Bussmann-Holder used model calculations to investigate the phase diagrams of various alloys including PbTe-SnTe and PbTe-GeTe and made arguements for the nearness of

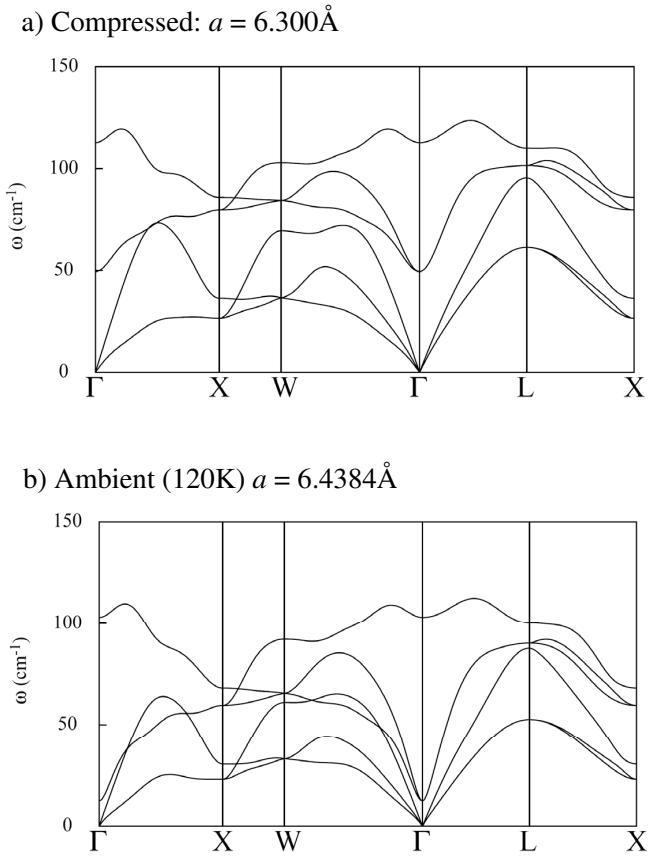

Figure 4.1: Calculated phonon dispersions of PbTe at a lattice parameter of a=6.30Å (top) and at the experimental 120K lattice parameter, a=6.4384Å (bottom). The dispersions are plotted along the path (0,0,0) $\rightarrow$ ($\frac{1}{2}$,0,0) $\rightarrow$ ($\frac{1}{2}$,$\frac{1}{4}$,0) $\rightarrow$ (0,0,0) $\rightarrow$ ($\frac{1}{4}$,$\frac{1}{4}$,$\frac{1}{4}$) $\rightarrow$ ($\frac{1}{2}$,0,0).

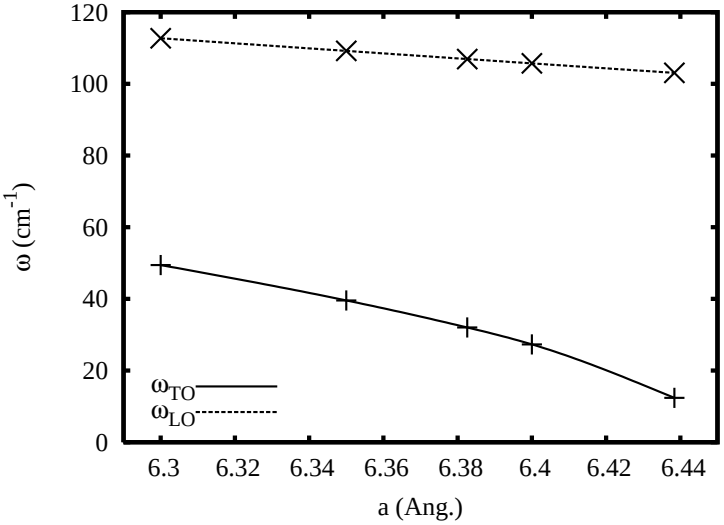

Figure 4.2: Zone center transverse and longitudinal optical phonon frequency of PbTe as a function of lattice parameter.

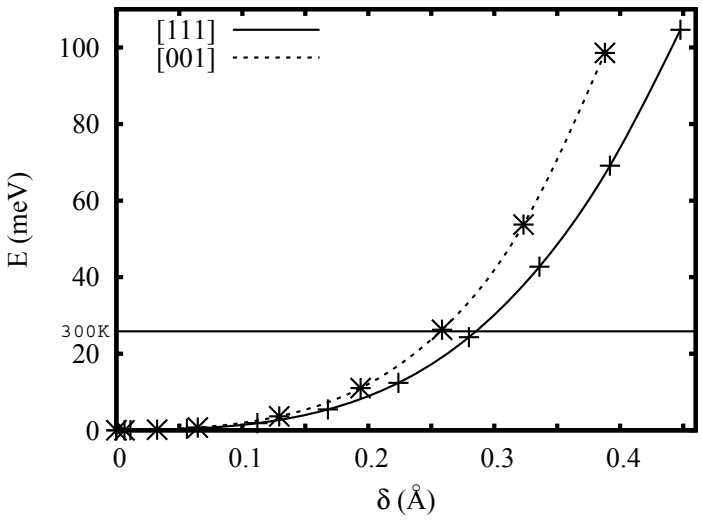

Figure 4.3: Calculated energy as a function of phonon amplitude for the Γ point TO mode, with displacements along the tetragonal and rhombohedral directions for the experimental 300K lattice parameter of 6.464Å. The horizontal line corresponds to kT for T=300K.

PbTe to ferroelectricity.[75] In fact it was known that PbTe shows a dielectric constant that increases at low T as well as a TO phonon mode that decreases in frequency as the temperature is lowered,[70, 76] although the detailed T dependence is complicated by a doping level dependence. In any case, Burhard and co-workers[76] obtained obtained a very soft frequency of 17.5 cm^{-1} from optical measurements on PbTe films. This value is consistent with the very low value of 12 cm^{-1} that we obtain at the reported experimental lattice parameter. This difference of ~ 5 cm^{-1} is well within the usual errors of LDA calculations.

Comparing the two panels of Fig. 4.1, one may note a strong volume dependence of the TO phonon frequency around the zone center. This frequency at Γ is plotted as a function of lattice parameter in Fig. 4.2. As may be seen there is a very strong volume dependence to the soft TO mode. Compressing the lattice parameter to 6.40 Å, which is less than 0.6% smaller than the 120K value, more than doubles the TO frequency from 12 cm^{-1} to 27 cm^{-1}. The LO mode on the other hand shows a quite ordinary, modest volume dependence. While such strong volume dependences of soft mode phonon frequencies are unusual they have been noted before in complex oxide ferroelectrics, such as $Pb(Zr,Ti)O_3$, $BaTiO_3$ and $KNbO_3$.[77, 68, 78] The present results show that there is a similar behavior in PbTe in spite of the much simpler structure of this material in comparison with the oxide ferroelectrics.

Returning to the issue of the thermoelectric properties of PbTe, the material clearly does not involve alloying with different mass ions or a large complex unit cell to lower thermal conductivity. Furthermore, the acoustic modes are not anomalously soft. One mechanism that has been discussed in the context of thermoelectric materials is the use of so-called rattlers. These are loosely bound atoms in a crystal structure that couple to the low frequency part of the phonon spectrum leading to scattering. One may ask then if there is an analogy

between the soft TO vibrations near the zone center and a material containing rattlers. One such connection can be made based on the strong volume dependence. Longitudinal acoustic (LA) vibrations are compressive waves and so the strong volume dependence of the TO mode implies strong anharmonic coupling between the TO branch and the LA phonons. Furthermore, we find that the TO modes are highly anharmonic themselves. Fig. 4.3 shows the calculated energy as a function of TO mode amplitude at the experimental volume. As may be seen the energy surface remains very soft up to large amplitude ~ 0.1 Å, and then starts to stiffen in a quite anharmonic way. This may be seen, *e.g.* from the difference between [001] and [111] energies, which arises due to the anharmonicity. For large amplitudes the softest direction is [111] in agreement with the experimental ground state of GeTe. However, even for [001] displacements the energy surface is very soft implying large amplitude vibrations even at room temperature. However, it should be noted that the TO mode is only soft near the zone center, and so the mean square displacement will be less than that implied by the position of the kT=300 K line on Fig. 4.3. This also means that unlike rattling modes in clathrates, for example, the soft TO modes in PbTe are strongly **k**-dependent, similar to the acoustic modes.

4.4 Conclusion

While the above results do not provide a quantitative description of the thermal conductivity of PbTe they do show that there are unusual features of the phonon spectrum that are generally associated with reduced thermal conductivity. In particular we find very soft TO phonon branches near the zone center as may be expected in a material near ferroelectricity. Importantly, these modes are very

volume dependent which implies strong anharmonic coupling to longitudinal acoustic modes. Furthermore, although the TO modes are quite **k**-dependent, which is not an indicator of low thermal conductivity, they are also highly anharmonic, as seen from the Fig. 4.3. This normally will lead to increased scattering at high temperature and accordingly reduced thermal conductivity.

Another recent and interesting development in PbTe has been the discovery of superconductivity when it is hole doped by Tl.[79, 80] $Pb_{1-x}Tl_xTe$ is superconducting with a maximum T_c of $\sim$ 1.5 K for Tl concentration up to $x = 1.4\%$. Strong dependence of TO modes on volume and proximity to ferroelectricity suggest electron-phonon coupling in this material may be significant. Moreover, according to Eq. 2.12, the electron-phonon coupling is more enhanced for low frequency phonon modes. If the soft TO modes have high electron-phonon coupling, our results point to the possibility that superconductivity in hole doped PbTe may be explained within the conventional electron-phonon scenario.

Chapter 5

Ferroelectricity in the double perovskites BiMZnNbO$_6$ (M = Pb and Sr)

A similar version of this chapter appeared as *"Polar behavior of the double perovskites $BiMZnNbO_6$ (M = Pb and Sr) from density-functional calculations"*, Shigeyuki Takagi, Alaska Subedi, David J. Singh and Valentino R. Cooper, Phys. Rev. B **81**, 134106 (2010).

5.1 Introduction

Perovskite ferroelectrics and relaxor ferroelectrics are widely used in applications including electromechanical transducers, actuators, passive electronic components, memory devices and microwave technology. There is strong interest in obtaining improvements in materials performance, such as high polarization, high Curie temperature, improved electromechanical coupling and lower loss. One approach is through the exploration of new materials. Besides this technological motivation,

these materials have been the focus of considerable fundamental interest, particularly in unraveling the complex interplay between crystal chemistry and lattice distortions and in understanding the range of polar behaviors that can be produced by strain and chemical substitutions. Much has been learned over the past several years.

The lattice instabilities of perovskite oxides, ABO_3 are often understood using the tolerance factor $t = (r_O + r_A)/\sqrt{2}(r_O + r_B)$, where r_O, r_A and r_B are the ionic radii for the O, A-site and B-site ions, respectively.[81, 82, 83] These materials are classed in two groups according to whether the tolerance factor is less than unity or not. Several $t > 1$ ferroelectrics are known, including the prototypical materials, $BaTiO_3$ and $KNbO_3$. In these materials there is a tendency towards lattice distortions where the too-small B-site ion off-centers. This is strongly enhanced by covalency involving O $2p$ states and nominally unoccupied B-site d states. This then leads to enhanced Born effective charges and large longitudinal optic - transverse optic splittings.[84, 52] In the majority of $t < 1$ materials the BO_6 octahedra are tilted and they are not ferroelectrics.[85] The exceptions are generally perovskites with lone-pair A-sites such as Pb and Bi. In these cases, the ideal cubic perovskite structure is often unstable against octahedral tilting, but the ferroelectric instability, which is enhanced by the stereochemical activity of the A-site, is stronger. In materials with $t < 1$ but no stereochemically active A-site ion, there is often a substantial ferroelectric instability of the ideal cubic structure, but now the tilt instability is stronger, and so ferroelectricity does not occur.[86, 87, 88] However, according to first principles calculations, if the octahedra are prevented from tilting by mixing large and small A-site ions they may become ferroelectrics.[8] There is experimental support for this. For example, ferroelectricity in the $(Ba,Ca)TiO_3$ solid solution is strongly enhanced compared to what would be expected interpolating between the properties of the

end-point compounds.[9] Importantly, this leads to new compositions that have high piezoelectric coefficients.[9, 89]

Generally, high piezoelectric coefficients and electromechanical coupling are found near phase boundaries. In particular, the electromechanical coupling in perovskite piezoelectrics is associated with polarization rotation near morphotropic phase boundaries (MPBs).[90, 91] These are generally boundaries between ferroelectric states differing in the direction of their ground state polarization. Therefore one strategy for finding new piezoelectric compositions is to search for solid solutions with MPBs. A particular emphasis has been in solid solutions with $PbTiO_3$ (PT) as one end-point, following the commonly used $Pb(Zr,Ti)O_3$ (PZT) system and the $PbMg_{1/3}Nb_{2/3}O_3$ (PMN) - PT and $PbZn_{1/3}Nb_{2/3}O_3$ (PZN) - PT piezocrystal systems.[92] PT is tetragonal with a substantial tetragonality. There is considerable interest in finding materials that can be alloyed with PT and which have strong ferroelectricity with rhombohedral or related ground states to produce an MPB perhaps with high Curie temperature, high polarization and high tetragonality on the tetragonal side of the MPB.

A development of potential importance is the realization that Bi based perovskites can be very useful ferroelectrics, as exemplified by progress in $BiFeO_3$. In particular, the small ionic radius and stereochemical activity of Bi^{3+}, leads to large displacements in a low volume unit cell, and its high charge (3+ vs. 2+ for Pb) and hybridization of Bi $6p$ states with O $2p$ states leads to a high Born charge.[93] Furthermore, experimental work on the $BiScO_3$ - PT solid solution shows an MPB with enhanced Curie temperature,[94] and there have been recent studies of several other Bi-based perovskites in solid solutions with PT.[95, 96, 97, 98, 99]. One problem has been that while the small Bi-ion tends to enhance tetragonality on the tetragonal side of the MPB, this same effect may prevent the occurrence of an MPB, leading to phase diagrams with only tetragonal phases.

Recently, an extremely large tetragonality ($c/a \sim 1.11$ and high Curie temperature T_C of ~ 700 °C at $x = 0.6$ was reported for perovskite solution $(1-x)\mathrm{Bi}(\mathrm{Zn}_{1/2}\mathrm{Ti}_{1/2})\mathrm{O}_3$-$(x)\mathrm{PbTiO}_3$.[100] This is reminiscent of the behavior of CdTiO_3 - PT alloys, which also have highly enhanced tetragonality.[86, 101, 102] In perovskites the balance between tetragonal and rhombohedral states is generally controlled by a balance between the energy lowering due to tetragonal strain, which favors the tetragonal state, and the *B*-site off-centering, which favors a rhombohedral state[103] (note that with small *A*-site ions there is an additional stabilization of the tetragonal state because off-centerings along [001] directions are towards the most open face of the O cage around the *A*-site; therefore, this direction is favored for the *A*-site and this can be important if the displacement is very large[87]). The interplay of *A*-site and *B*-site off-centering, and the importance of the *B*-site in determining the direction of the ferroelectric polarization suggests the exploration of alternate *B*-site ions in solid solutions with PT to obtain an MPBs.

Here, we present a study of the polar behavior of perovskite $(\mathrm{Bi,Pb})(\mathrm{Zn,Nb})\mathrm{O}_6$ and $(\mathrm{Bi,Sr})(\mathrm{Zn,Nb})\mathrm{O}_6$ using density functional supercell calculations. The purpose is to explore the effect of combining the mechanisms discussed above in a perovskite that may be amenable to experimental synthesis. Specifically, the compositions explored have different size *A*-site cations (Pb and Bi), stereochemically active ions on the *A*-site (particularly, Bi, though Pb may also contribute as discussed below), and ions with electronic structures that favor cross-gap hybridization and therefore ferroelectricity on the *B*-site (Nb and Zn).

As mentioned, one motivation for this study is to explore the use of different size *A*-site ions in relation to stereochemical activity to obtain *A*-site driven ferroelectricity. The ionic radii[82] of the *A*-site ions considered here are $r_{\mathrm{Pb}^{2+}} = 1.63$ Å, $r_{\mathrm{Sr}^{2+}} = 1.58$ Å, and $r_{\mathrm{Bi}^{3+}} = 1.31$ Å. Thus, Bi^{3+} is significantly smaller than

the other A-site ions and Pb and Sr have approximately the same size, but unlike Sr, Pb has stereochemical activity that can favor ferroelectricity, as in $PbTiO_3$.

Related to this there is an experimental report of the synthesis and some physical properties of perovskite $(Bi_{0.5}Sr_{0.5})(Mg_{0.5}Nb_{0.5})O_3$, $(Bi_{0.5}Ba_{0.5})(Mg_{0.5}Nb_{0.5})O_3$, $(Bi_{0.5}Sr_{0.5})(Zn_{0.5}Nb_{0.5})O_3$, $(Bi_{0.5}Ba_{0.5})(Zn_{0.5}Nb_{0.5})O_3$, and the solid solution of $(Bi_{0.5}Ba_{0.5})(Zn_{0.5}Nb_{0.5})O_3$ with PT and $(Bi_{0.5}Sr_{0.5})(Mg_{0.5}Nb_{0.5})O_3$ with $SrTiO_3$.[104, 105] The compound $(Bi_{0.5}Sr_{0.5})(Mg_{0.5}Nb_{0.5})O_3$ was reported to be ferroelectric based on the observation of a hysteresis loop below 103 K. All four compounds were reported to show phase transitions above room temperature and relatively high dielectric constants. They also show substantial microwave loss, which may indicate ferroelectricity.

5.2 Approach

The perovskite alloys were studied using supercell calculations within density functional theory. The main results are for compositions $BiPbNbZnO_6$ and $BiSrNbZnO_6$. The large charge difference between Zn^{2+} and Nb^{5+} may be expected to lead to a strong ordering tendency on the B-site. This is the case in the relaxor systems $PbZn_{1/3}Nb_{2/3}O_3$ (PZN) and $PbMg_{1/3}Nb_{2/3}O_3$ (PMN), where a double perovskite like structure occurs even though the Nb:Zn stoichiometry is not 1:1 (specifically, in PZN and PMN one double perovskite B-site sublattice is Nb and the other is 1/3 Nb and 2/3 Zn or Mg, which in turn may further order).[106, 107, 108] In the present case the stoichiometry is 1:1, which should further stabilize the ordering. Therefore we assume an ordering of the B-site lattice into a double perovskite structure. In contrast, there is no a priori reason to assume that the A-site lattice consisting of Pb and Bi is chemically ordered.

$BiPbZnNbO_6$ (BPZN) and $BiSrZnNbO_6$ (BSZN) have ferroelectrically active ions on both the A and B sites. On the B-site both Zn^{2+} and Nb^{5+} favor ferroelectricity, as is evident from the stronger relaxor ferroelectricity of PZN relative to PMN and the ferroelectricity of $KNbO_3$. Likewise Bi^{3+} and Pb^{2+} are stereochemically active, and favor ferroelectricity on the perovskite A-site. However, both BPZN and BSZN are expected to be strongly A-site driven materials both based on ionic radius ($t < 1$, and A-site size disorder) and lone pair physics,[103] and as such a competition between octahedral tilts and polar off-centering may be expected similar to the $Pb(Zr,Ti)O_3$ system.[78] Therefore it is important that the supercells are constructed in a way that this competition can be included. The minimum size for this is 2x2x2, or 40 atoms, since such a cell has an even number of units along the [001], [011], and [111] directions and therefore can accommodate the various Glazer tilt patterns.[109]

An additional constraint comes from the fact that with multiple A-site ions it is possible to choose cells that have polar spacegroups just because of the cation ordering and not because of lattice instability. This would not represent ferroelectricity, but would rather simply be an artifact of the selected order. Therefore even though Bi and Pb are not expected to chemically order in the solid solutions, we consider them in a highly ordered state within our supercells. Here we select a rock-salt ordering of Pb and Bi on the A-site. The cation ordering with this choice has symmetry $F\bar{4}3m$, which is non-polar. Thus any polarization or off-centering is a consequence of lattice instability and not the choice of cation ordering, and furthermore, one may expect that a more disordered alloy would have a better frustration of the tilts and a stronger ferroelectric tendency.[8]

The density functional (DFT) calculations were done using two methods. We used the general potential linearized augmented planewave (LAPW) method[19] for the structure relaxations. This is a full potential all electron method. We did the

calculations using the local density approximation at a scalar relativistic level. Well converged basis sets were employed with LAPW sphere radii of 2.3 Bohr for Pb, Sr and Bi, 1.90 Bohr for Zn and Nb and 1.55 Bohr for O. We included local orbitals to relax linearization and to accurately treat semicore states.[110] The polarization and Born effective charges were calculated with an ultrasoft pseudopotential method as implemented in the quantum espresso package,[31] using the relaxed structures from the LAPW calculations. The results were converged with respect to the Brillouin zone sampling, which was tested. The polarization was obtained using the Berry's phase method.[111, 112]

5.3 Results

We started by assuming a pseudocubic structure, i.e. setting the lattice parameters of our 40 atom supercells to be orthogonal and equal. We then fully relaxed the internal coordinates of all atoms in the cell, with no symmetry constraints. This was done as a function of the lattice parameter to obtain the equilibrium cell volumes for $BiPbZnNbO_6$ and $BiSrZnNbO_6$. This was done in the LDA using the LAPW method. The effective perovskite lattice parameters for the minimum energy were 3.99 Å, for $BiPbZnNbO_6$ and 3.97 Å, for $BiSrZnNbO_6$. As mentioned, $(Bi_{0.5}Sr_{0.5})(Zn_{0.5}Nb_{0.5})O_3$ was synthesized by Kosyachenko and co-workers.[105] They reported a weakly tetragonal structure with lattice parameters a=b=4.002, and c=4.015 Å (c/a=1.003) at 293 K. These values are $\sim$ 0.9 % larger than our calculated LDA lattice parameter. This size of underestimation is typical of LDA errors.

The structure of the 40 atom pseudocubic $BiPbZnNbO_6$ supercell at the LDA equilibrium volume is depicted in Fig. 5.1. As may be seen, there are large off-centerings of the Bi ions and also some octahedral tilting. Fig. 5.2 shows the cation

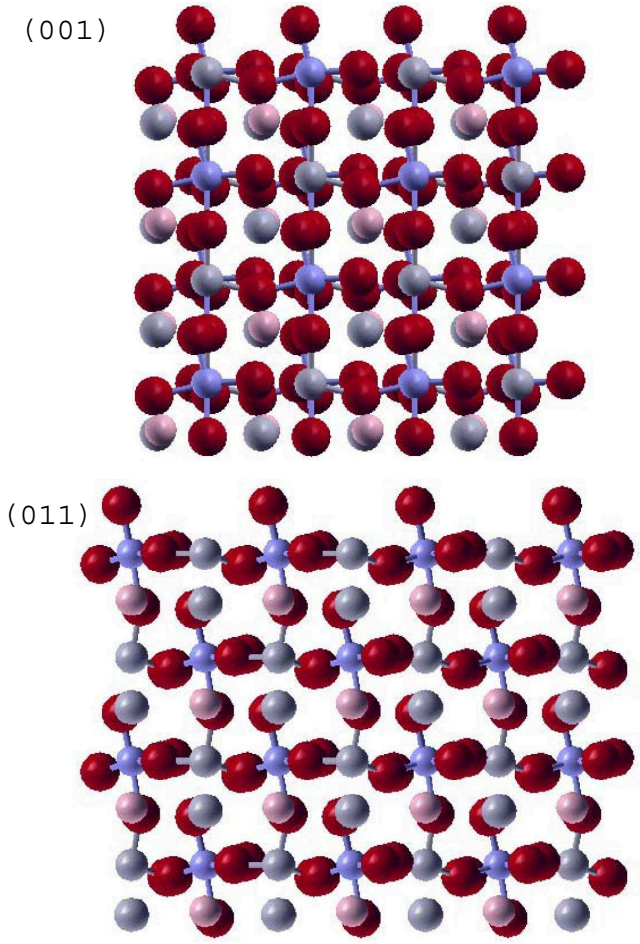

Figure 5.1: (color online) Structure of the 40 atom pseudocubic $BiPbZnNbO_6$ supercell after relaxation. The *B*-site – O bonds are shown. The O ions are shown by (dark) red, Zn by (medium) gray, Nb by smaller (medium) blue, Pb by gray and Bi by (smaller, light) pink spheres. For clarity eight (2x2x2) supercells are shown. The top panel shows a view along (001) and the bottom shows a view along (011). Note that in addition to the cation off-centerings, there are noticeable octahedral tilts.

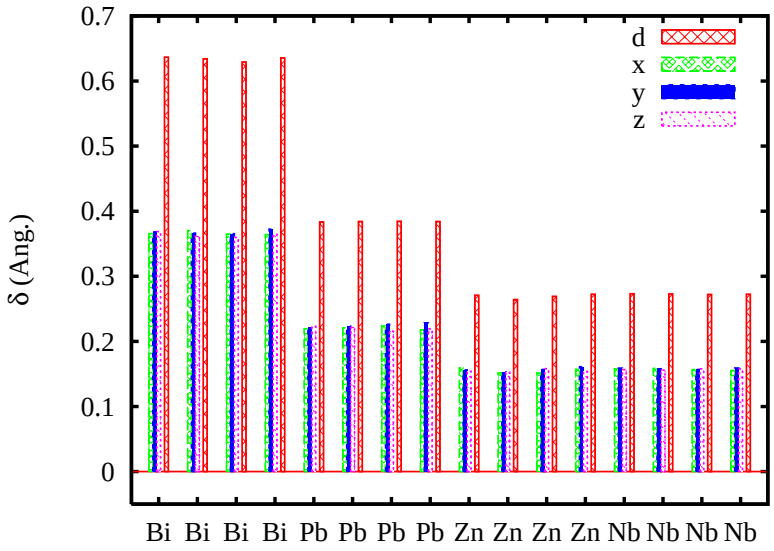

Figure 5.2: (color online) Cation off-centerings along the Cartesian directions with respect to their O cages for the various sites in LDA relaxed structure of the pseudocubic 40 atom supercell of $BiPbZnNbO_6$ at a lattice parameter of 3.99 Å. The total displacement magnitude of each ion is also given.

off-centerings in this cell for the different sites with respect to the centers of their O cages (the 12 nearest O ions for the *A*-site and the 6 nearest for the *B*-site). The largest off-centerings are of the Bi ions, consistent with Fig. 5.1, and what might be expected based on the small size and stereochemical activity of Bi^{3+}. These displacements are large (0.64 Å) and collinear along a [111] direction. Importantly, there are also large collinear displacements of the other cations. The Pb ions displace by $\sim$ 0.39 Å, the Zn by $\sim$ 0.27 Å, and the Nb by $\sim$ 0.27 Å, all very close to [111]. This cooperative nature of the ferroelectricity, where all cations off-center significantly, is a characteristic of good perovskite ferroelectrics such as $KNbO_3$, $BaTiO_3$ and $PbTiO_3$.[103, 68] These displacements would yield a point charge polarization based on nominal charges of 58 $\mu C/cm^2$ using nominal charges, with the largest contributions coming from the Bi and Nb (note the +5 charge state of

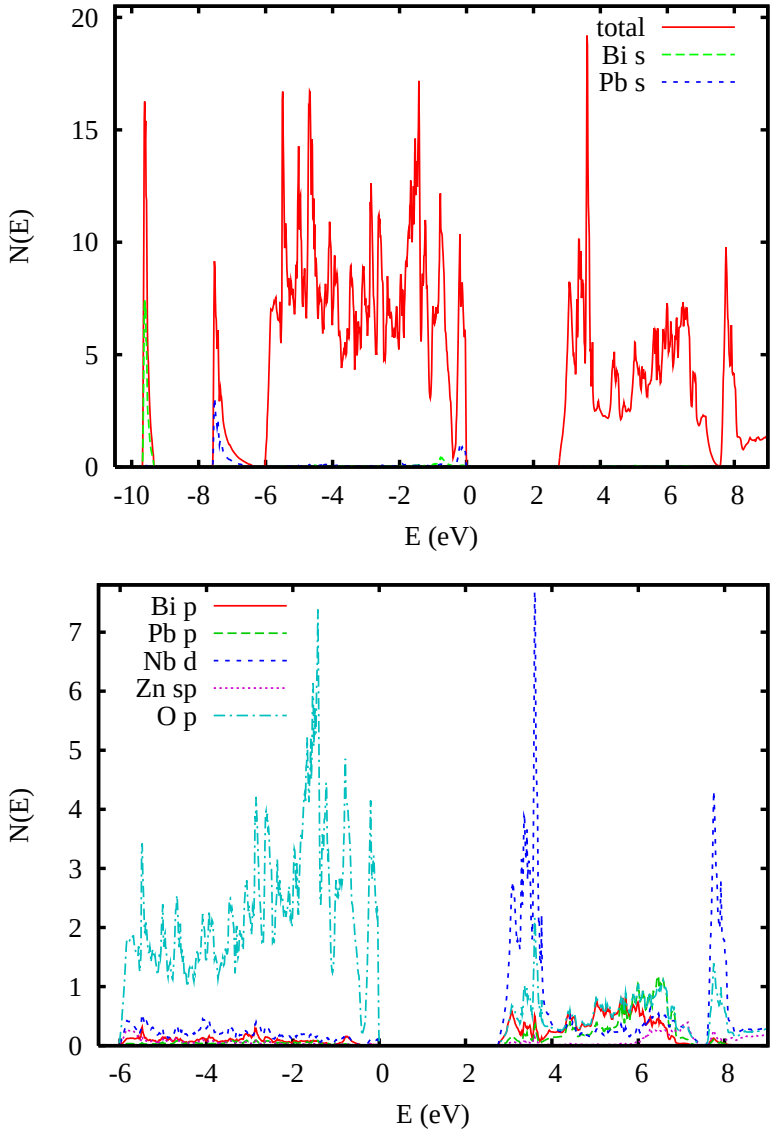

Figure 5.3: (color online) Electronic DOS of the pseudocubic relaxed $BiPbZnNbO_6$ supercell on a per formula unit basis. The top panel shows the total DOS and the Bi s and Pb s projections. The bottom panel shows Bi p, Pb p, Nb d, Zn sp and O p projections. The projections are the integrals of components of the charge density with given angular character within the LAPW spheres. Note that for extended orbitals this gives an underestimate. The energy zero is set at the valence band maximum.

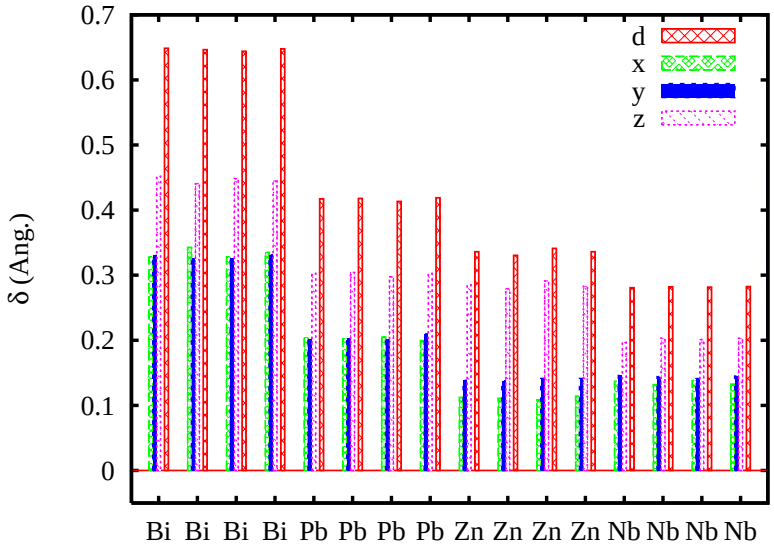

Figure 5.4: (color online) Cation off-centerings along the Cartesian directions with respect to their O cages for the various sites in LDA relaxed structure of the 40 atom supercell of $BiPbZnNbO_6$ at at the same volume as in Fig. 5.2, but with an imposed c/a ratio of 1.0606. Note that despite the large tetragonal strain the cation displacements remain nearly collinear and do remain reasonably close to a [111] direction.

Table 5.1: Average displacements of the cations relative to their O cages in relaxed 40 atom $BiPbZnNbO_6$ cells as a function of pseudocubic lattice parameter, a.

a(Å)	δ_{Bi}(Å)	δ_{Pb}(Å)	δ_{Zn}(Å)	δ_{Nb}(Å)
3.88	0.50	0.28	0.20	0.22
3.92	0.54	0.31	0.23	0.24
3.98	0.62	0.38	0.26	0.27
3.99	0.64	0.39	0.27	0.27
4.03	0.69	0.44	0.30	0.30
4.07	0.75	0.50	0.35	0.32

Nb). The actual polarization is higher (see below) because the nominal charges are enhanced due to covalency.

As is usual in perovskite ferroelectrics, we find that the ferroelectricity is enhanced as the volume is expanded and conversely under compression. However, over the volume range investigated (pseudocubic lattice parameter, 3.88 Å $\leq a \leq$ 4.07 Å), the material remains ferroelectric, with cation displacements along [111]. The average cation displacements as a function of a are given in Table 5.1. The LDA typically underestimates lattice parameters, often by $\sim$ 1–2 %, and as such the prediction of ferroelectricity in this material would seem to be robust against LDA volume errors.

We now discuss the electronic structure as it relates to ferroelectricity. The electronic density of states (DOS) and projections for the relaxed supercell are shown in Fig. 5.3. The calculated LDA band gap is 2.7 eV. This is almost certainly an underestimate due to the LDA band gap error. Considering the sizable gap and the fact that all the ions are in chemically stable valence states it is likely that $BiPbZnNbO_6$ can be made as a good insulator at ambient temperature. This is an important consideration for a ferroelectric material to be used in applications. The stereochemical activity of Bi^{3+} and Pb^{2+} is associated with the lone pair chemistry, which is usually discussed in terms of a high polarizability of the

electrons in the occupied 6s orbitals of these ions. As shown, the Bi 6s states give rise to the DOS peak centered at -9.5 eV relative to the valence band maximum (VBM), while the Pb 6s states are at -7.4 eV. The O 2p bands provide the DOS from -6 eV to the VBM, while the conduction bands are derived from unoccupied orbitals of metal character, primarily Nb 4d, Bi 6p, Pb 6p and at higher energies, Zn sp character. There is a modest hybridization between the Bi and Pb 6s states and the O 2p states as may be seen from the Bi and Pb s character at the top of the O 2p bands. However, this is a mixing of occupied states and as such does not signify chemical bonding. Instead, as has been noted previously for ferroelectric perovskites,[84, 52] the important hybridization is between the O 2p states and unoccupied metal states, which favors ferroelectricity due to chemical bonding and leads to enhanced Born effective charges. The energy position of the Nb 4d states, which are dominant in the lower conduction bands from the conduction band minimum (CBM) to $\sim$ 1.2 eV above it is important because the low energy favors hybridization with O 2p states and ferroelectric off-centering, as was discussed in the case of PMN and $KNbO_3$ in relation to $KTaO_3$.[113, 114] In the present case, there is a strong mixing of O 2p and Nb 4d states. This is evident from the Nb d character in the O 2p bands. The Bi 6p and Pb 6p states, which occur in the conduction bands from the CBM to $\sim$ 4 eV above, also mix strongly with the O 2p bands. There is also cross-gap hybridization evident involving the Zn sp states, although this mixing is weaker perhaps because the Zn states occur further above the CBM. The values of the Born effective charges are enhanced by this cross gap hybridization. The average values for Bi, Pb, Zn and Nb are 4.4, 3.6, 2.9 and 5.8, respectively. The calculated polarization for the supercell is 85 $\mu C/cm^2$. This number was obtained using a Berry's phase calculation. The estimate of the polarization that is obtained by multiplying the Born charges and cation off-centerings in their O cages is 83 $\mu C/cm^2$ in close agreement with the Berry's phase

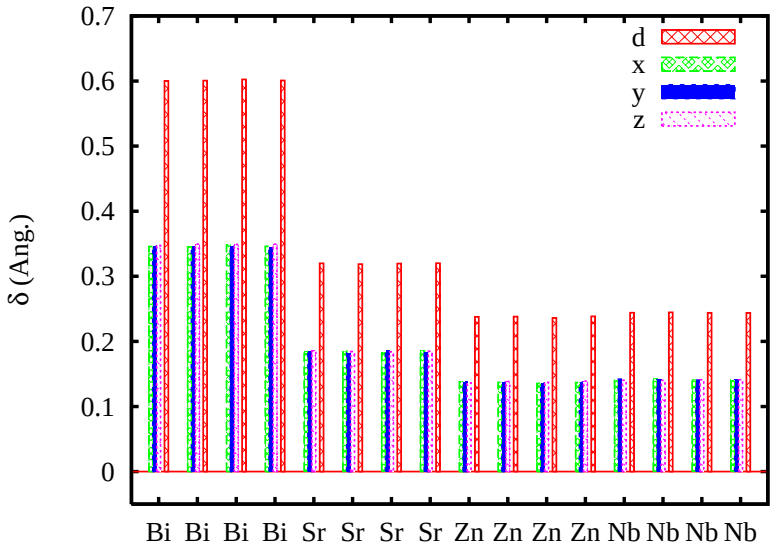

Figure 5.5: (color online) Cation off-centerings along the Cartesian directions with respect to their O cages for the various sites in LDA relaxed structure of the pseudocubic 40 atom supercell of $BiSrZnNbO_6$ at a lattice parameter of 3.97 Å. The total displacement magnitude of each ion is also given. Note the reduced off-centering of Sr relative to Pb (Fig. 5.2) in $BiPbZnNbO_6$, while the off-centerings of the other cations are similar.

calculation. For comparison the polarization of $BiFeO_3$ from DFT calculations is 90 – 100 $\mu C/cm^2$.[93]

The above discussion in terms of cross gap hybridization due to interaction between O $2p$ states and extended, low lying metal orbitals making up the conduction bands is different from a discussion in terms of a polarizable atomic like s orbital. However, it should be emphasized that atomic character is not a uniquely defined quantity since it is basis set dependent (note that an expansion in terms of radial functions times spherical harmonics about a single site is a complete basis, and so expansion about the different sites on a lattice is necessarily overcomplete). Furthermore, polarization of an s orbital implies a mixing in of some p character from unoccupied orbitals, and in these perovskites this is $6p$ character that arises from conduction bands. The distinction between the two views is that in the lone

pair description the discussion is in terms of response to crystal potential as in a discussion of crystal field, while in the cross-gap hybridization it is structure dependent hybridization as in ligand field. This is analogous to the origin of crystal field splittings in transition metal oxide compounds, which arise primarily from hybridization with O $2p$ states and not the non-spherical crystal potential around the metal site.

As mentioned, high piezoelectric coupling in ferroelectric perovskites is generally found near an MPB, most commonly between a pseudocubic phase and a tetragonal phase, as in PZT. We did calculations as a function of imposed tetragonal strain for our supercell at a fixed volume equal to the equilibrium volume for the pseudocubic cell (a=3.99 Å). Over the range considered ($0.992 < c/a < 1.076$), the cation off-centerings stayed collinear and primarily along a [111] direction, and in particular, at least up to the maximum strain considered, did not switch to an [001] average direction. As an example, cation off-centerings for $c/a = 1.0606$ are shown in Fig. 5.4. The lowest energy is at $c/a \sim 1.015$. However, near this minimum the cation displacements remain very close to a [111] direction. Instead it seems that the deviation of c/a from unity is due to the octahedral tilts and not strain coupling for the tetragonal ferroelectric state. Since the tilts are expected to be coupled to the A-site cation ordering, this may very well be an artifact of the specific ordering used in the necessarily small supercell studied here (note that the A-site cations would most likely be disordered in this material). In any case, $BiPbZnNbO_6$ is most likely pseudocubic with a rhombohedral ferroelectric state or weakly tetragonal. As such it may be of interest to investigate the $BiPbZnNbO_6$ – $PbTiO_3$ solid solution to determine whether an MPB is present. We note that the tetragonality may be particularly sensitive to volume, as is the case in $PbTiO_3$, meaning that the LDA volume error may be particularly important for this, and

Table 5.2: Comparison of properties of $BiPbZnNbO_6$ and $BiSrZnNbO_6$ cells as obtained from our LDA calculations. a denotes the pseudocubic lattice parameter, the z^* are the average Born effective charges, δ are the average cation off-centerings with respect to the O cages, and P is the polarization.

	$BiPbZnNbO_6$	$BiSrZnNbO_6$
a(LDA)	3.99 Å	3.97 Å
δ(Bi)	0.64 Å	0.62 Å
z^*(Bi)	4.4	4.4
δ(Pb/Sr)	0.39 Å	0.33 Å
z^*(Pb/Sr)	3.6	2.6
δ(Zn)	0.27 Å	0.25 Å
z^*(Zn)	2.9	2.8
δ(Nb)	0.27 Å	0.25 Å
z^*(Nb)	5.8	5.8
P(111)	85 μC/cm^2	79 μC/cm^2

also that errors due to the use of a small ordered supercell may be particularly important for this.

$BiPbZnNbO_6$ has two A-site ions with stereochemical activity. Bi shows large off-centerings while the Pb off-centerings are smaller, and furthermore Bi carries a higher charge. This raises the question of the role of Pb in the ferroelectricity. This question is also of interest because Pb is considered hazardous. This fact motivates searches for Pb-free replacements for the commonly used Pb-based ferroelectrics such as PZT. We performed calculations for 40 atom $BiSrZnNbO_6$ supercells, similar to those discussed above for the Pb system. Some properties are compared with the Pb system in Table 5.2. We found a slightly smaller equilibrium volume for the Sr system, corresponding to a pseudocubic a=3.97 Å. As shown in Fig. 5.5, the material is ferroelectric, with large collinear cation off-centerings along [111]. The calculated polarization is 79 μC/cm^2. These off-centerings are similar to those for the Pb system, except on the Sr site. This is also the case for calculations at the same volume. For a pseudocubic a=3.98 Å, the calculated off-centerings are 0.62 Å, 0.33 Å, 0.25 Å, and 0.25 Å, for Bi, Sr, Zn and Nb, respectively, as compared with

0.62 Å, 0.38 Å, 0.26 Å, and 0.27 Å, for Bi, Pb, Zn and Nb in the Pb compound at the same volume. This implies only slightly inferior ferroelectric properties for the Sr compound as compared to the Pb compound. The calculated average Born effective charges for $BiSrZnNbO_6$ are 4.4, 2.6, 2.8, and 5.8 for Bi, Sr, Zn, and Nb, respectively. These are very similar to $BiPbZnNbO_6$, except that the Sr Born charge is lower than that for Pb. Importantly, the LDA band gap of the Sr compound, E_g=3.0 eV, is slightly higher than that of the Pb compound. This large band gap combined with the stable valences of the various cations implies that highly insulating samples can be prepared. This may make $BiSrZnNbO_6$ a useful alternative Pb-free ferroelectric.

5.4 Summary and Discussion

Density functional calculations for small supercells of double perovskites $BiPbZnNbO_6$ and $BiSrZnNbO_6$ indicate that these may be useful ferroelectric materials. They have high polarization due to the large displacement of Bi and the displacements of Nb combined with its high charge. They have substantial band gaps and stable chemistry consistent with synthesis of highly insulating samples. It will be of interest to measure properties experimentally, and to investigate the solid solutions with $PbTiO_3$ to determine if a morphotropic phase boundary is present. Finally, we note that because these materials have mixtures of ions with different charges on both the A- and B-sites, they should have considerable chemical flexibility. While we considered $BiPbZnNbO_6$ in the double perovskite structure, $Bi_xPb_{1-x}Zn_{1/3+x/3}Nb_{2/3-x/3}O_3$ may exist over a large range of x. $BiPbZnNbO_6$ is the x=0.5, while x=0 is the known relaxor ferroelectric PZN. To our knowledge, the x=1 perovskite $BiZn_{4/3}Nb_{1/3}O_3$ has not been reported, and instead the Bi_2O_3 – ZnO – Nb_2O_5 system shows Nb rich pyrochlore phases that presumably compete

with the perovskite.[115] As such, it may be possible to synthesize the perovskite under pressure, similar to other low tolerance factor Bi based perovskites.[116, 117] In any case, the chemical flexibility implies a tunability of properties that may be very helpful in obtaining useful ferroelectric properties including MPBs.

Chapter 6

Density functional study of FeS, FeSe and FeTe: Electronic structure, magnetism, phonons and superconductivity

A similar version of this chapter appeared as *"Density functional study of FeS, FeSe and FeTe: Electronic structure, magnetism, phonons and superconductivity"*, Alaska Subedi, Lijun Zhang, David J. Singh and Mao-Hua Du, Phys. Rev. B **78**, 134514 (2008)

6.1 Introduction

Superconductivity was recently reported in α-$FeSe_{1-x}$, with critical temperature $T_c \sim 8$K.[12] This is of interest both because of the fact that Fe containing superconductors are unusual and because this material shares in common square planar sheets of tetrahedrally coordinated Fe with the Fe-As based high temperature

superconductors.[10, 118, 119, 120, 121, 122] α-FeSe occurs in the PbO structure. This consists, as mentioned, of Fe square planar sheets, with Se atoms forming distorted tetrahedra around the Fe very similar to the structure of the FeAs planes in LaFeAsO, $BaFe_2As_2$ and LiFeAs, which are prototypes of the known families of Fe-As based high-T_c superconductors.[11, 123, 124] Since the reported $T_c = 8$K of doped α-FeSe is modest, it is important first of all to establish the relationship between this material and the Fe-As based superconductors.

In this chapter we present density functional calculations that show α-FeSe and the other known Fe based chalcogenides in this structure to be very similar to that of the Fe-As based superconductors.[125] In particular, the Fermi surface consists of small heavy hole cylinders near the zone center and lighter compensating electron cylinders around the zone corner. We show that the stoichiometric compounds are either very close to a spin density wave (SDW) instability (FeS) or have an itinerant spin density wave instability without doping (FeSe) similar to the Fe-As superconductors.[126] We find that ordered SDW state in FeTe has lower energy than the paramagnetic and ferromagnetic states, but more recent neutron scattering experiments by Bao *et al.*[127] and calculations by Ma *et al.*[128] show that FeTe has bicollinear antiferromagnetic order. This suggests band structure effects may be more important for magnetism in FeTe. Calculations of the electron-phonon coupling show that doped FeSe is not an electron-phonon superconductor, similar to what was found for the Fe-As phases.

6.2 First principles methods and Structure

Our calculations of the electronic structure and magnetic properties were performed within the local density approximation with the general potential linearized augmented planewave (LAPW) method,[19] including local orbitals,[110] similar

Table 6.1: Structural parameters and magnetic properties of PbO-structure FeX. The lattice parameters are from experimental data, while the internal chalcogen structural parameter, z_X is from LDA structure minimization. m_{SDW} is the spin moment within the Fe LAPW sphere (radius 2.1 a_0) for the SDW state and E_{SDW} is the energy per Fe of this state relative to the non-spin-polarized state in meV/Fe. $N(E_F)$ is the density of states at the Fermi energy in the non-spin-polarized band structure in eV^{-1} on a per Fe both spins basis.

	a(Å)	c(Å)	z_X	$N(E_F)$	$m_{SDW}(\mu_B)$	E_{SDW}
FeS	3.6735	5.0328	0.2243	1.35	0.00	0
FeSe	3.765	5.518	0.2343	0.95	0.65	5
FeTe	3.8215	6.2695	0.2496	1.83	1.28	47

to our previous calculations for the Fe-As based superconductors.[125, 129, 130] We used LAPW spheres of radius 2.1 a_0 for Fe, Se and Te and 1.9 a_0 for S. These compounds occur in a simple tetragonal structure with one internal parameter, z_X corresponding to the chalcogen height above the Fe square plane. The experimental lattice parameters[12, 131, 132] were employed and we relaxed the chalcogen height via energy minimization. The structural parameters used and some results are presented in Table 6.1. The electron-phonon coupling and phonon dispersions were on the other hand obtained using linear response, again with the experimental lattice parameters, with the Quantum Espresso code[31] within the generalized gradient approximation of Perdew, Burke and Ernzerhof.[29] The linear response calculations were done using ultrasoft pseudopotentials for Fe, and norm conserving pseudopotentials for Se. We used a 50 Ry basis set cutoff and a high 500 Ry cutoff for the charge density expansion. This was needed in order to obtain convergence in the linear response calculations.

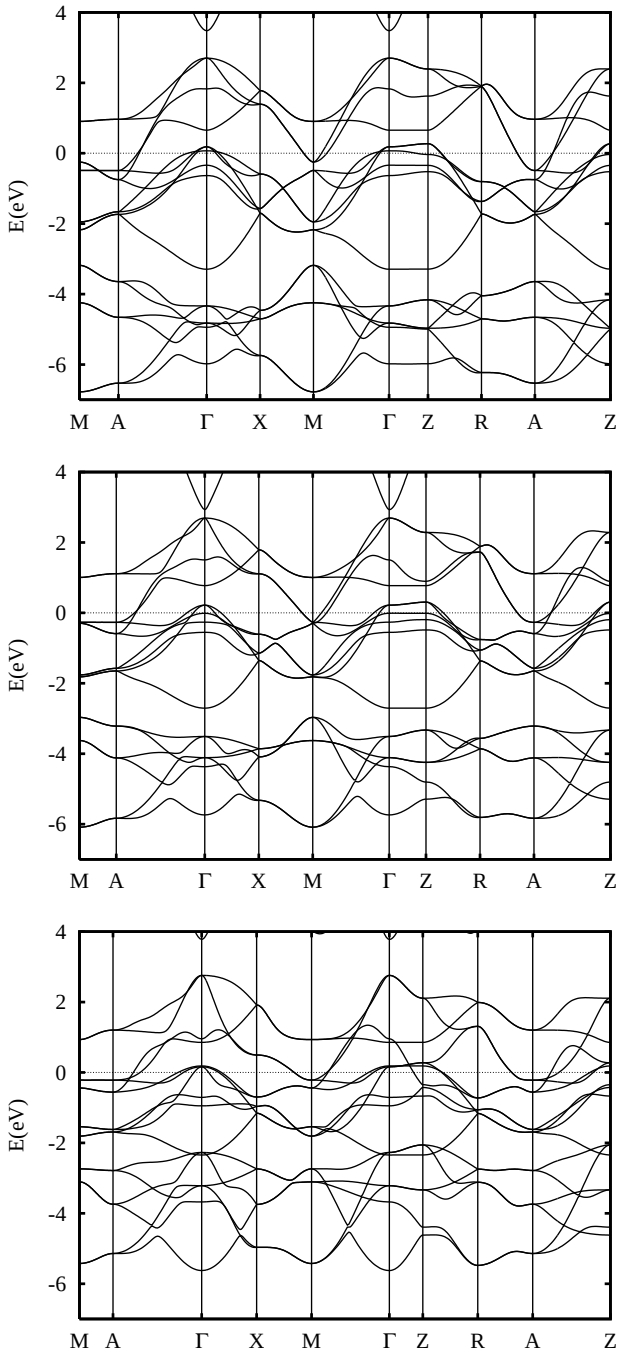

Figure 6.1: Band structures of FeS (top), FeSe (middle) and FeTe (bottom) from non-spin-polarized calculations with the LDA relaxed X heights. The band structures are plotted along the path $(\frac{1}{2},\frac{1}{2},0) \rightarrow (\frac{1}{2},\frac{1}{2},\frac{1}{2}) \rightarrow (0,0,0) \rightarrow (0,\frac{1}{2},0) \rightarrow (\frac{1}{2},\frac{1}{2},0) \rightarrow (0,0,0) \rightarrow (0,0,\frac{1}{2}) \rightarrow (0,\frac{1}{2},\frac{1}{2}) \rightarrow (\frac{1}{2},\frac{1}{2},\frac{1}{2}) \rightarrow (0,0,\frac{1}{2})$.

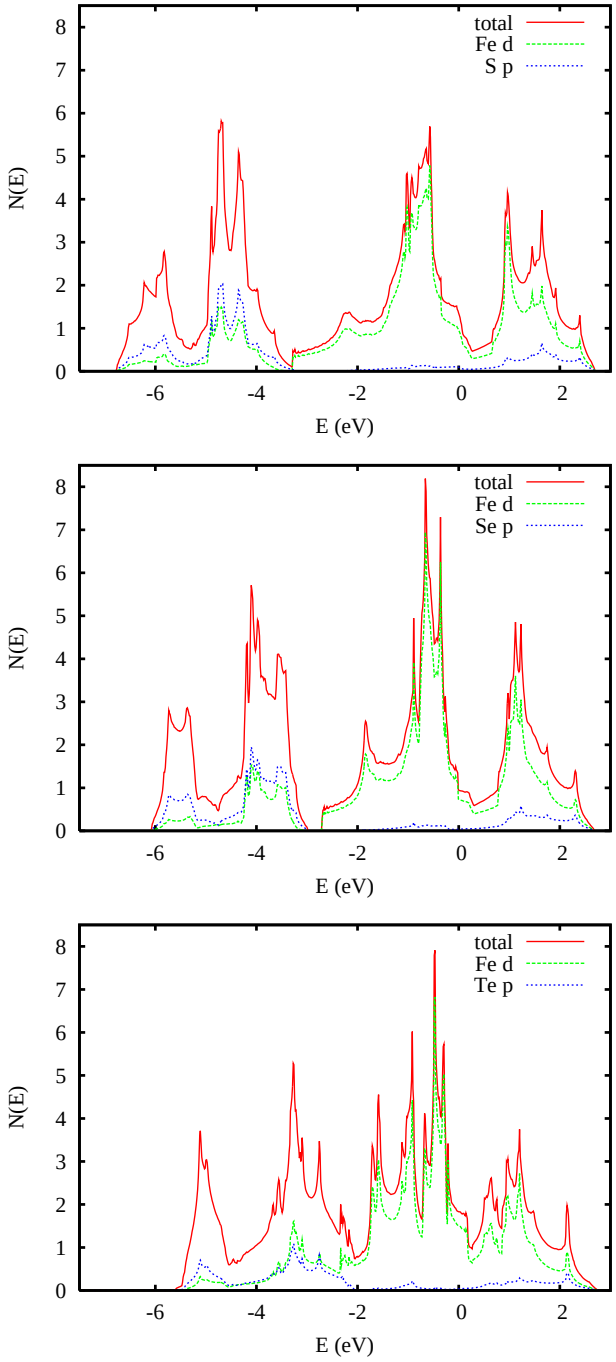

Figure 6.2: (color online) Electronic DOS and projection onto the LAPW Fe and chalcogen spheres indicating the Fe d and chalcogen p contributions for FeS (top), FeSe (middle) and FeTe (bottom) as in Fig. 6.1.

6.3 Electronic structure, Phonons and Magnetism

Our main results for the electronic structure are given in Figs. 6.1, 6.2 and 6.3, which show the non-spin-polarized band structures, electronic densities of states and Fermi surfaces of FeS, FeSe and FeTe. The calculated values of $N(E_F)$ are given in Table 6.1. The phonon dispersions of FeSe are shown in Fig. 6.4. One interesting feature of the phonon dispersion is that they have little dispersion in the k_z and e.g. are very flat along the tetragonal Γ-Z direction. This presumably reflects anion-anion repulsion, which leads to long bonds between the FeSe layers. the result is that there may be an easy cleavage plane between the Se ions, which may facilitate preparation of clean surfaces for experiments such as photoelectron spectroscopy.

The phonon density of states, $G(\omega)$ and electron-phonon spectral function, $\alpha^2F(\omega)$ are given in Fig. 6.5. The electron-phonon coupling constant for FeSe as obtained in linear response is $\lambda = 0.17$ with ω_{log}=113 cm^{-1}. No superconductivity at any temperature even approaching 1K results with these values within standard electron-phonon theory even if very low values of the Coulomb parameter, e.g. $\mu^* = 0.10$ are used in the Allen-Dynes equation. This is similar to what was found previously for LaFeAsO.[133, 129] Therefore we conclude that FeSe is not a conventional electron-phonon superconductor.

Turning to the electronic structure we find a strong qualitative similarity between these materials and the FeAs-based superconductors. In particular, we find these to be low carrier density metals, with high density of states. This arises from band structures that are closely related to those of the FeAs materials. The chalcogen p states lie well below the Fermi level and are only modestly hybridized with the Fe d states as may be seen from the projected DOS (Fig. 6.2). Thus the

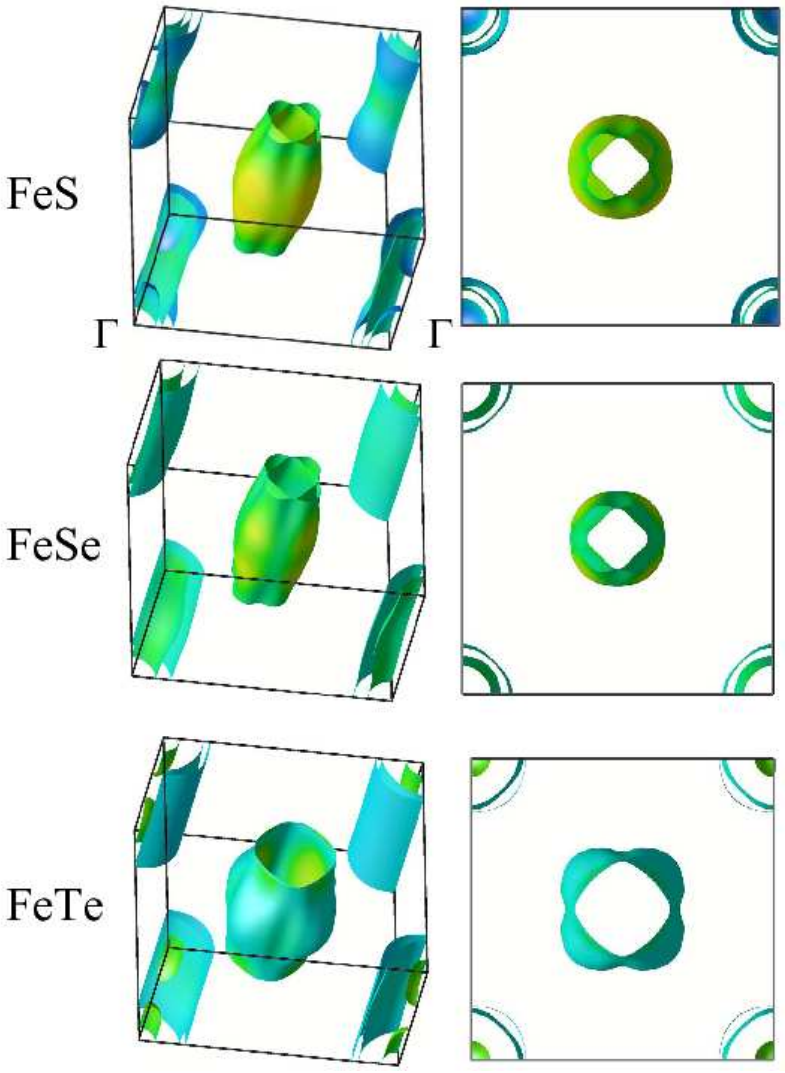

Figure 6.3: (color online) LDA Fermi surface of FeS, FeSe and FeTe from non-spin-polarized calculations with the LDA relaxed X heights. The corners are Γ points.

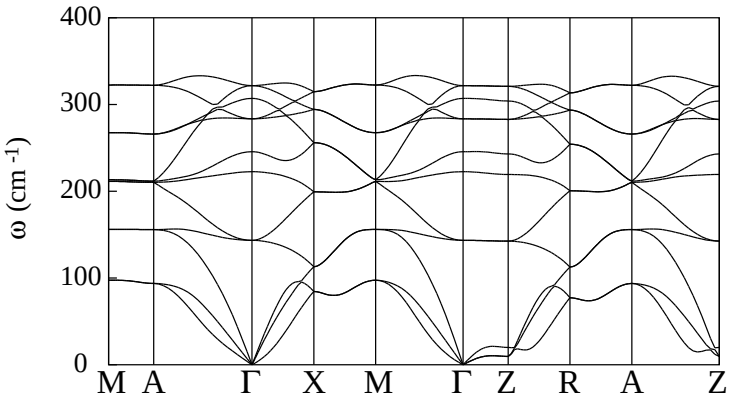

Figure 6.4: Calculated GGA phonon dispersions of non-spin-polarized FeSe along the path $(\frac{1}{2},\frac{1}{2},0) \rightarrow (\frac{1}{2},\frac{1}{2},\frac{1}{2}) \rightarrow (0,0,0) \rightarrow (0,\frac{1}{2},0) \rightarrow (\frac{1}{2},\frac{1}{2},0) \rightarrow (0,0,0) \rightarrow (0,0,\frac{1}{2}) \rightarrow (0,\frac{1}{2},\frac{1}{2}) \rightarrow (\frac{1}{2},\frac{1}{2},\frac{1}{2}) \rightarrow (0,0,\frac{1}{2})$.

electronic structure near the Fermi energy derives from metallic Fe^{2+} layers, with direct Fe-Fe interactions. These are embedded inside a largely ionic background which imposes a competing tetrahedral crystal field. As in the Fe-As based materials, there is a pseudogap at an electron count of 6 d electrons per Fe, and E_F lies near the bottom of this pseudogap. We emphasize that this is not the position of a tetrahedral crystal field gap, which would be at 4 electrons, and emphasizes the fact that Fe chalcogen hybridization is not strong compared with the Fe-Fe interactions. This explains the similarity of the electronic structure to that of the FeAs-based materials, which were also found to be substantially ionic in similar calculations.[125]

These band structures yield two intersecting elliptical cylindrical electron Fermi surfaces at the zone corner in all three materials. These are compensated by lower velocity hole sections at the zone center – two concentric hole cylinders, and in the case of FeS and FeTe a small closed hole section inside the inner cylinder. This is qualitatively very similar to the FeAs-based materials. It is important to note that cylinders at the zone center and zone corner, if they are the same

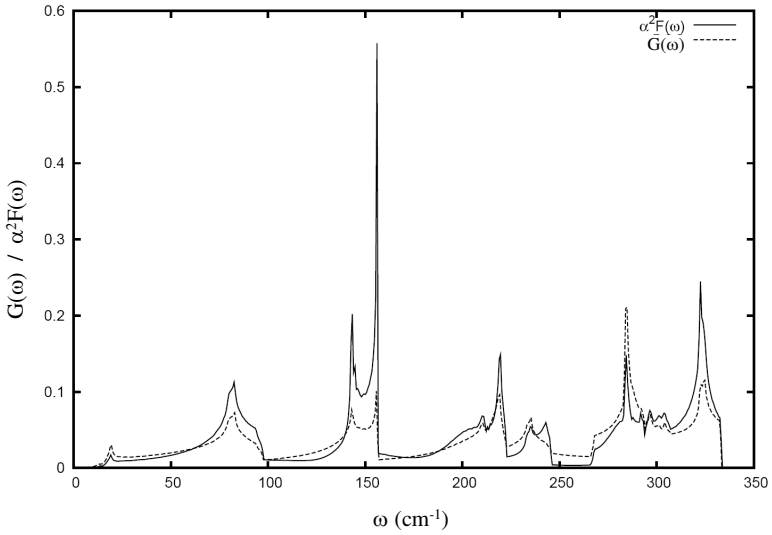

Figure 6.5: Calculated GGA phonon density of state $G(\omega)$ and electron-phonon spectral function $\alpha^2F(\omega)$ for FeSe.

size, would yield strong nesting peaked at the 2D (π,π) point. This will lead in general to enhanced spin fluctuations at the nesting vector, and if sufficiently strong will cause a spin density wave. In fact, an ordered SDW was found both in first principles calculations and in experimental studies for LaFeAsO and many other undoped FeAs-based compounds.[129, 126, 134, 135, 136, 137, 138, 139] There is a clear competition between the SDW and the superconducting state in that superconducting samples generally do not show the SDW, while samples with the SDW transition, generally do not show superconductivity. The ground state is an antiferromagnetic cell doubled along the [11] in plane direction to yield linear chains of nearest neighbor like spin Fe atoms arranged antiferromagnetically, although the values of the moments are dependent on details, especially the As height above the Fe plane.[140, 141, 142, 143, 144, 145]

6.4 Discussion

Turning to the trends, the size of the pseudogap is approximately the same in FeSe and FeS, but is significantly smaller in FeTe. Specifically, there is a greater overlap between the hole and electron bands in the latter compound. This leads to larger Fermi surfaces. The value of $N(E_F)$=1.83 eV^{-1} is also highest in this compound, although it is still lower than the 2.62 eV^{-1} that is obtained for LaFeAsO by the same approach. We used a supercell approach to investigate the SDW with the chalcogen heights fixed to the values calculated by non-spin-polarized energy minimization. We find instabilities for FeSe and FeTe, but not for FeS. The spin moments and the energy of the SDW relative to the non-spin-polarized state are given in Table 6.1. As may be seen the SDW is considerably stronger in FeTe than in FeSe, with an energy gain of 47 meV/Fe and a spin-moment of 1.3 μ_B. The corresponding values for LaFeAsO, calculated in the same way are E_{SDW}=11 meV/Fe and m_{SDW} = 1.0 μ_B in a 2.1 a_0 Fe sphere. However, more recent neutron experiments[127] and calculations[128] show that FeTe has a bicollinear antiferromagnetic order, indicating band structure effects may be more important for magnetism in this compound. Besides the SDW, we find a borderline ferromagnetic tendency in FeTe, without doping when the SDW is not allowed, similar to LaFeAsO.[125] We do not find ferromagnetic instabilities in either FeSe or FeS, consistent with the lower values of $N(E_F)$ in those materials. The sensitivity of the moment size to the ordering pattern underscores that fact that these are itinerant magnetic systems in the LDA, as opposed to local moment magnets. This means that magnetic ordering is driven by electrons at and near the Fermi surface. On the other hand this is not to say that spin fluctuations are weak in the paramagnetic state above the SDW ordering temperature or the paramagnetic state as realized by doping. In fact, as noted, several authors have

found that the As height in the Fe-As compounds is strongly coupled to magnetism and so strong spin fluctuations in the paramagnetic state would help rationalize the underestimated As height in non-spin-polarized LDA calculations.[140, 141, 142, 143, 145] In fact, there is evidence for strong spin fluctuations in the normal state of the FeAs compounds, e.g. from temperature dependent resistivity data indicating strong scattering above the SDW ordering temperature (note a drop in resistivity below the SDW ordering temperature even though the carrier density is strongly reduced),[146] as well as from spectroscopy.[147] The size of the effects observed implies that these fluctuations should have large amplitudes and therefore unlike the SDW should be rather diffuse in **q**-space, which might make them hard to directly observe.* Furthermore, the strong transport signatures especially the enhanced resistivity above the ordering temperature imply substantial coupling between spin flucuations and electrons at the Fermi energy, which is indicative of the itinerant nature of the magnetism.

We emphasize also that our results in Table 6.1 are at the LDA relaxed atomic positions for the non-spin-polarized states. These systems become more magnetic as the chalcogen height is raised. In the case of FeS a recent refinement is available, and gives z_S=0.2602.[131] This puts the S ions 0.18 Å higher than in the LDA structure. With this value we find a stable SDW for FeS, with a moment of 1.2 μ_B/Fe. This is the same trend as in the Fe-As based superconducting materials.

*In a system with strong magnetic tendencies ordering will normally occur at high temperature unless there is a large **q** space for fluctuations, e.g. due to frustration, itinerant electron physics or competing exchange interactions. It is difficult to avoid ordering with large amplitude spin fluctuations if they are they are strongly peaked, e.g. at the SDW nesting vector, or are subject to a simple exchange model that favors a specific ordering pattern, such as a nearest neighbor antiferromagnetic interaction on the square lattice (with 3D interactions or magnetoelastic coupling as a present here). Also, in the case where there is large phase space for fluctuations, local magnetic correlations will be very short range. This does not mean however that the fluctuations will necessarily be fast or only at high energy and in fact near a quantum critical point there will be slow fluctuations that extend to low energy. One experimental signature of such fluctuations besides the magneto-structural effects noted, will be via transport data and in particular data that show nearness to a quantum critical point through non-Fermi liquid scalings.

The result may be taken as an indication that in fact FeS may have a spin density wave as well and at least that there will be strong spin fluctuations in FeS as well as the other PbO-structure Fe chalcogenides.

As mentioned, cylindrical Fermi surface sections of equal volume will be nested with nesting vector equal to the separation of the centers of these cylinders. This nesting can be reduced by imperfect matches in shape, three dimensionality, and size mismatch. Size mismatch can arise both from additional Fermi surface sections, such as the extra small hole sections obtained in FeS and FeTe, but not FeSe, or from doping. In particular, electron doping will reduce the size of the hole sections and increase the size of the electron sections consistent with Luttinger's theorem.

The mechanism for superconductivity in the Fe-As based phases has not yet been established. Nonetheless, there are indications that magnetism is associated with superconductivity. These include the modest electron phonon couplings in the materials, the proximity to magnetism and the phase diagrams which show an association between the SDW and superconductivity. We discuss our results within a general spin fluctuation mediated framework.[148, 149, 129, 150] In general an itinerant SDW instability arises from a divergence of the real part of the susceptibility $\chi(\mathbf{q})$ at a specific wavevector $\mathbf{q}$. Superconducting pairing is also associated with the real part of $\chi(\mathbf{q})$ through an integral over the Fermi surface. $\chi(\mathbf{q})$ for $\mathbf{q}$ connecting different parts of the Fermi surface can contribute to pairing. As a result, when the Fermi surfaces are small and disconnected as in these Fe based materials, the fluctuations associated with nesting will provide substantial interband pairing between the electron and hole sections, but will not provide substantial intraband pairing.[129, 150] As the nesting is reduced, e.g. by doping, $\chi(\mathbf{q})$ will spread out while the peak value will be reduced, consistent with the destruction of the SDW. For circular cylinders of radii differing by δq, $\chi(\mathbf{q})$ will

show a plateau of high $\chi(\mathbf{q})$ around the nesting vector with width $2\delta q$ (this will persist until the radii differ by a factor of two at which point the center of the plataeu will dip). This means that the two cylinders will still be connected by spin fluctuations associated with their now reduced nesting, and therefore even though the SDW will be suppressed by the reduction in the maximum value of χ the associated spin fluctuations can still provide superconducting pairing. We emphasize that in this general framework the same parts of the Fermi surface are affected by the SDW and by the superconducting pairing. Thus these two Fermi surface instabilities compete for the same Fermi surface and therefore that there should be at best little coexistence of these two orders.

6.5 Summary and Conclusions

We report electronic structures, magnetic properties and electron-phonon calculations for FeX, X=S,Se,Te. We find strong similarities to the Fe-As based superconductors, reflecting the ionic nature of the As and chalcogen atoms in these compounds. As in the arsenides, we find that the electron-phonon coupling cannot explain the superconductivity, and furthermore that these compounds display itinerant magnetism. These results imply a similar superconducting nature for the Fe-As phases and FeSe.

Chapter 7

Quantum criticality in $NbFe_2$

A similar version of this chapter appeared as *"Band Structure and Itinerant Magnetism in Quantum Critical $NbFe_2$"*, Alaska Subedi and David J. Singh, Phys. Rev. B **81**, 024422 (2010).

7.1 Introduction

There has been considerable recent interest in metals near magnetic quantum critical points both because new ground states such as superconductivity and nematic phases that have been reported in some as well as improved materials preparation and experimental techniques that allow detailed characterization of these phases including the unusual scalings of properties near the critical point.[151] Iron compounds are of particular interest because of the recent discovery of high temperature superconductivity in iron compounds near magnetism,[10] with a possibly magnetic pairing mechanism.[129]

The hexagonal C14 hexagonal Laves phase compound $NbFe_2$ was thought to be either paramagnetic or very weakly ferromagnetic until 1987.[152, 153] However, nuclear magnetic resonance (NMR) experiments by Yamada and Sakata found

$NbFe_2$ to be a weak antiferromagnet with $T_N \sim 10$ K and $M \sim 0.1\mu_B$.[13] The antiferromagnetic state is very sensitive to stoichiometry and the material becomes ferromagnetic by slight over-doping of either Nb or Fe, indicating the existence of a quantum critical point (QCP) at or very close to stoichiometric $NbFe_2$. The proximity to quantum criticality is also seen in the non-Fermi liquid behavior of specific heat capacity and resistivity. Wada and co-workers reported that the electronic specific heat is substantially enhanced,[154] and more recently it was found that the Sommerfeld coefficient in fact shows logarithmic dependence $\gamma \propto -\log T$ at low temperatures.[155, 156, 157, 158] The low temperature resistivity meanwhile shows a behavior $\rho \propto T^{3/2}$. Furthermore, $NbFe_2$ shows a substantial exchange splitting of the Fe $3s$ core level, in spite of having a very low ordered moment.[159] This is a feature shared in common with the iron based superconductors.[160]

$NbFe_2$ has the hexagonal C14 structure with Nb at $4f(1/3, 2/3, x)$ and Fe at $2a(0, 0, 0)$ and $6h(y, 2y, 3/4)$. A unit cell of $NbFe_2$ consists of four formula units and has a layered structure as shown in Fig. 7.1. One layer is formed by hexagonal sheet of Fe at site $6h$. Another layer consists of Nb at site $4f$ and Fe at site $2a$. The Nb atoms reside in Fe cages. Fe atoms at site $6h$ form Kagome lattice sheets as shown in Fig. 7.2. Therefore there are two types of Fe atoms, which may behave differently from a magnetic point of view. In the related compound, $TiFe_2$, neutron scattering measurements have shown that Fe on the $6h$ sites form ferromagnetic sheets, which are stacked antiferromagnetically, while there is no moment on the $2a$ Fe sites.[161] Furthermore, it has been reported that in that material there is a competition between ferromagnetic and antiferromagnetic ground states both from density functional calculations and experimental measurements in samples with quenched disorder.[162, 163] This indicates that the $2a$ site may play an important role in the magnetism of $TiFe_2$ even though it does not have ordered moments.

It has been argued that the magnetic behaviors of the different C14 Laves $T\mathrm{Fe}_2$ compounds, where T is an early transition metal, are closely related,[164] and so one may conjecture that NbFe_2 is similar to TiFe_2. On the other hand, the presence of Kagome sheets in a material near a quantum critical point is suggestive of different physics since strong geometric frustration would be present if there were dominant near neighbor antiferromagnetic interactions in the sheets. In fact, the nature of magnetism at and in the vicinity of the quantum critical point is under debate. Further NMR studies have confirmed Yamada and Sakata's result,[165, 14, 166] but neutron studies have not identified the magnetic order owing to very small magnetic moment and difficulty in growing clean single crystal samples.[155, 158] It has been presumed that the antiferromagnetism is of the spin density wave (SDW) type,[165] but an explanation based on frustration of Fe layers with Kagome type arrangement has also been proposed.[167] As NbFe_2 shows rich interplay of different type of magnetism within a small composition region, this system provides a good opportunity to study ferromagnetic quantum criticality and the precise nature of critical phenomena of the quantum critical point.

7.2 First principles calculations

Here, we present the results of first principles calculations on stoichiometric NbFe_2. Our electronic structure calculations were performed within the local spin density approximation (LSDA) using the general potential linearized augmented planewave (LAPW) method[19] as implemented in our in-house code. This is a full potential method with a flexible basis and no shape approximations to either the potential or charge density. The core states were treated relativistically, while for the valence states a scalar relativisitic method was used. We used LAPW spheres of radii $2.2a_0$ for Nb and Fe. A well converged basis set with cutoff, K_{max}=$9.0/R_{min}$, where

R_{min} is the minimum sphere radius was employed. Additional local orbitals were used to treat the Fe $3s$ and $3p$, and Nb $4s$ and $4p$ states with the valence states. e used Brillouin zone samplings derived from an 8x8x8 grid for the self consistent calculations, and did tests with a doubled 16x16x16 grid. The Fermi surfaces and densities of states shown were obtained using a 32x32x32 grid of first principles band energies. A denser interpolated 72x72x72 grid based on the 32x32x32 grid of first principles data was used for the Lindhard function. We used the experimental lattice parameters, a=4.838 Å, and c=7.889 Å,[168] but relaxed the atom positions in the unit cell. The calculated atomic position parameters were $x = 0.0660$ and $y = 0.1705$. For comparison, the experimental parameters are $x = 0.0629$ and $y = 0.1697$.

We find that magnetism of $NbFe_2$ is itinerant and obtain calculated moments that are much larger compared to experimental values. This type of error, in which the LSDA overestimates the stability of magnetic states is uncommon, but is found generally in materials near magnetic quantum critical points. It indicates that the effect of beyond mean field renormalizations (i.e. renormalization due to quantum spin fluctuations) which reduce the moment from the static LSDA value, is large. This type of renormalization of moments is also found in $ZrZn_2$,[169] and Ni_3Al,[170] and indicates crucial role of spin fluctuations that are presumably associated with the QCP. In any case, the LSDA moments for $NbFe_2$ are found to depend on ordering and go to zero for some configurations, implying an itinerant nature for the magnetism. Furthermore, an analysis of the energetics shows that there are strong Fe-Fe interactions that compete with each other. Among the various magnetic ordering configurations we studied, we find ferrimagnetic ordering, has the lowest energy. From a symmetry point of view ferrimagnetism is the same as ferromagnetism in that there is a net magnetization.

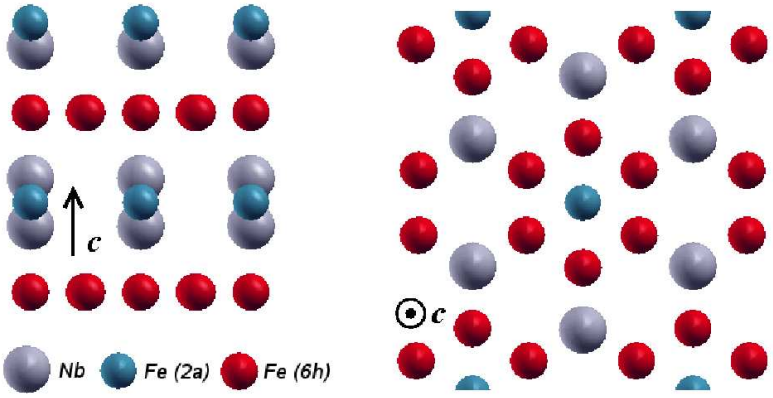

Figure 7.1: (color online) Crystal structure of $NbFe_2$ viewed along the b- and c-axes.

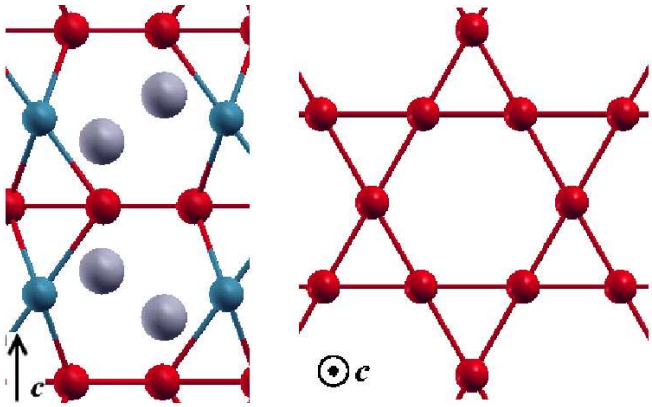

Figure 7.2: (color online) (Left) Crystal structure of $NbFe_2$ showing Nb atoms inside Fe cage. (Right) Kagome lattice layer formed by Fe at site $6h$.

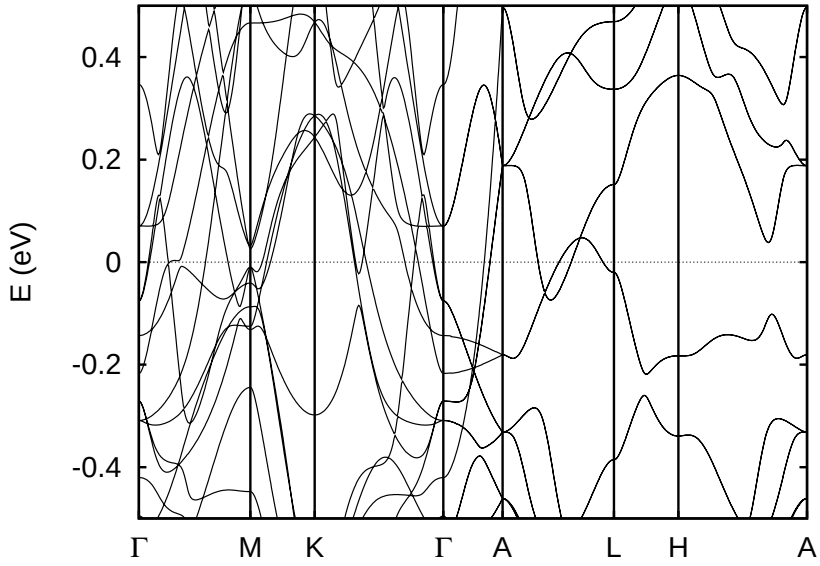

Figure 7.3: Calculated band structure of non-spin-polarized $NbFe_2$ along the path (0,0,0) → ($\frac{1}{2}$,0,0) → ($\frac{1}{3}$,$\frac{1}{3}$,0) → (0,0,0) → (0,0,$\frac{1}{2}$) → ($\frac{1}{2}$,0,$\frac{1}{2}$) → ($\frac{1}{3}$,$\frac{1}{3}$,$\frac{1}{2}$) → (0,0,$\frac{1}{2}$). The Fermi energy is at 0 eV.

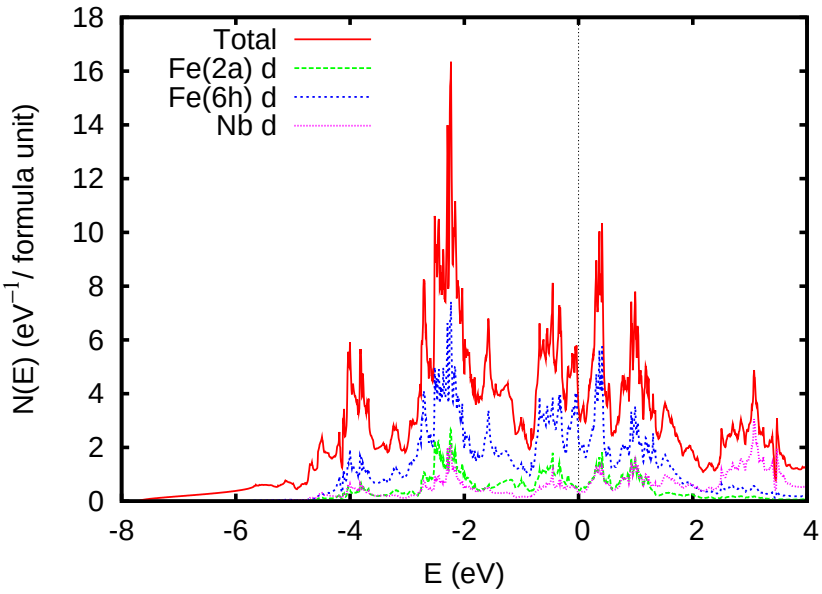

Figure 7.4: (color online) Electronic density of states of non-spin-polarized $NbFe_2$. The Fermi energy is at 0 eV.

Our results for the electronic structure and density of states (DOS) without spin polarization are shown in Figs. 7.3 and 7.4, respectively. The general features of these are similar to the results obtained by Ishida *et al.* in Ref. [171] using Koringa-Kohn-Rostoker (KKR) method. However, there are differences in the dispersion of bands and the band crossings at the Fermi level, presumably reflecting the use of shape approximations in the KKR methodology, as compared to the full potential LAPW approach. For example, the small Fermi surface at Γ is a hole section in our calculations, but is a small electron section in the KKR calculations. The electronic density of states of this material has also been calculated by Terao *et al.*,[172] Takayama *et al.*,[173] and Inoue *et al.*[174] These are qualitatively similar to our results but have different value for DOS at the Fermi energy. From the calculations, we find that most of the s and p bands lie well below Fermi level. The lowest three valence bands, starting at $\sim$ -8 eV with respect to E_F, are light and have mainly Fe sp character. The remaining bands above these are derived from mainly d orbitals of Nb and Fe. These bands are more flat as may be expected and give rise to peaks in DOS. The Fermi level lies near the bottom of one of these peaks with $N(E_F) = 3.5$ eV^{-1} per formula unit both spins. Within Stoner theory,[175] a material has ferromagnetic instability when $NI > 1$. Here N is the density of states at E_F on a per Fe per spin basis, $N = 3.5/4$ eV^{-1} per Fe per spin. Using the typical value of $I \sim 0.7 - 0.9$ eV for Fe d electrons,[176, 177] this gives a Stoner enhancement $(1 - NI)^{-1} \sim 3$, which puts $NbFe_2$ away from a ferromagnetic Stoner instability (this is an instability where all Fe atoms polarize together) but still indicates significant renormalization and the possibility of ferromagnetic spin fluctations. Furthermore the Fermi level lies near the bottom of a valley. The density of states increases strongly below E_F. Above E_F on a large scale (0.1 eV) the density of states is flat followed by a steep increase. Therefore hole doping will

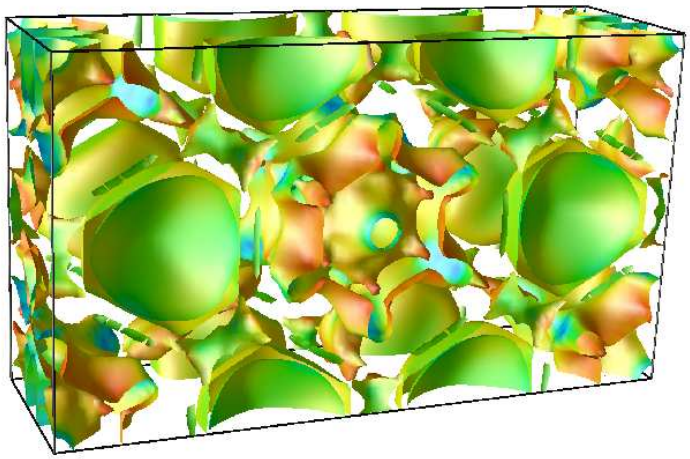

Figure 7.5: Fermi surface of non-spin-polarized $NbFe_2$. The figure contains two Brillouin zones and the shading is proportional to contribution of Fe at $6h$ site with red and blue indicating high and low values, respectively.

increase $N(E_F)$ and likely move the system closer to a ferromagnetic instability and more importantly disorder will increase the effective $N(E_F)$.

As may be seen, there are several bands crossing the Fermi energy. $NbFe_2$ has a large, three-dimensional and multi-sheet Fermi surface as shown in Fig. 7.5. The Fermi velocities are in fact rather isotropic, v_{xx}=0.96x10^5 m/s in-plane, and v_{zz}=1.07x10^5 m/s in the c-axis direction. This argues against explanations of the magnetic behavior based on two dimensionality. This also argues against explanations in terms of frustration on the 2D Kagome sheets, since the material is effectively 3D (also as discussed below, we do not find nearest neighbor antiferromagnetism on the sheets, which again argues against this explantion).

Previous theoretical studies on the nature of magnetism in $NbFe_2$ have yielded disparate results. Ishida *et al.* found that $NbFe_2$ does not fulfill Stoner condition and suggested a paramagnetic ground state.[171] On the other hand, Asano *et al.* calculated total energy as a function of lattice constant and magnetic moment, and found an antiferromagnetic state to have the lowest energy.[178] However, they

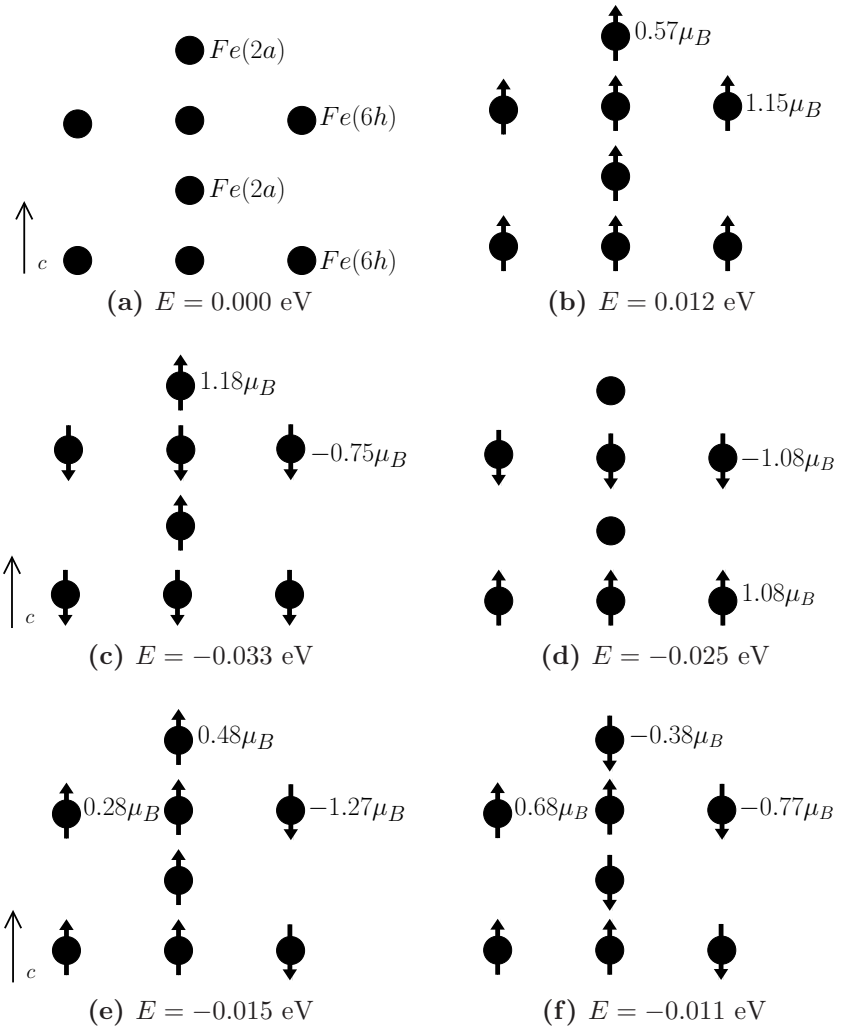

(a) $E = 0.000$ eV **(b)** $E = 0.012$ eV

(c) $E = -0.033$ eV **(d)** $E = -0.025$ eV

(e) $E = -0.015$ eV **(f)** $E = -0.011$ eV

Figure 7.6: Cartoons depicting various spin configurations of Fe in $NbFe_2$. Only Fe atoms are shown.

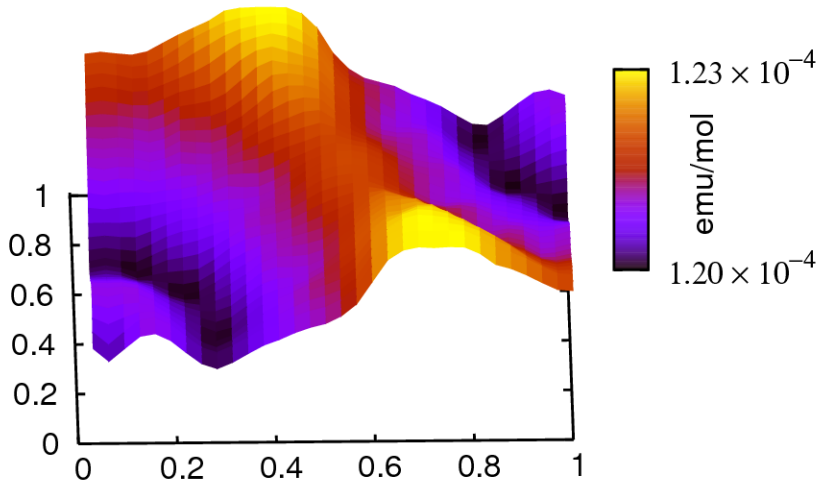

Figure 7.7: (color online) The real part of the Lindhard susceptibility $\chi_0(q, \omega \rightarrow 0)$ for the plane $(q_x, q_y, 0.38)$ that contains the maximum value. For comparison, the susceptibility for $q = (0, 0, 0)$ is $\chi_0(0) = 1.13 \times 10^{-4}$ emu/mol.

also found the antiferromagnetic state to be energetically close to two other type of ferromagnetic states.

We did calculations for various spin configurations as shown in the cartoons in Fig. 7.6. We only studied collinear magnetic ordering cases and the direction of moment on each atom is indicated by an arrow. The cartoons also show the moments on Fe atoms as defined by the spin density within the Fe LAPW spheres. We have only shown Fe atoms in our cartoons as the induced moments on the Nb atoms were small compared to the moments on Fe atoms. The ground state energy per formula unit is given relative to that of the non-spin-polarized case, which is shown in Fig. 7.6a. Fig. 7.6b illustrates the case when spins of all Fe atoms are aligned in the same direction. The moments on Fe $2a$ and $6h$ atoms are 0.57 μ_B and 1.15 μ_B, respectively. The energy is +0.012 eV relative to the non-spin-polarized case. Hence, this configuration is energetically unfavorable and in fact is metastable with respect to the non-spin-polarized case. However, a state where the $6h$ and $2a$ sites have moments in opposite directions has the same symmetry

and is more favorable. Fig. 7.6c depicts this ferrimagnetic case. The energy of this state is −0.033 eV, which is also the lowest among all the orderings we studied. In this solution the moment on each 2a site is 1.18 μ_B, while each 6h Fe has 0.75 μ_B in the opposite direction. The induced Nb moment is 0.09 μ_B in the same direction as the 2a site. This shows that there is a tendency towards moment formation on the 2a sites, in contrast to what might be surmised from the absence of an ordered moment on this site in $TiFe_2$. However, the next lowest energy state studied (Fig. 7.6d) does have zero moments on the 2a sites. In this configuration the 6h layers are stacked antiferromagnetically. The moments on the 2a sites converged to zero in this case, although we did not enforce this by symmetry and started self-consistent iterations with the 2a sites stacked along the c-axis both ferromagnetically and antiferromagnetically with respect to each other (each 2a site is adjacent to an up spin and a down spin 6h layer in these calculations; the stacking we are referring to is the stacking of the 2a sublattice). The energy of this antiferromagnetic state is −0.025 eV with 6h moments of 1.08 μ_B. This is the same ordering as was observed in $TiFe_2$.[161] The corresponding state with the 6h layers stacked ferromagnetically, is the ferromagnetic state discussed above. As mentioned, it is high in energy and metastable against moment collapse to the non-spin-polarized state. This shows that there is a rather strong antiferromagnetic interaction between the stacked 6h layers if they are ferromagnetic in-plane.

We also studied the possibility of frustration in the Kagome type Fe 6h layers due to antiferromagnetic interactions. This was done by calculating configurations with spins flipped in the 6h sheets, as shown in Figs. 7.6e and 7.6f. In both cases considered, the energy is negative relative to the non-spin-polarized case, but well above the energies of the orderings in Figs. 7.6c and 7.6d. This is opposite to what would occur if there were dominant antiferromagnetic interactions between neighbors in the Kagome sheets, and so we conclude that this is not the

case. Interestingly, these solutions with flipped spins in the $6h$ sites also showed significant moments on the $2a$ sites and furthermore depending on the stacking had very different moments on the different sites in the $6h$ layers.

We performed calculations on other orderings as well, but they all either converged to non-spin-polarized case or one of the previous configurations. These calculations show that the moments are strongly dependent on ordering and go to zero for some configurations. Hence, magnetism in this material is of itinerant type with an interplay between magnetic order and moment formation.

All the ordering patterns discussed above, involve different spin arrangements within one unit cell (eight Fe atoms). As such they represent different branches at the Γ point. In order to extend this, we calculated the Lindhard susceptibility, $\chi_0(q,\omega) = \sum_k M_{k,k+q} \frac{f(\epsilon_k)-f(\epsilon_{k+q})}{\epsilon_k-\epsilon_{k+q}-\omega-i\delta}$, neglecting the matrix elements $M_{k,k+q}$, which we set to unity. Fig. 7.7 shows the real part in the zero energy (static susceptibility) limit. We found only weak structure with peaks at the wave-vectors $Q \sim (0.41, 0.97, 0.38), (0.69, 0.13, 0.38), (0.41, 0.97, 0.69)$ and $(0.69, 0.13, 0.69)$. The value of $\chi_0(q) = 1.23 \times 10^{-4}$ emu/mol at the peaks is comparable to $\chi_0(0) = 1.13 \times 10^{-4}$ emu/mol. Therefore the nesting is not strong. Furthermore, we note that our neglect of the matrix element M in the Lindhard functions in general leads to an overestimate at finite q relative to Γ, since the $M = 1$ at Γ and $M \leq 1$ at finite q.

7.3 Discussion and Conclusions

To summarize the main results of our calculations: (1) The magnetism of $NbFe_2$ is highly itinerant. The moments are dependent on ordering and go to zero for some configurations. Furthermore, some magnetic configurations are unstable with respect to the non-spin-polarized system, meaning that stable local moments

do not exist. (2) There are strong magnetic interactions between Fe $2a$ and $6h$ layers. The interlayer $2a$-$2a$ and $6h$-$6h$ interactions are also strong. Ferrimagnetic ordering of Fig. 7.6c has lowest energy with largest moment on Fe($2a$). However, the antiferromangetic ordering of Fig. 7.6d is almost degenerate with the ferrimagnetic state. This implies competing magnetic interactions. (3) There are not strong nearest neighbor antiferromagnetic tendencies in the Kagome layers, and furthermore the electronic structure and magnetic interactions are three dimensional. This implies that geometric frustration based on antiferromagnetic interactions in the 2D Kagome planes is unlikely to be the main player in the quantum criticality. (4) The calculated Lindhard susceptibility shows only weak structure arguing against scenarios involving a simple spin density wave. (5) The magnetic moments in our first principles calculations are much too high compared to experiment. This implies that there is a substantial renormalization presumably due to spin fluctuations. As mentioned, this may be a signature of quantum fluctuations associated with a critical point, as was discussed for $ZrZn_2$ (Ref. [169]) and Ni_3Al.[170] The characteristic of overestimated moments is also shared with the iron superconductors.[143]

It has been argued that large renormalizations generally occur in materials where there is a large phase space for spin-fluctuations.[170, 179, 180, 181, 182] This follows from the fluctuation dissipation theorem, which relates the fluctuation amplitude to the energy and momentum integrated imaginary (dissipative) part of the susceptibility. Thus large amplitude fluctuations and renormalization are expected when the imaginary part of the susceptibility is large over an extended space. The imaginary part of the susceptibility is also what is measured in inelastic magnetic neutron scattering. Therefore, even though the ordered moments are very difficult to measure by neutron diffraction, important insights into the behavior of this material, specifically identification of competing magnetic states that may

exist in relation to the quantum critical behavior may be obtained from inelastic scattering. If the LSDA moments represent mean field values that are then reduced by fluctuations, the amplitude of these fluctuations must be sizable, and therefore they should be visible in experiments. It would be of considerable interest to perform such measurements. Finally, we mention one important difference between the iron superconductors and $NbFe_2$. In $NbFe_2$ ferrimagnetism, which from a symmetry point of view is ferromagnetism, is nearby both based on LSDA results and experimental data as a function of alloying. Crucially, ferromagnetic spin fluctuations are strongly pair breaking for singlet superconductivity.

Chapter 8

Electron-phonon superconductivity in LaNiPO and $BaNi_2As_2$

This chapter is based on *"Electron-phonon superconductivity in LaNiPO"*, Alaska Subedi, David J. Singh and Mao-Hua Du, Phys. Rev. B **78**, 060506(R) (2008), *"Density functional study of $BaNi_2As_2$: Electronic structure, phonons, and electron-phonon superconductivity"*, Alaska Subedi and David J. Singh, Phys. Rev. B **78**, 132511 (2008), and *"Low-Temperature Magnetothermal Transport Investigation of a Ni-Based Superconductor $BaNi_2As_2$: Evidence for Fully Gapped Superconductor"*, Phys. Rev. Lett. **102**, 147004 (2009).

8.1 Introduction

The finding of superconductivity in F doped LaFeAsO by Kamihara and co-workers[10] has led to considerable interest as this provides an alternative non-cuprate route to high critical temperature (T_c) superconductivity. Since this finding, high T_c superconductivity has been found in many related phases that can be generally characterized into four different groups according to their parent

compounds: (i) LaFeAsO,[10, 183, 184] (ii) $BaFe_2As_2$,[11, 123] (iii) LiFeAs,[185] and (iv) α-FeSe.[12] The precise mechanism of superconductivity in these compounds is yet to be established, but is strongly thought to be unconventional. This is based in part on calculations of the electron-phonon coupling,[133, 129] which is too small to account for any appreciable superconductivity and on the proximity to magnetism.[126, 125, 186, 187, 135] These compounds show considerable variation in doping levels (i.e. hole or electron doped), applied pressure, and chemistry of the non-Fe layers, while remaining superconducting. However, there are three main threads joining these compounds together. The parent compounds have spin density wave (SDW) order with the possible exception of the LiFeAs phase, exist in a tetragonal structure and possess iron in a 2D square lattice sheet. There is a clear association between suppression of the SDW order and appearance of superconductivity in the phase diagrams, although recent work does show some range of coexistence of magnetism and superconductivity.[188, 189] Importantly, the SDW phase is accompanied by an orthorhombic distortion. Depending on the specific material, this distortion occurs at a temperature higher than the SDW ordering temperature or coincident with it.[126, 11, 190]

In this regard, besides the FeAs based phases, superconductivity is also observed in Ni based materials, including LaNiPO,[15, 191] pure, fluorine or Sr doped LaNiAsO,[192, 193, 183] and LaNiBiO.[194] In addition, Ronning *et al.* recently reported both the occurrence of a first order phase transition at $T_0 = 130$ K with characteristics similar to the structural transition seen in the Fe-As based superconductors, and a superconducting transition with $T_c = 0.7$ K in $BaNi_2As_2$.[195] It is possible that the underlying physics in both the Fe and Ni superconductors are similar. Since Fe and Ni are ambient temperature ferromagnets and many Fe and Ni compounds show magnetism, it is plausible to expect that Ni can fill in the role of Fe in these compounds.

In this chapter, we report the details of our calculations of the electronic structure, phonons, and electron-phonon coupling of LaNiPO and $BaNi_2As_2$. The band structure of these compounds are similar to that reported for their As counterparts,[196, 197, 198, 199] but the Fermi level is shifted up owing to the higher valence electron count in Ni^{2+} and Fe^{2+}. Hence, with a larger Fermi surface and higher carrier density, the Ni compounds have remarkably different electronic properties from their Fe counterparts. The electron-phonon properties are also different. Unlike the Fe based materials, superconductivity in Ni based compounds can be readily explained by the standard electron-phonon mechanism.

8.2 Methods and Structure

The electronic structure calculations for both LaNiPO and $BaNi_2As_2$ were performed within the local density approximation (LDA) with the general potential linearized augmented planewave (LAPW) method.[19] We used LAPW spheres of radius 2.2 a_0 for La, 2.2 a_0 for Ba, 2.1 a_0 for Ni, 2.1 a_0 for P, 2.1 a_0 for As and 1.6 a_0 for O.

LaNiPO occurs in a tetragonal structure ($P4/nmm$) with La, Ni, P and O at the positions 2c(0.25, 0.25, z_{La}), 2b(0.75, 0.25, 0.5), 2c(0.25, 0.25, z_{P}) and 2a(0.75, 0.25, 0), respectively, where z_{La} and z_{P} are internal coordinates that correspond to the La and P heights. We used experimentally reported lattice parameters (a=4.0461Å, c=8.100Å)[15] and relaxed the internal coordinates. We obtain z_{La}=0.1506 and z_{P}=0.6210, which are close to the reported experimental values of z_{La}=0.1531 and z_{P}=0.6260,[15] and z_{La}=0.1519 and z_{P}=0.6257.[191] This is different from the Fe-based compounds where pnictogen heights significantly lower than the reported experimental values are generally obtained.[142, 143]

$BaNi_2As_2$ occurs in a body centered tetragonal structure ($I4/mmm$) with Ba, Ni and As at the positions 2a(0,0,0), 4d(0.5,0,0.5) and 4e(0,0,z_{As}), respectively. Here z_{As}, the As height above the Ni square planes, is a structural parameter governing the Ni-As distance and the distortion of the As tetrahedra that coordinate the Ni in this material. Again, we used experimental lattice parameters ($a = 4.112$ Å and $c = 11.54$ Å)[195] but employed the computed z_{As} obtained via non-spin polarized energy minimization. The value we obtain for $z_{As} = 0.346$ agree well with the experimental value of $z_{As} = 0.3476$. This is in contrast to $BaFe_2As_2$,[199] and other Fe based superconductors where LDA calculations done in this way noticeably underestimate z_{As}, but is similar to the case of LaNiPO. It has been suggested that this underestimation of z_{As} in Fe based superconductors is due to its coupling with magnetism.[187, 142, 143] This underestimation may be indicative of strong spin fluctuations in the paramagnetic superconducting parts of the phase diagrams of the Fe-based materials. The absence of this discrepancy between the experimental and calculated value of z_{La} and z_P in LaNiPO and z_{As} in $BaNi_2As_2$ then indicates that the magnetic character of LaNiPO and $BaNi_2As_2$ is different from that of Fe based superconductors.

The phonon dispersions and electron-phonon coupling were calculated using linear response as implemented in Quantum Espresso code,[31] similar to the calculations reported for LaFeAsO.[133, 129] The linear response calculations were also done with experimental lattice parameters, using ultrasoft pseudopotentials within the generalized gradient approximation (GGA) of Perdew, Burke and Ernzerhof.[29] An 8x8x8 grid was used for the zone integration in the phonon calculations, while a more dense 32x32x8 grid was used for the zone integration in the electron-phonon coupling calculations. The basis set cut-off for the wave functions was 40 Ry, while a 400 Ry cut-off was used for the charge density.

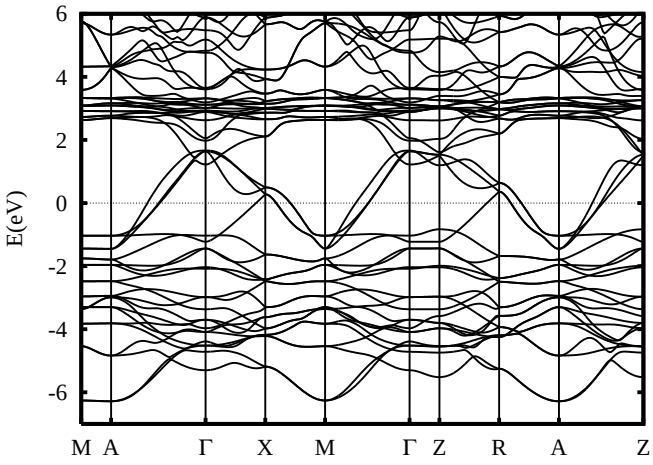

Figure 8.1: Calculated LDA band structure of LaNiPO using the experimental lattice parameter and relaxed internal coordinates, z_{La}=0.1506 and z_{P}=0.6210. The band structure is plotted along the path $(\frac{1}{2},\frac{1}{2},0) \rightarrow (\frac{1}{2},\frac{1}{2},\frac{1}{2}) \rightarrow (0,0,0) \rightarrow (0,\frac{1}{2},0) \rightarrow (\frac{1}{2},\frac{1}{2},0) \rightarrow (0,0,0) \rightarrow (0,0,\frac{1}{2}) \rightarrow (0,\frac{1}{2},\frac{1}{2}) \rightarrow (\frac{1}{2},\frac{1}{2},\frac{1}{2}) \rightarrow (0,0,\frac{1}{2})$.

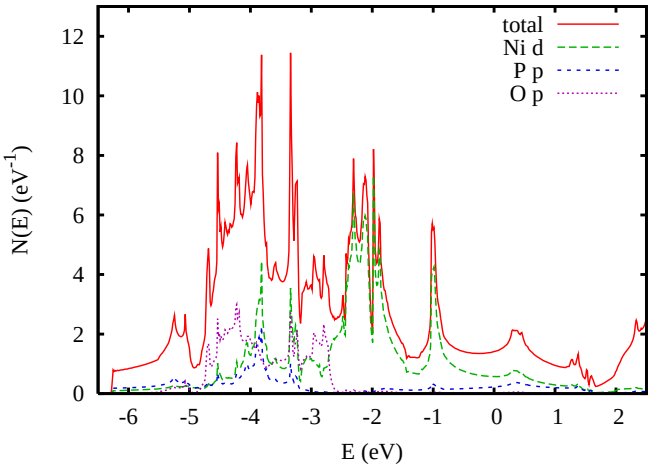

Figure 8.2: (color online) Calculated LDA density of states of LaNiPO on a per formula unit both spins basis. The projections are onto the LAPW spheres.

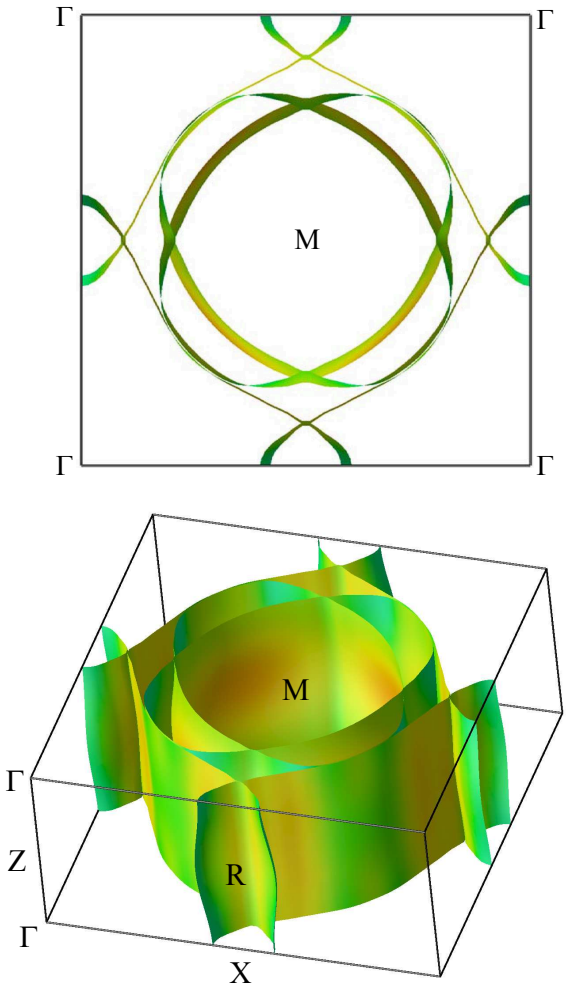

Figure 8.3: (color online) Calculated LDA Fermi surface of LaNiPO shaded by velocity. The top panel shows a view along the tetragonal axis while the bottom panel shows a tilted view.

8.3 Results for LaNiPO

The calculated band structure and electronic density of states (DOS) are shown in Figs. 8.1 and 8.2, respectively. The Fermi surface of LaNiPO is given in Fig. 8.3. As may be seen, these are very different in LaNiPO from those in LaFeAsO. This is as might be expected from the different electron count. LaNiPO and LaFeAsO have a similar structure to the d bands, and in particular LaNiPO should be described as Ni^{2+} ions on a square lattice with direct hopping as well as a P induced crystal field. In fact, the projections of the density of states shows that there is a greater degree of covalency between Ni and P, than between Fe and As or Fe and P in the corresponding Fe-based materials. There remains a pseudogap at a d electron count of 6, however Ni^{2+} has 8 electrons. This places E_F well inside the upper manifold of d states. In this energy range the bands are derived from Ni d states hybridized with P p states. The bands at E_F are more dispersive than in the Fe compounds where E_F is lower. This leads to lower density of states with higher in plane Fermi velocity, $N(E_F)$=1.41 eV^{-1} per formula unit, v_{xx}=3.75x10^7 cm/s, v_{zz}=0.39x10^7 cm/s. The lower $N(E_F)$ puts the Ni based compound further from magnetism than the Fe-based materials, as discussed in Ref. [125]. Furthermore, this compound is quite two dimensional in the sense that there is no 3D Fermi surface sheet. Based on the anisotropy of the Fermi velocity, the ratio of in-plane to c-axis conductivity for the Ni compound is ~ 100 assuming isotropic scattering. The Fermi surface may described as consisting of two large ellipsoidal cross-section electron cylinders around M, and a large hole section around Γ. This hole section intersects the zone boundary near X leading to an electron section around X.

The calculated phonon dispersions of LaNiPO are shown in Fig. 8.4. The corresponding phonon density of states and Eliashberg spectral function $\alpha^2F(\omega)$ are shown in Fig. 8.5. The phonon dispersions show a set of 12 phonon bands

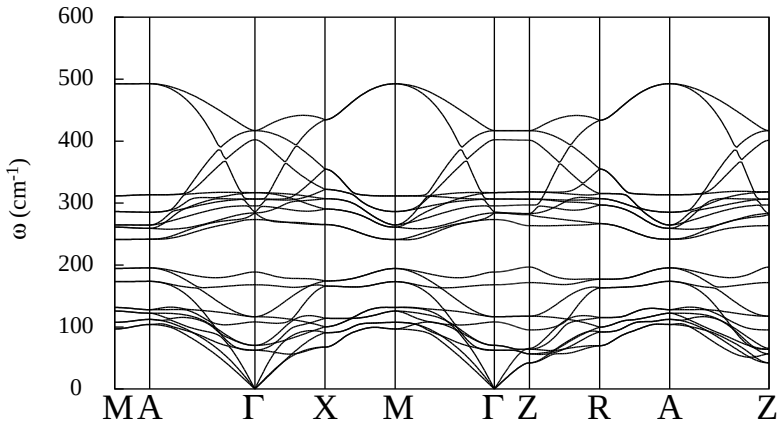

Figure 8.4: Calculated phonon dispersions of LaNiPO as obtained within linear response along the path $(\frac{1}{2},\frac{1}{2},0) \rightarrow (\frac{1}{2},\frac{1}{2},\frac{1}{2}) \rightarrow (0,0,0) \rightarrow (0,\frac{1}{2},0) \rightarrow (\frac{1}{2},\frac{1}{2},0) \rightarrow (0,0,0) \rightarrow (0,0,\frac{1}{2}) \rightarrow (0,\frac{1}{2},\frac{1}{2}) \rightarrow (\frac{1}{2},\frac{1}{2},\frac{1}{2}) \rightarrow (0,0,\frac{1}{2})$..

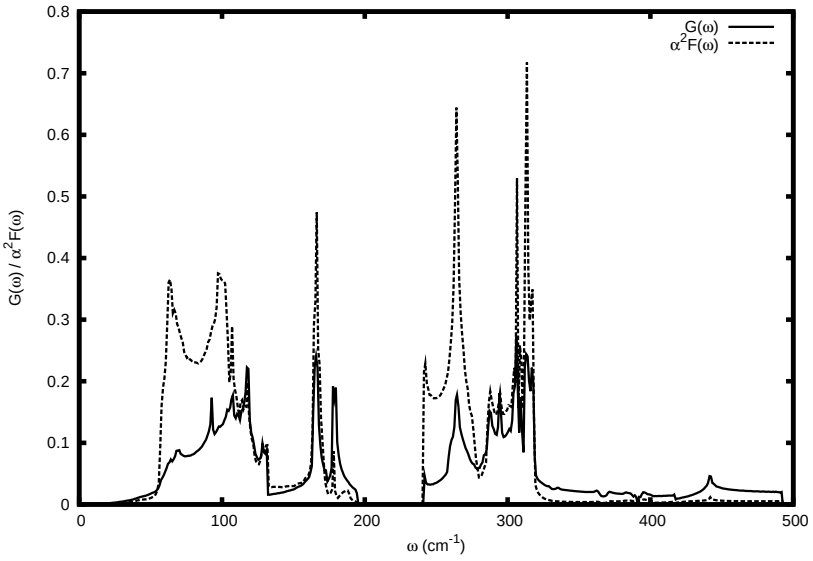

Figure 8.5: Calculated phonon density of states and electron phonon spectral functional $\alpha^2F(\omega)$.

extending up to $\sim$ 200 cm^{-1}, separated by a gap from 12 higher frequency bands extending up to $\sim$ 500 cm^{-1} (note that there are 24 phonon branches since there are two formula units per primitive cell). The higher frequency manifold is derived mainly from O and P motions. Within this upper manifold the P contribution is mainly below $\sim$ 300 cm^{-1}, while the dispersive modes above 300 cm^{-1} are mainly O derived. The lower manifold from 0 to 200 cm^{-1} consists of the acoustic modes and modes of mixed, but mainly metal character.

We obtain a value of the electron phonon coupling λ=0.58 with logarithmically averaged frequency $\omega_{\ln}$=113 cm^{-1}. Relative to the phonon density of states, the spectral function is enhanced for the lower frequency metal modes, which have strong in-plane Ni character, and for the modes at the bottom of the upper manifold, which have strong P character. Thus in spite of the lower electronic density of states, we obtain stronger electron phonon coupling as compared with LaFeAsO, where $\lambda \sim 0.2$.[133, 129] Inserting these numbers into the simplified Allen-Dynes formula,

$$k_B T_c = \frac{\hbar\omega_{\ln}}{1.2} \exp\left\{-\frac{1.04(1+\lambda)}{\lambda - \mu^*(1+0.62\lambda)}\right\}, \tag{8.1}$$

with ordinary values of the Coulomb parameter μ^* yields values in reasonable accord with experiment. Specifically, for μ^*=0.12 we obtain T_c=2.6K, which is in accord with the experimental value $T_c \sim$ 3K,[15] or T_c=4.2K.[191]

8.4 Results for $BaNi_2As_2$

The calculated band structure and electronic density of states (DOS) are shown in Figs. 8.6 and 8.7, respectively. The Fermi surface is shown in Fig. 8.8. The pnictogen p states occur between -6 eV and -3 eV, with respect to the Fermi energy, consistent with an anionic As^{3-} species, and modest hybridization of the

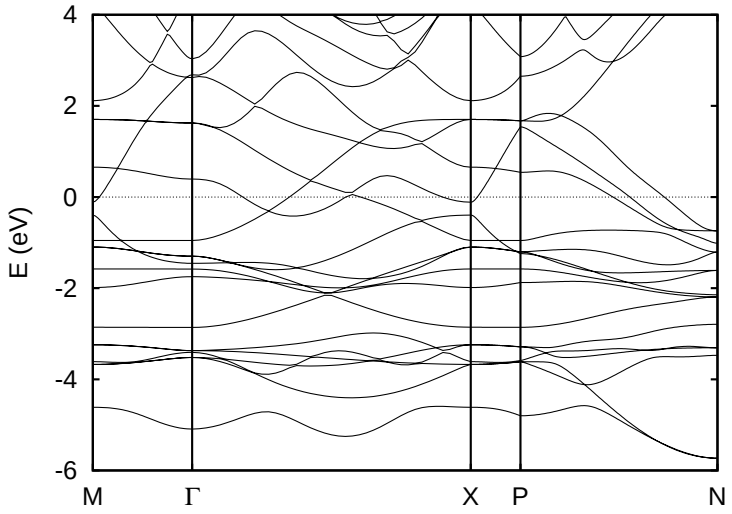

Figure 8.6: Calculated LDA band structure of non-spin-polarized $BaNi_2As_2$ along the path $(0,0,\frac{1}{2}) \rightarrow (0,0,0) \rightarrow (0,\frac{1}{2},0) \rightarrow (0,\frac{1}{2},\frac{1}{4}) \rightarrow (\frac{1}{4},\frac{1}{4},\frac{1}{4})$.

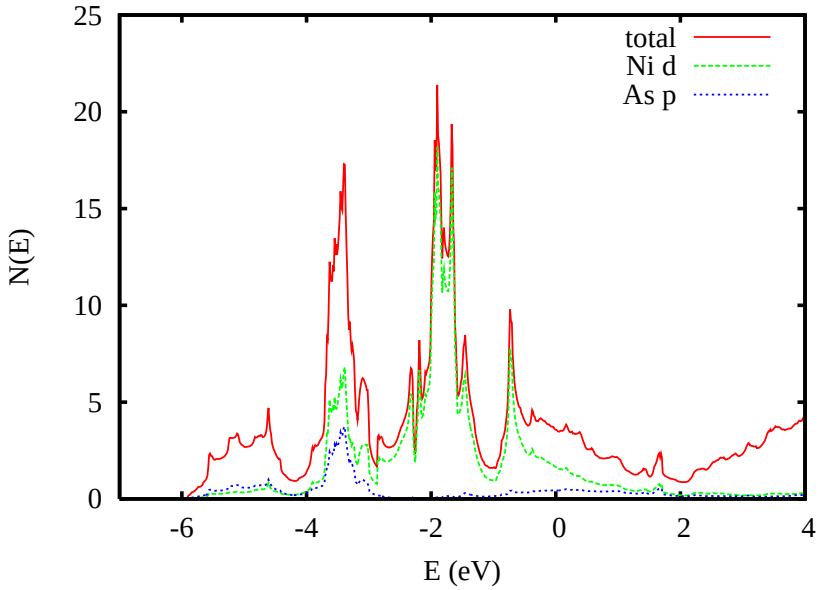

Figure 8.7: (color online) Calculated LDA electron density of states of non-spin-polarized $BaNi_2As_2$ and projections onto the LAPW spheres on a per formula unit basis.

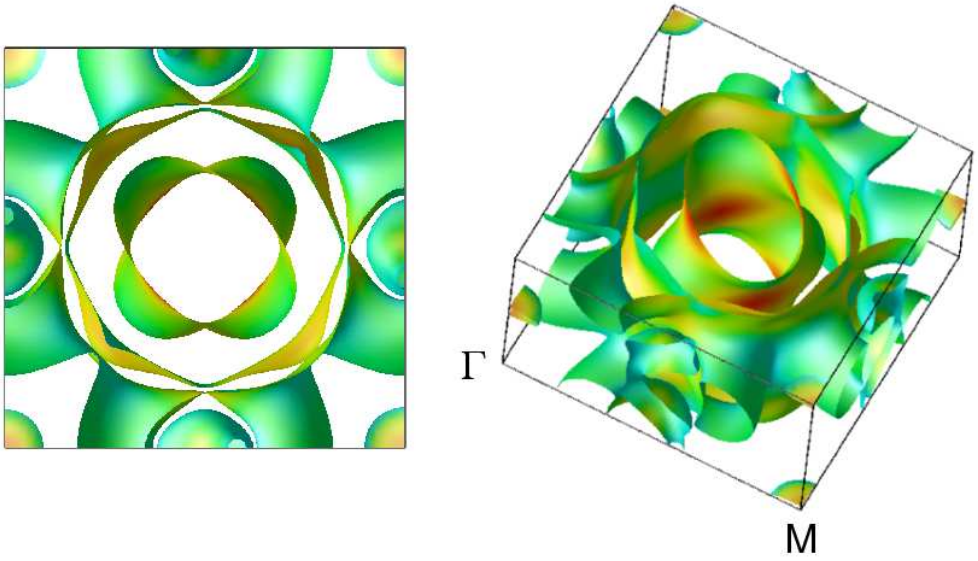

Figure 8.8: (color online) Calculated LDA Fermi surface of non-spin-polarized $BaNi_2As_2$. The shading is by velocity.

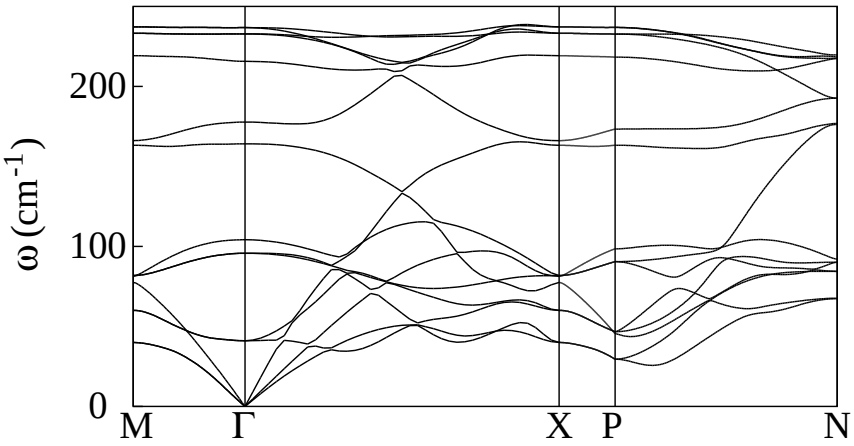

Figure 8.9: Calculated GGA phonon dispersion curves of non-spin-polarized $BaNi_2As_2$ along the path $(0,0,\frac{1}{2}) \rightarrow (0,0,0) \rightarrow (0,\frac{1}{2},0) \rightarrow (0,\frac{1}{2},\frac{1}{4}) \rightarrow (\frac{1}{4},\frac{1}{4},\frac{1}{4})$.

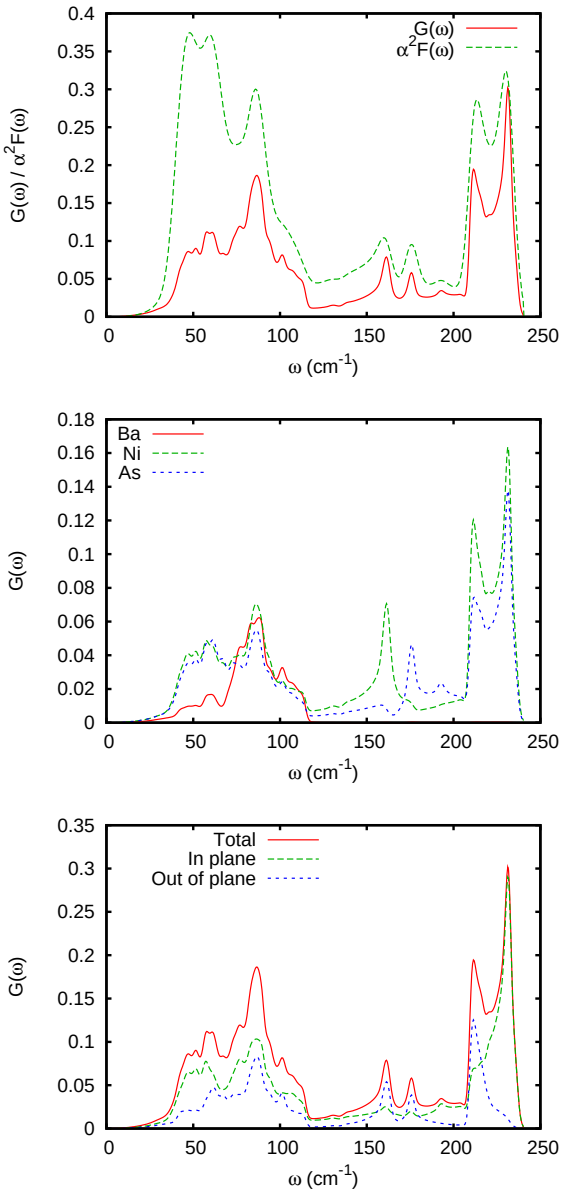

Figure 8.10: (color online) Top: Calculated GGA phonon density of states $G(\omega)$ and electron-phonon spectral function $\alpha^2F(\omega)$ for non-spin-polarized $BaNi_2As_2$. Middle: Projected phonon density of states for each atom of $BaNi_2As_2$. Bottom: Phonon density of states weighted by in-plane or out-of-plane character, i.e. atomwise projections of eigenvectors in the ab-plane and along the c-axis, respectively.

As p states with Ni d states similar to the Fe-based materials. As expected, Ba occurs as Ba^{2+} with the Ba derived valence states well above the Fermi energy. As such, Ni has a nominal valence Ni^{+2} with eight d electrons per Ni. The manifold of six heavy bands between -3.0 eV and -1.0 eV have Ni d character and account for six electrons per Ni. There is a pseudogap at this point separating the heavy bands from a manifold of lighter bands that span between -1.0 eV and 2.0 eV. The light bands accommodate the remaining d electrons and show Ni d character accompanied by some mixing with As p states. It may seen that the band structure and DOS of $BaNi_2As_2$ are qualitatively very similar to that of $BaFe_2As_2$ (Refs. [197],[198], and [199]), with the exception that Ni^{2+} crucially contains two more valence electrons than Fe^{2+}. This causes the Fermi level to shift up away from the pseudogap into the upper manifold. As a result, compared to $BaFe_2As_2$, $BaNi_2As_2$ has a large multi-sheet Fermi surface very different from the Fe-based materials. The value of the DOS at E_F is $N(E_F)$=3.57 eV^{-1}, on a per formula unit (two Ni atoms) both spins basis. This is lower than LaFeAsO, but is comparable to some of the other Fe-As based materials.

The calculated phonon dispersions of $BaNi_2As_2$ are shown in Fig. 8.9. The corresponding phonon density of states and Eliashberg spectral function $\alpha^2F(\omega)$ are shown in Fig. 8.10. There are 15 phonon bands extending up to $\sim$ 230 cm^{-1}. The bands below 120 cm^{-1} show Ba, Ni and As characters while the region above it contains bands of mostly Ni and As character. From Fig. 8.10, we can see that the electron-phonon spectral function is enhanced relative to the phonon density of states in the low frequency modes. The projected phonon density of states plots (Fig. 8.10, middle and bottom) show that this enhancement occurs in the region where there is high Ni and As character, although the enhancement cannot be attributed to solely in-plane or out-of-plane character. This is in contrast to the case of LaFeAsO where the spectral function more closely follows in proportionality

to the phonon density of states in this energy region.[133] It should be noted that doped LaFeAsO was shown to have a rather low overall electron-phonon coupling ($\lambda \sim 0.2$) which cannot explain the superconductivity[133] while LaNiPO was shown to be be readily explained as conventional electron-phonon superconductor.[200] For $BaNi_2As_2$, we obtain a value of the electron-phonon coupling $\lambda = 0.76$ with logarithmically average frequency $\omega_{\ln} = 73$ cm^{-1}. Inserting these numbers into the simplified Allen-Dynes formula (Eq. 8.1), with $\mu^* = 0.12$, we obtain $T_c \sim 4$K, which overestimates but is reasonably in accord with the experimental low value of $T_c = 0.7$K.[195] As mentioned, the total DOS per formula unit at the Fermi energy is $N(E_F) = 3.57$ eV^{-1}. With a typical $3d$ Stoner parameter $I \sim 0.7$ – 0.8 eV, this yields a Stoner enhancement $(1 - NI)^{-1} \sim 3$ (note that in this formula N is per atom per spin). This enhancement is sufficient to indicate the presence of spin fluctuations that would depress the electron-phonon T_c and may therefore explain why the experimental T_c is reduced compared with the calculated value based on λ.

8.5 Conclusions

In summary, we have presented electronic structure calculations that show LaNiPO and $BaNi_2As_2$ have very different electronic properties compared to the Fe based high T_c superconductors. Even though their band structures are similar to that of Fe based superconductors, the Fermi level lies in the upper manifold away from the pseudogap due to higher number of valence electrons in Ni^{2+}. This gives Ni compounds large Fermi surfaces in contrast to the small surfaces in the Fe based superconductors. Also in contrast to the Fe based superconductors, the Ni based compounds have intermediate electron-phonon coupling which is sufficient to describe these compounds as conventional electron-phonon superconductors.

Chapter 9

Electron-phonon superconductivity in noncentrosymmetric $LaNiC_2$

A similar version of this chapter appeared as *"Electron-phonon superconductivity in noncentrosymmetric $LaNiC_2$: First-principles calculations"*, Alaska Subedi and David J. Singh, Phys. Rev. B **80**, 092506 (2010).

9.1 Introduction

$LaNiC_2$ is a member of a family of ternary nickel carbides RNiC$_2$ (where R is a rare earth or Y) first reported by Bodak and Marusin.[16] These compounds form in the base centered orthorhombic CeNiC$_2$-type structure (space group $Amm2$) that lacks inversion symmetry. Studies of magnetic properties show that the RNiC$_2$ phases exhibit a variety of magnetic ordering for various R.[201, 202] Although, Ni is often associated with magnetism, e.g. in oxides and in intermetallics, the magnetism in these compounds is due to $4f$ electrons of R with almost no magnetic contribution from Ni. Therefore, it is perhaps not surprising that $LaNiC_2$ does not

show magnetic ordering. Interestingly, it is instead superconducting at $T_c = 2.7$ K.[17, 18]

Lee *et al.*[17] found non-exponential decay of specific heat below T_c and based on this argued that $LaNiC_2$ is an unconventional superconductor. Since pure Ni is a ferromagnet and Ni compounds are often magnetic, one might suppose $LaNiC_2$ to be near magnetism and therefore that a pairing mechanism involving spin fluctuations is operative. Spin fluctuations are not pairing for order parameters that do not change sign on the Fermi surface (i.e. conventional s-wave). However, Pecharsky *et al.*[18] observed the usual exponential decay of specific heat below T_c, consistent with the conventional BCS superconductivity. One avenue to address the inconsistency of these two experiments is by determining the symmetry that is broken in the superconducting system. Gauge symmetry is broken in a conventional BCS superconductor,[203] while other symmetries are broken in unconventional ones.[204] Related to this, Hillier *et al.* recently reported their results of muon spin relaxation measurements on $LaNiC_2$ that indicate that time reversal symmetry is broken in the superconducting state.[205] Such time reversal symmetry breaking requires a superconducting state with triplet character, and does not occur in singlet superconductors. However, this analysis is complicated by the non-centrosymmetric lattice structure of $LaNiC_2$.

There are a number of other examples of non-centrosymmetric superconductors including for example $CePtSi_3$, $CeIrSi_3$, $CeRh_3Si$, UIr, Li_2Pd_xB, Re_3W and Y_2C_3.[206, 207, 208, 209, 210, 211, 212] These include both non-phonon mediated heavy Fermion metals and electron phonon superconductors, which behave very much like conventional centrosymmetric superconductors. Since parity is not a good quantum number in non-centrosymmetric systems, it necessitates the modification of scheme for classification of Cooper pairs. For example, Yanase and Sigrist[213] argue that Cooper pairs have a state that has dominant p-wave

with some mixture of s-wave symmetry in $CePt_3Si$. Considering the T_c of $LaNiC_2$, either case is possible; it could be a conventional electron-phonon superconductor in analogy with Y_2C_3 (refs. [212, 214]) and Re_3W (ref. [215]), in which case it would have a Cooper pair state that has dominant s-wave but some mixture of p-wave symmetry or alternatively it could be an unconventional superconductor in analogy with the non-centrosymmetric heavy Fermions such as $CePt_3Si$ (refs. [206, 216]), or near ferromagnetic UIr, in which case it would have dominant p or d wave character, which would allow a simpler explanation of non-exponential behavior.

Here, we report the results of first principles calculations of electronic structure, phonon dispersion and electron-phonon coupling. We find that the main contributions to the electronic structure from Ni $3d$ orbitals are away from the Fermi energy and consequently that $LaNiC_2$ is non-magnetic and rather far from magnetic instabilities that might lead to strong spin fluctuations thereby leading to an unconventional superconducting state. On the other hand, we obtain a value of electron-phonon coupling constant $\lambda \sim 0.52$ with logarithmically averaged frequency $\omega_{\ln} \sim 207$ cm^{-1}. Using simplified Allen-Dynes formula, we obtain $T_c \sim 3.0$ K that suggests $LaNiC_2$ is an intermediately coupled electron-phonon superconductor with dominant pairing that has s-wave but also some mixture of p-wave symmetry.

9.2 Structure and Method

$LaNiC_2$ forms in a base centered orthorhombic structure with La on site $(0.5, u, 1-u)$, Ni on site $(0, 0, 0)$ and C on site $(0, v, w)$. In this compound, the La atoms form trigonal prisms, which are alternately filled by Ni and C dimers, hence breaking the inversion symmetry. Another characteristic of this structure is the short bond length of C dimers, which indicates the existence of very stiff bond stretching

modes. If these modes were responsible for superconductivity, it would result in a moderately high electron-phonon coupling and a large logarithmically averaged phonon frequency. This would mean a very high prefactor in the McMillan equation for T_c. Previous tight-binding[217] and density functional[214, 218] studies of other metals with C dimers show that the electronic structure near the Fermi level could have substantial contributions from states with C-C antibonding character. If this were the case for $LaNiC_2$, there may be a strong dependence of T_c on the occupation of the antibonding states (which could be controlled by doping) and perhaps also a high T_c in optimally doped samples.

Our electronic structure calculations were performed within the local density approximation (LDA) using the general potential linearized augmented planewave (LAPW) method as implemented in our in-house code.[19] We used LAPW spheres of radius $2.0a_0$ for La and Ni and $1.25a_0$ for C. We repeated some calculations with the WIEN2k code[30] as a test and found no significant differences. We used the experimentally reported lattice parameters ($a = 3.959$ Å, $b = 4.564$ Å, $c = 6.204$ Å),[16] but relaxed the internal coordinates. We obtain for internal parameters, $u = 0.3886$, $v = 0.5411$, and $w = 0.1606$. This yields the calculated C-C distance of 1.36 Å, which is in reasonable accord with the reported experimental value[16] of 1.41 Å.

The phonon dispersions and electron-phonon coupling were calculated using linear response as implemented in Quantum Espresso code.[31] The linear response calculations were also done using experimental lattice parameters, using ultrasoft pseudopotentials within the generalized gradient approximation (GGA) of Perdew *et al.*[29] An $8 \times 8 \times 8$ grid was used for the zone integration in the phonon calculations, while a more dense $32 \times 32 \times 32$ grid was used for the zone integration in the electron-phonon coupling calculations. The basis set cutoff for the wave functions was 40 Ry, while a 400 Ry cutoff was used for the charge density. The

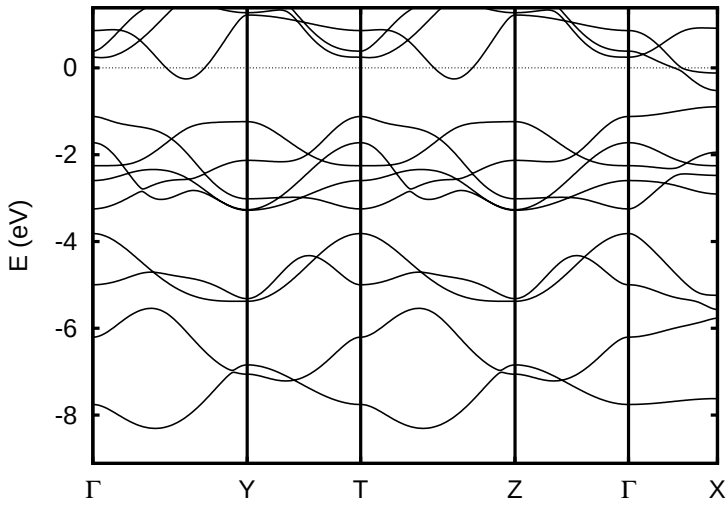

Figure 9.1: Calculated LDA band structure of $LaNiC_2$ plotted along the path (0,0,0) → (0,$\frac{1}{2}$,0) → (0,$\frac{1}{2}$,$\frac{1}{2}$) → (0,0,$\frac{1}{2}$) → (0,0,0) → ($\frac{1}{2}$,0,0).

internal coordinates were again relaxed and we obtained values that agreed well with the values obtained from LDA calculations. The GGA and LDA electronic structures were very similar.

9.3 Results

The calculated band structure and Fermi surface of $LaNiC_2$ is shown in Figs. 9.1 and 9.2, respectively. These agree in large scale features with recent calculations done by Laverock *et al.*,[219] but the details of the Fermi surface and band dispersions differ significantly along some directions, yielding differences in the Fermi surface. These presumably reflect the use of non-full potential methods in Ref. [219]. The corresponding density of states is shown in Fig. 9.3. The band structure shows a C 2*s* derived band between -15.5 and -13.5 eV and another C 2*s* derived band between -8.5 and -6.5 eV, relative to the Fermi energy E_F. This is followed by a manifold of three bands with C 2*p* character, associated with C

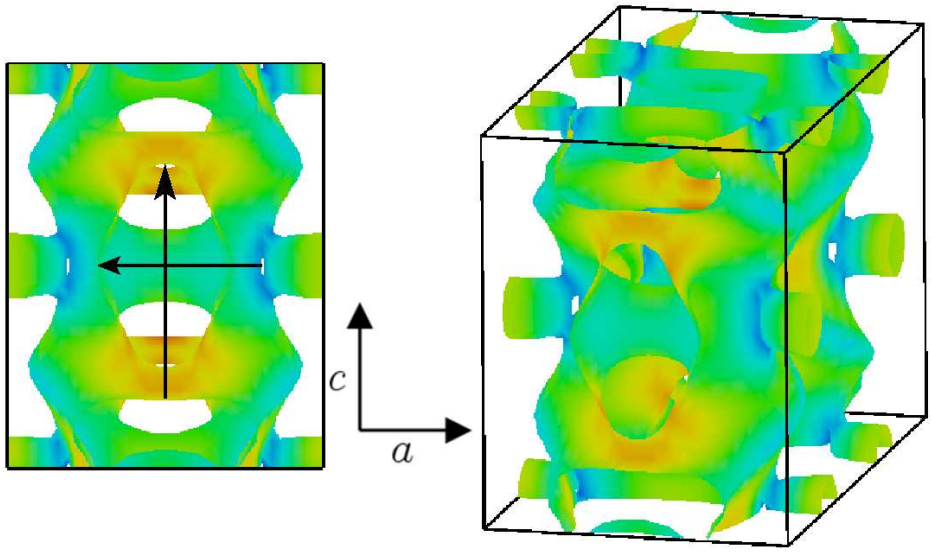

Figure 9.2: (Color online) Calculated LDA Fermi surface of $LaNiC_2$. The shading is by velocity. The arrows indicate nesting vectors that give rise to Kohn anomalies.

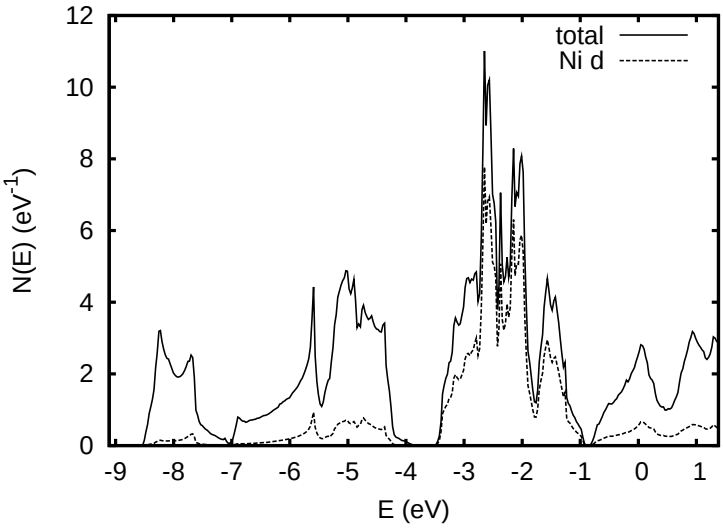

Figure 9.3: Calculated LDA density of states of $LaNiC_2$ on a per formula unit both spins basis. The projection is onto the Ni LAPW sphere.

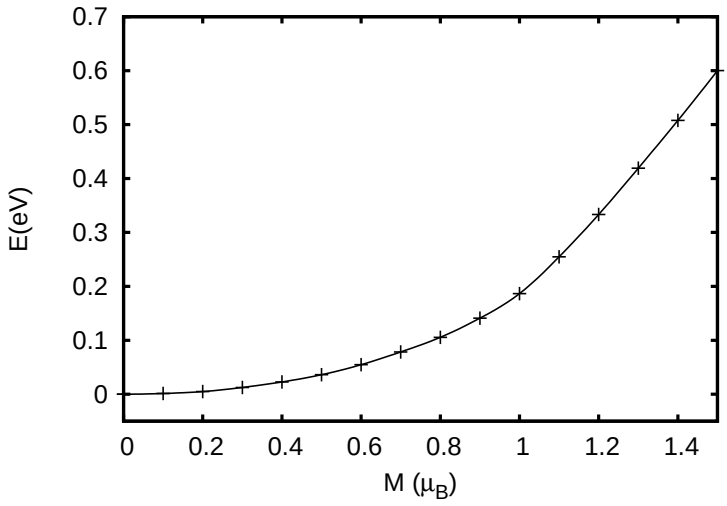

Figure 9.4: Fixed spin moment magnetic energies for $LaNiC_2$.

dimers, that extend from -7.5 to -3.8 eV. This is followed by a manifold of 5 bands of Ni 3d character between -3.5 and -0.9 eV. These account for the majority of the Ni d character in the density of states although there is some Ni d contribution near E_F, similar to the borocarbides (e.g. $LuNi_2B_2C$), which electron phonon superconductors.[220] There are two bands that cross the Fermi level and they have mixed Ni 3d, La 5d and C 2p antibonding characters. This electronic structure is consistent with strongly bonded C dimers embedded in a metallic solid with states near E_F having La, Ni and C antibonding character.

The density of states at E_F is $N(E_F) = 2.6$ eV^{-1} on a per formula unit both spin basis. The calculated Fermi velocities are $< v_{xx}^2 >^{1/2}$=1.79x10^5 m/s, $< v_{yy}^2 >^{1/2}$=1.52x10^5 m/s, and $< v_{zz}^2 >^{1/2}$=1.48x10^5 m/s, indicating only modest resistivity anisotropy unless there is a large scattering anisotropy. The density of states has a prominent peak with a maximum very close to E_F. Therefore the stoichiometric compound is expected to have the highest T_c similar to Y_2C_3, although in the present case the peak is broader. Doping away from stoichiometry will move the E_F away from the peak and is therefore expected to lower the T_c.

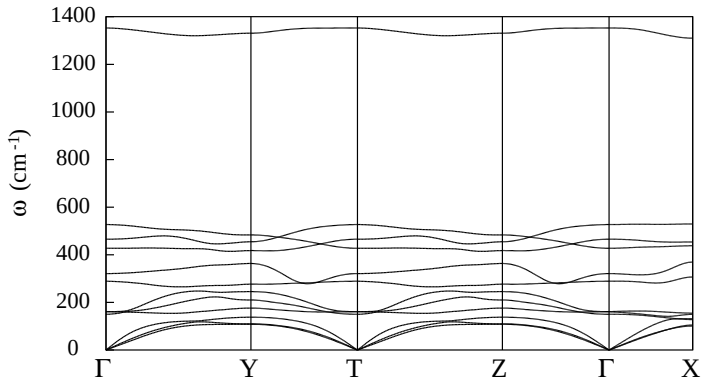

Figure 9.5: Calculated phonon dispersion curves of $LaNiC_2$ plotted along the path (0,0,0) → (0,$\frac{1}{2}$,0) → (0,$\frac{1}{2}$,$\frac{1}{2}$) → (0,0,$\frac{1}{2}$) → (0,0,0) → ($\frac{1}{2}$,0,0).

The moderately high value of $N(E_F)$ might also indicate magnetism if the states at the Fermi level are of predominantly Ni d character. However, as mentioned, most of the Ni d states are in a manifold of 5 bands that lie between -3.5 and -0.9 eV relative to the Fermi level. Hence, the high $N(E_F)$ of $LaNiC_2$ does not place it near magnetism. This is supported by our fixed spin moment calculations. Fig. 9.4 shows energies calculated for different values of magnetic moment relative to the nonmagnetic case. As may be seen the energy scale is relatively high, which means that the material is not near ferromagnetism.

The calculated phonon dispersions of $LaNiC_2$ are shown in Fig. 9.5. The corresponding phonon density of states and Eliashberg spectral function $\alpha^2F(\omega)$ are shown in Fig. 9.6. The phonon dispersions show a set of 11 bands extending up to $\sim$ 530 cm^{-1}, separated by a gap of $\sim$ 775 cm^{-1} from 1 high frequency band that lies between 1305 and 1355 cm^{-1}. The bands below 180 cm^{-1} show contributions from La, Ni and C, while the bands between 180 and 255 cm^{-1} are derived mainly from motions of Ni and C atoms. Above 255 cm^{-1} the bands are dominated by motions of C atoms. The highest frequency band is an almost pure C-C bond

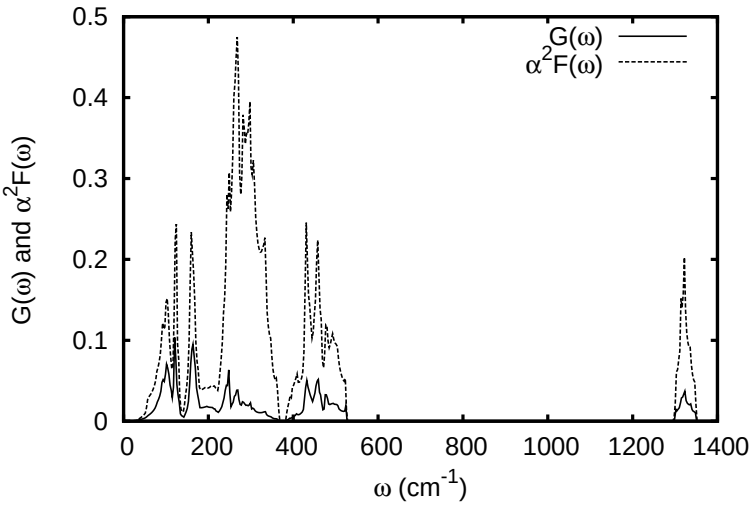

Figure 9.6: Calculated phonon density of states and electron-phonon spectral function $\alpha^2F(\omega)$ for $LaNiC_2$.

stretching mode, confirming the picture of strongly bonded C dimer inferred from band structure.

The eighth branch of the phonon dispersion, which has mainly C non-bond-stretching character, shows Kohn anomalies at $k \sim (0, 0.5, 0.25)$, $k \sim (0, 0, 0.25)$ and $k \sim (0.25, 0, 0)$. These can be seen in Fig. 9.5 along the Y–T, Z–Γ and Γ–X lines. The origin of the Kohn anomalies can be seen in the Fermi surface, which shows nesting with wavevectors $k \sim (0, 0, 0.25)$ and $k \sim (0.25, 0, 0)$ as indicated by two arrows in Fig. 9.2. A comparison of phonon density of states with the with the Eliashberg spectral function shows that the latter is enhanced relative to the former between 220 and 400 cm^{-1}, which is the region where the seventh (which also has mainly C non-bond-stretching character) and eighth branches are placed. We obtain a value of the electron-phonon coupling $\lambda = 0.52$. As there are 12 phonon branches, the average electron-phonon coupling per branch is $\lambda_{avg} = 0.04$. The contribution due to seventh and eighth bands is large with values of $\lambda_7 = 0.13$ and $\lambda_8 = 0.09$, respectively. We obtain for the logarithmically averaged frequency

$\omega_{\ln} = 207$ cm^{-1}. Inserting these numbers into the simplified Allen-Dynes formula,

$$k_B T_c = \frac{\hbar \omega_{\ln}}{1.2} \exp\left\{ -\frac{1.04(1+\lambda)}{\lambda - \mu^*(1+0.62\lambda)} \right\}, \tag{9.1}$$

with $\mu^* = 0.12$, we obtain $T_c \sim 3$ K, which is in accord with the experimental value of $T_c = 2.7$ K.[17, 18] While this close agreement may be partly fortuitous (note the parameter μ^* in the Allen-Dynes formula; 0.12 is a typical value, but values in the range 0.1 - 0.15 are reasonable), it does indicate that the superconductivity can be readily explained in an electron-phonon framework.

9.4 Conclusions

To summarize, we report full potential calculations of the electronic structure, phonon dispersions of $LaNiC_2$ and electron-phonon coupling in $LaNiC_2$. We find that conventional electron-phonon coupling picture readily describes the superconductivity of $LaNiC_2$. With inversion center this would yield a pure s-wave state. However, because of the non-centrosymmetric structure of $LaNiC_2$ a small p admixture will be present. The Ni d states are located mainly away from the Fermi energy, and accordingly we do not find $LaNiC_2$ to be near magnetism. Therefore, we expect the contribution of spin fluctuations to the coupling, which is pair breaking for s-wave, to be small. The phonon-mediated Cooper pairs are intermediately coupled with large contributions made by two low frequency C non-bond-stretching modes, one of which has Kohn anomalies. Owing to the lack of inversion symmetry, the pairing will have dominant s-wave character with some mixture of p-wave. This is expected to give exponential decay of specific heat below T_C. In particular, there will be no line nodes in the gap function. Also, while the Cooper pairs also have some p-wave character, a pure electron phonon

mechanism will not yield breaking of time reversal symmetry due to the removal of centrosymmetry.

Chapter 10

Summary

In this dissertation, I have presented various studies that help to illuminate the role that structure and chemical composition play in defining the physical properties of materials, including ferroelectricity, magnetism and superconductivity. I used first principles methods based on density functional theory in my investigations. These methods enable us to see how electrons are arranged in real, momentum and spin spaces, and thus give us a microscopic basis to explain various properties of solids. I used this framework in the study of following illustrative examples.

The Zintl phase hydrides $SrAl_2H_2$, $BaGa_2H_2$, $SrGa_2H_2$ and SrAlSiH, where I find Ba and Sr are cationic while H is anionic. I also find the formation of covalent sp^2 bonds in the Al/Ga/Al-Si planes, which is a highly unusual bonding configuration for these elements.

PbTe, despite its simple and high symmetry rock salt structure, has a low thermal conductivity of 2.3 W/(m K). I studied the lattice dynamics of PbTe at various lattice parameters and found strong coupling between longitudinal acoustic and transverse optic modes that may explain its low thermal conductivity.

The double perovskites $BiPbZnNbO_6$ and $BiSrZnNbO_6$, where introducing size disorder at A-site prevents the BO_6 octahedra from tiling and enhances the polar

behavior. I find the polarization of Pb and Sr materials are 85 and 79 $\mu C/cm^2$, respectively, along the rhombohedral direction.

The unconventional superconductor FeSe, which shares the salient electronic and magnetic properties of other Fe superconductors and cannot be described as a conventional electron-phonon superconductor. This suggest Fe layer drives much of the physics in these compounds.

$NbFe_2$, which has a magnetic quantum critical point at or very close to the stoichiometric composition. I find that the magnetism is itinerant in the sense that the moments are highly dependent on ordering and go to zero for some configurations. I also find strong competition between different magnetic orderings that may explain its unusual non-Fermi liquid behavior at very low temperatures.

The Ni analogues of Fe superconductors LaNiPO and $BaNi_2As_2$, which have large Fermi surfaces without nesting and are further from magnetism. The superconductivity in Ni compounds are readily explained by the conventional electron-phonon picture, in contrast to the Fe superconductors.

Noncentrosymmetric $LaNiC_2$, which is a conventional electron-phonon superconductor with intermediate coupling. I find there are large contributions to the coupling by two low frequency C nonbond-stretching modes, one of which has strong Kohn anomalies.

Bibliography

Bibliography

[1] P. Hohenberg and W. Kohn, Phys. Rev. **136**, B864 (1964). 3, 8

[2] W. Kohn and L. Sham, Phys. Rev. **140**, A1133 (1965). 3, 9

[3] F. Gingl, T. Vogt, and E. Akiba, Journal of Alloys and Compounds **306**, 127 (2000). 4, 16, 18

[4] T. Bjorling, D. Noreus, K. Jansson, M. Andersson, E. Leonova, M. Edén, U. Hålenius, and U. Häussermann, Angew. Chem., Int. Ed. **44**, 7269 (2005). 4, 16, 18, 19

[5] T. Bjorling, D. Noreus, and U. Häussermann, J. Am. Chem. Soc. **128**, 817 (2006). 4, 16, 18

[6] A. F. Joffe, Can. J. Phys. **34**, 1342 (1956). 5, 37

[7] S. K. W. D. G. Cahilland and R. O. Pohl, Phys. Rev. B **46**, 6131 (1992). 5, 36

[8] D. J. Singh and C. H. Park, Phys. Rev. Lett. **100**, 087601 (2008). 5, 45, 49

[9] D. Fu, M. Itoh, S. Y. Koshihara, T. Kosugi, and S. Tsuneyuki, Phys. Rev. Lett. **100**, 227601 (2008). 5, 46

[10] Y. Kamihara, T. Watanabe, M. Hirano, and H. Hosono, J. Am. Chem. Soc. **130**, 3296 (2008). 5, 63, 75, 89, 90

[11] M. Rotter, M. Tegel, D. Johrendt, I. Schellenberg, W. Hermes, and R. Pottgen, Phys. Rev. B **78**, 020503(R) (2008). 5, 63, 90

[12] F. C. Hsu, J. Y. Luo, K. W. Yeh, T. K. Chen, T. W. Huang, P. M. Wu, Y. C. Lee, Y. L. Huang, Y. Y. Chu, D. C. Yan, and M. K. Wu, Proc. Natl. Acad. Sci. U.S.A. **105**, 14262 (2008). 5, 62, 64, 90

[13] Y. Yamada and A. Sakata, J. Phys. Soc. Jpn. **57**, 46 (1988). 6, 76

[14] M. Crook and R. Cywinski, J. Magn. Magn. Mater. **140-144**, 71 (1995). 6, 77

[15] T. Watanabe, H. Yanagi, T. Kamiya, Y. Kamihara, H. Hiramatsu, M. Hirano, and H. Hosono, Inorg. Chem. **46**, 7719 (2007). 6, 90, 91, 97

[16] O. I. Bodak and E. P. Marusin, Dopov. Akad. Nauk. Ukr. RSR, Ser. A: Fiz.-Mat. Tekh. Nauki **41**, 1048 (1979). 6, 103, 106

[17] W. H. Lee, H. K. Zeng, Y. D. Yao, and Y. Y. Chen, Physica C **266**, 138 (1996). 6, 104, 112

[18] V. K. Pecharsky, L. L. Miller, and K. A. Gschneidner, Phys. Rev. B **58**, 497 (1998). 6, 104, 112

[19] D. J. Singh and L. Nordstrom, *Planewaves, Pseudopotentials and the LAPW Method*, 2nd ed. (Springer, Berlin, 2006). 10, 17, 37, 49, 63, 77, 91, 106

[20] S. Baroni, S. de Gironcoli, A. D. Corso, and P. Giannozzi, Rev. Mod. Phys. **73**, 515 (2001). 11, 17

[21] S. Y. Savrasov and D. Y. Savrasov, Phys. Rev. B **54**, 16487 (1996). 11

[22] P. B. Allen and R. C. Dynes, Phys. Rev. B **12**, 905 (1975). 12

[23] D. M. Ceperley and B. J. Alder, Phys. Rev. Lett. **45**, 566 (1980). 13

[24] L. Pauling, *The Nature of the Chemical Bond and the Structure of Molecules and Crystals: An Introduction to Modern Structural Chemistry*, 3rd ed. (Cornell University Press, Ithaca, 1960). 15, 19

[25] C. E. Messer, J. Solid State Chem. **2**, 144 (1970). 16

[26] K. Yvon, Chimia **52**, 613 (1998). 16

[27] D. F. C. Morris and G. L. Reed, J. Inorg. Nucl. Chem. **27**, 1715 (1965). 16

[28] L. Pauling, Acta Cryst. A **32**, 751 (1976). 16

[29] J. P. Perdew, K. Burke, and M. Ernzerhof, Phys. Rev. Lett. **77**, 3865 (1996). 16, 38, 64, 92, 106

[30] P. Blaha, K. Schwarz, G. Madsen, D. Kvasnicka, and J. Luitz, http://www.wien2k.at. 17, 106

[31] S. Baroni, A. dal Corso, S. de Gironcoli, P. Giannozzi, C. Cavazzoni, G. Ballabio, S. Scandolo, G. Chiarotti, P. Focher, A. Pasquarello, K. Laasonen, A. Trave, R. Car, N. Marzari, and A. Kokalj, http://www.quantum-espresso.org. 17, 37, 50, 64, 92, 106

[32] D. Vanderbilt, http://www.physics.rutgers.edu/~dhv/uspp. 17

[33] A. J. Maeland and G. G. Libowitz, J. Less-Common Met. **89**, 197 (1983). 18

[34] A. J. Maeland, J. Less-Common Met. **89**, 183 (1983). 18

[35] A. F. Andresen, K. Otnes, and A. J. Maeland, J. Less-Common Met. **89**, 201 (1983). 18

[36] D. J. Singh and M. Gupta, Phys. Rev. B **76**, 075120 (2007). 18

[37] M. H. Lee, O. F. Sankey, T. Bjorling, D. Moser, D. Noreus, S. F. Parker, and U. Häussermann, Inorg. Chem. **46**, 6987 (2007). 19, 32

[38] R. Yu and P. K. Lam, Phys. Rev. B **37**, 8730 (1988). 20

[39] A. B. Kunz and D. J. Mickish, Phys. Rev. B **11**, 1700 (1975). 20

[40] R. Dovesi, C. Ermondi, E. Ferrero, C. Pisani, and C. Roetti, Phys. Rev. B **29**, 3591 (1984). 20

[41] R. E. Watson, Phys. Rev. **111**, 1108 (1958). 20

[42] I. I. Mazin and D. A. Papaconstantopoulos, Phys. Rev. B **69**, 180512(R) (2004). 21

[43] G. Q. Huang, L. F. Chen, M. Liu, and D. Y. Xing, Phys. Rev. B **69**, 064509 (2004). 21

[44] G. Q. Huang, L. F. Chen, M. Liu, and D. Y. Xing, Phys. Rev. B **71**, 172506 (2005). 21

[45] V. Ozolins, E. H. Majzoub, and T. J. Udovic, Journal of Alloys and Compounds **375**, 1 (2004). 26

[46] A. Aguayo and D. J. Singh, Phys. Rev. B **69**, 155103 (2004). 26

[47] D. J. Singh, Phys. Rev. B **71**, 216101 (2005). 26

[48] E. Orgaz and A. Aburto, Int. J. Quantum Chem. **101**, 783 (2005). 28

[49] G. Herzberg, *Molecular Spectra and Moleculer Structure III, Electronic Spectra and Electronic Structure of Polyatomic Molecules* (Krieger, Malabar, FL, 1991). 29

[50] J. L. Verble, J. L. Warren, and J. L. Yarnell, Phys. Rev. **168**, 980 (1968). 29

[51] N. Ohba, K. Miwa, T. Noritake, and A. Fukumoto, Phys. Rev. B **70**, 035102 (2004). 29

[52] W. Zhong, R. D. King-Smith, and D. Vanderbilt, Phys. Rev. Lett. **72**, 3618 (1994). 34, 45, 56

[53] A. Ioffe, *Semiconductor Thermoelements and Thermoelectric Cooling* (Infosearch, London, 1957). 36

[54] D. Rowe, *CRC Handbook of Thermoelectrics* (CRC Press, Boca Raton, LA, 1995). 36

[55] G. Slack, in *Solid State Physics*, Vol. 34, edited by F. Seitz and D. Turnbull (Academic Press, New York, NY, 1979). 36

[56] C. Wood, Rep. Prog. Phys. **51**, 459 (1988). 37

[57] Y. Gelbstein, Z. Dashevsky, and M. P. Daniel, Physica B **363**, 196 (2005). 37

[58] K. Hsu, S. Loo, F. Guo, W. Chen, J. S. Dyck, C. Uher, T. Hogan, E. K. Polychroniadis, and M. G. Kanatzidis, Science **303**, 818 (2004). 37

[59] T. C. Harman, P. J. Taylor, M. P. Walsh, and B. E. LaForge, Science **297**, 2229 (2002). 37

[60] J. J. B. Conklin, L. E. Johnson, and J. G. W. Pratt, Phys. Rev. **137**, A1282 (1965). 37

[61] K. M. Rabe and J. D. Joannopoulos, Phys. Rev. B **32**, 2302 (1985). 37

[62] U. V. Waghmare, N. A. Spaldin, H. C. Kandpal, and R. Seshadri, Phys. Rev. B **67**, 125111 (2003). 37

[63] D. I. Bilc, S. D. Mahanti, and M. G. Kanatzidis, Phys. Rev. B **74**, 125202 (2006). 37

[64] K. Hoang, S. D. Mahanti, and P. Jena, Phys. Rev. B **76**, 115432 (2007). 37

[65] R. Dalven, Infrared Phys. **9**, 141 (1969). 38

[66] Y. Noda, K. Masumoto, S. Ohba, Y. Saito, K. Toriumi, Y. Iwata, and I. Shibuya, Acta. Cryst. C **43**, 1443 (1987). 38

[67] C. Filippi, D. J. Singh, and C. J. Umrigar, Phys. Rev. B **50**, 14947 (1994). 38

[68] D. J. Singh and L. L. Boyer, Ferroelectrics **136**, 95 (1992). 38, 41, 52

[69] M. IIzumi, Y. Hamaguchi, K. F. Komatsubara, and Y. Kato, J. Phys. Soc. Jpn. **38**, 443 (1975). 38

[70] G. S. Pawley, W. Cochran, R. A. Cowley, and G. Dolling, Phys. Rev. Lett. **17**, 753 (1966). 38, 41

[71] G. Lucovsky, R. P. Martin, and E. Burstein, J. Nonmetals **1**, 173 (1973). 38

[72] K. M. Rabe and J. D. Joannopoulos, Phys. Rev. Lett. **59**, 570 (1987). 38

[73] K. M. Rabe and J. D. Joannopoulos, Phys. Rev. B **36**, 3319 (1987). 38

[74] K. M. Rabe and J. D. Joannopoulos, Phys. Rev. B **36**, 6631 (1987). 38

[75] A. Bussmann-Holder, Phys. Rev. B **40**, 11639 (1989). 41

[76] H. Burkhard, G. Bauer, and A. Lopez-Otero, J. opt. Soc. Am. **67**, 943 (1977). 41

[77] G. Samara, Phys. Rev. B **1**, 3777 (1970). 41

[78] M. Fornari and D. J. Singh, Phys. Rev. B **63**, 092101 (2001). 41, 49

[79] Y. Matsushita, H. Bluhm, T. H. Geballe, and I. R. Fisher, Phys. Rev. Lett. **94**, 157002 (2005). 43

[80] Y. Matsushita, H. Bluhm, T. H. Geballe, and I. R. Fisher, Phys. Rev. B **74**, 134512 (2006). 43

[81] V. M. Goldschmidt, Skr. Nor. Vidensk.-Akad., [Kl.] 1: Mat.-Naturvidensk. Kl. **K1**, 8 (1926). 45

[82] R. D. Shannon, Acta Crystallogr., Sect. A: Cryst. Phys., Diffr., Theor. Gen. Crystallogr. **32**, 751 (1976). 45, 47

[83] W. Zhong and D. Vanderbilt, Phys. Rev. Lett. **74**, 2587 (1995). 45

[84] R. E. Cohen, Nature **358**, 136 (1992). 45, 56

[85] S. M. Choi, C. J. Stringer, T. R. Shrout, and C. A. Randall, J. Appl. Phys. **98**, 034108 (2005). 45

[86] S. V. Halilov, M. Fornari, and D. J. Singh, Appl. Phys. Lett. **81**, 3443 (2002). 45, 47

[87] D. I. Bilc and D. J. Singh, Phys. Rev. Lett. **96**, 147602 (2006). 45, 47

[88] D. J. Singh, M. Ghita, M. Fornari, and S. V. Halilov, Ferroelectrics **338**, 73 (2006). 45

[89] W. Liu and X. Ren, Phys. Rev. Lett. **103**, 257602 (2009). 46

[90] B. Noheda, D. E. Cox, G. Shirane, S. E. Park, L. E. Cross, and Z. Zhong, Phys. Rev. Lett. **86**, 3891 (2001). 46

[91] H. Fu and R. E. Cohen, Nature **403**, 281 (2000). 46

[92] S. E. Park and T. R. Shrout, J. Appl. Phys. **82**, 1804 (1997). 46

[93] J. B. Neaton, C. Ederer, U. V. Waghmare, N. A. Spaldin, and K. M. Rabe, Phys. Rev. B **71**, 014113 (2005). 46, 57

[94] R. E. Eitel, C. A. Randall, T. R. Shrout, P. W. Rehrig, W. Hackenberger, and S. E. Park, Jpn. J. Appl. Phys. **40**, 5999 (2001). 46

[95] C. J. Stringer, R. E. Eitel, T. R. Shrout, C. A. Randall, and I. M. Reaney, J. Appl. Phys. **97**, 024101 (2005). 46

[96] M. R. Suchomel and P. K. Davis, J. Appl. Phys. **96**, 4405 (2004). 46

[97] C. A. Randall, R. Eitel, B. Jones, T. R. Shrout, D. I. Woodward, and I. M. Reaney, J. Appl. Phys. **95**, 3633 (2004). 46

[98] J.-R. Cheng, W. Zhu, N. Li, and L. E. Cross, Mater. Lett. **57**, 2090 (2003). 46

[99] R. Duan, R. F. Speyer, E. Alberta, and T. R. Shrout, J. Mater. Res. **19**, 2185 (2004). 46

[100] M. R. Suchomel and P. K. Davies, Appl. Phys. Lett. **86**, 262905 (2005). 47

[101] D. Y. Suarez-Sandoval and P. K. Davies, Appl. Phys. Lett. **82**, 3215 (2003). 47

[102] J. Chen, X. R. Xing, and G. R. Liu, Appl. Phys. Lett. **87**, 231915 (2005). 47

[103] M. Ghita, M. Fornari, D. J. Singh, and S. V. Halilov, Phys. Rev. B **72**, 054114 (2005). 47, 49, 52

[104] V. V. Bogatko and Y. N. Venevtsev, Izv. Akad. Nauk SSSR, Neorg. Mater. **17**, 367 (1981). 48

[105] L. G. Kosyachenko, V. V. Kochetkov, A. G. Belous, V. V. Bogatko, and Y. N. Venevtsev, Izv. Akad. Nauk SSSR, Neorg. Mater. **18**, 1352 (1982). 48, 50

[106] H. B. Krause and D. L. Gibbon, Z. Kristallogr. **134**, 44 (1971). 48

[107] P. K. Davies and M. A. Akbas, J. Phys. Chem. Solids **61**, 159 (2000). 48

[108] S. A. Prosandeev, E. Cockayne, B. P. Burton, S. Kamba, J. Petzelt, Y. Yuzyuk, R. S. Katiyar, and S. B. Vakhrushev, Phys. Rev. B **70**, 134110 (2004). 48

[109] A. M. Glazer, Acta Crystallogr., Sect. B: Struct. Crystallogr. Cryst. Chem. **28**, 3384 (1972). 49

[110] D. J. Singh, Phys. Rev. B **43**, 6388 (1991). 50, 63

[111] R. D. King-Smith and D. Vanderbilt, Phys. Rev. B **47**, 651 (1993). 50

[112] R. Resta, Rev. Mod. Phys. **66**, 899 (1994). 50

[113] M. Suewattana and D. J. Singh, Phys. Rev. B **73**, 224105 (2006). 56

[114] D. J. Singh, Phys. Rev. B **53**, 176 (1996). 56

[115] I. Levin, T. G. Amos, J. C. Nino, T. A. Vanderah, C. A. Randall, and M. T. Lanagan, J. Solid State Chem. **168**, 69 (2002). 61

[116] A. N. Salak, A. D. Shilin, M. V. Bushinski, N. M. Olekhnovich, and N. P. Vyshatko, Mater. Res. Bull. **35**, 1429 (2000). 61

[117] A. A. Belik, T. Wuernisha, T. Kamiyama, K. Mori, M. Maie, T. Nagai, Y. Matsui, and E. Takayama-Muromachi, Chem. Mater. **18**, 133 (2006). 61

[118] Z. A. Ren, W. Lu, J. Yang, W. Yi, X. L. Shen, Z. C. Li, G. C. Che, X. L. Dong, L. L. Sun, F. Zhou, and Z. X. Zhao, Chin. Phys. Lett. **25**, 2215 (2008). 63

[119] Z. A. Ren, G. C. Che, X. L. Dong, J. Yang, W. Lu, W. Yi, X. L. Shen, Z. C. Li, L. L. Sun, F. Zhou, and Z. X. Zhao, Europhys. Lett. **83**, 17002 (2008). 63

[120] C. Wang, L. Li, S. Chi, Z. Zhu, Z. Ren, Y. Li, Y. Wang, X. Lin, Y. Luo, S. Jiang, X. Xu, G. Cao, and Z. Xu, Europhys. Lett. **83**, 67006 (2008). 63

[121] A. S. Sefat, M. A. McGuire, B. C. Sales, R. Jin, J. Y. Howe, and D. Mandrus, Phys. Rev. B **77**, 174503 (2008). 63

[122] H. Kito, H. Eisaki, and A. Iyo, J. Phys. Soc. Jpn. **77**, 063707 (2008). 63

[123] M. Rotter, M. Tegel, and D. Johrendt, Phys. Rev. Lett. **101**, 107006 (2008). 63, 90

[124] X. C. Wang, Q. Q. Liu, Y. X. Lv, W. B. Gao, L. X. Yang, R. C. Yu, F. Y. Li, and C. Q. Jin, Solid State Commun. **148**, 538 (2008). 63

[125] D. J. Singh and M. H. Du, Phys. Rev. Lett. **100**, 237003 (2008). 63, 64, 69, 71, 90, 95

[126] C. de la Cruz, Q. Huang, J. W. Lynn, J. Li, W. R. II, J. L. Zaretsky, H. A. Mook, G. F. Chen, J. L. Luo, N. L. Wang, and P. Dai, Nature **443**, 899 (2008). 63, 70, 90

[127] W. Bao, Y. Qiu, Q. Huang, M. A. Green, P. Zajdel, M. R. Fitzsimmons, M. Zhernenkov, S. Chang, M. Fang, B. Qian, E. K. Vehstedt, J. Yang, H. M. Pham, L. Spinu, and Z. Q. Mao, Phys. Rev. Lett. **102**, 247001 (2009). 63, 71

[128] F. Ma, W. Ji, J. Hu, Z. Y. Luu, and T. Xiang, Phys. Rev. Lett. **102**, 177003 (2009). 63, 71

[129] I. Mazin, D. J. Singh, M. D. Johannes, and M. H. Du, Phys. Rev. Lett. **101**, 057003 (2008). 64, 67, 70, 73, 75, 90, 92, 97

[130] D. J. Singh, Phys. Rev. B **78**, 094511 (2008). 64

[131] A. R. Lennie, S. A. T. Redfern, P. F. Schofield, and D. J. Vaughan, Mineralogical Magazine **59**, 677 (1995). 64, 72

[132] D. M. Finlayson, D. Greig, J. P. Llewellyn, and T. Smith, Proc. Phys. Soc. B **69**, 860 (1956). 64

[133] L. Boeri, O. V. Dolgov, and A. A. Golubov, Phys. Rev. Lett. **101**, 026403 (2008). 67, 90, 92, 97, 102

[134] J. Dong, H. J. Zhang, G. Xu, Z. Li, G. Li, W. Z. Hu, D. Wu, G. F. Chen, X. Dai, J. L. Luo, Z. Fang, and N. Wang, Europhys. Lett. **83**, 27006 (2008). 70

[135] G. F. Chen, Z. Li, D. Wu, G. Li, W. Z. Hu, J. Dong, P. Zheng, J. L. Luo, and N. L. Wang, Phys. Rev. Lett. **100**, 247002 (2008). 70, 90

[136] J. Zhao, Q. Huang, C. de la Cruz, S. Li, J. Lynn, Y. Chen, M. Green, G. Chen, G. Li, Z. Li, J. Luo, N. Wang, and P. Dai, Nature Materials **7**, 953 (2008). 70

[137] Q. Huang, Y. Qiu, W. Bao, J. Lynn, M. Green, Y. Gasparovic, T. Wu, G. Wu, and X. Chen, Phys. Rev. Lett. **101**, 257003 (2008). 70

[138] A. I. Goldman, D. N. Argyriou, B. Ouladdiaf, T. Chatterji, A. Kreyssig, S. Nandi, N. Ni, S. L. Budko, P. C. Canfield, and R. McQueeney, Phys. Rev. B **78**, 100506(R) (2008). 70

[139] Y. Nakai, K. Ishida, Y. Kamihara, M. Hirano, and H. Hosono, J. Phys. Soc. Japan **77**, 073701 (2008). 70

[140] T. Yildirim, Phys. Rev. Lett. **101**, 057010 (2008). 70, 72

[141] S. Ishibashi, K. Terakura, and H. Hosono, J. Phys. Soc. Japan **77**, 053709 (2008). 70, 72

[142] Z. P. Yin, S. Lebegue, M. J. Han, B. Neal, S. Y. Savrasov, and W. E. Pickett, Phys. Rev. Lett. **101**, 047001 (2008). 70, 72, 91, 92

[143] I. I. Mazin, M. D. Johannes, L. Boeri, K. Koepernik, and D. J. Singh, Phys. Rev. B **78**, 085104 (2008). 70, 72, 87, 91, 92

[144] V. Vildosola, L. Pourovskii, R. Arita, S. Biermann, and A. Georges, Phys. Rev. B **78**, 064518 (2008). 70

[145] T. Yildirim, Phys. Rev. Lett. **102**, 037003 (2009). 70, 72

[146] M. A. McGuire, A. D. Christianson, A. S. Sefat, B. C. Sales, M. D. Lumsden, R. Jin, E. A. Payzant, D. Mandrus, Y. Luan, V. Keppens, V. Varadarajan, J. W. Brill, R. P. Hermann, M. T. Sougrati, F. Grandjean, , and G. J. Long, Phys. Rev. B **78**, 094517 (2008). 72

[147] F. Bondino, E. Magnano, M. Malvestuto, F. Parmigiani, M. A. McGuire, A. S. Sefat, B. C. Sales, R. Jin, D. Mandrus, E. W. Plummer, D. J. Singh, and N. Mannella, Phys. Rev. Lett. **101**, 267001 (2008). 72

[148] T. Moriya and K. Ueda, Rep. Prog. Phys. **66**, 1299 (2003). 73

[149] P. Monthoux and G. G. Lonzarich, Phys. Rev. B **63**, 054529 (2001). 73

[150] K. Kuroki, S. Onari, R. Arita, H. Usui, Y. Tanaka, H. Kotani, and H. Aoki, Phys. Rev. Lett. **101**, 087004 (2008). 73

[151] R. Laughlin, G. G. Lonzarich, P. Monthoux, and D. Pines, Adv. Phys. **50**, 361 (2001). 75

[152] M. V. Nevitt, C. W. Kimball, and R. S. Preston, *Proc. Int. Conf. Magnetism, Nottingham* (The Institute of Physics and The Physical Society, London, 1964) p. 137. 75

[153] Y. Yamada, Y. Kitaoka, K. Asayama, and A. Sakata, J. Phys. Soc. Jpn. **53**, 3198 (1984). 75

[154] H. Wada, M. Hada, M. Chic, and Y. Nakamura, J. Phys. Soc. Jpn. **59**, 701 (1990). 76

[155] M. Brando, D. Moroni-Klementowicz, C. Albrecht, and F. M. Grosche, Physica B **378-380**, 111 (2006). 76, 77

[156] M. Brando, D. Moroni-Klementowicz, C. Albrecht, W. Duncan, D. Gruner, R. Boll, B. Fak, and F. M. Grosche, J. Magn. Magn. Mater. **310**, 852 (2007). 76

[157] M. Brando, W. J. Duncan, D. Moroni-Klementowicz, C. Albrecht, D. Gruner, R. Ballou, and F. M. Grosche, Phys. Rev. Lett. **101**, 026401 (2008). 76

[158] D. Moroni-Klementowicz, M. Brando, C. Albrecht, W. J. Duncan, F. M. Grosche, D. Gruner, and G. Kreiner, Phys. Rev. B **79**, 224410 (2009). 76, 77

[159] J. F. van Acker, Z. M. Stadnik, J. C. Fuggle, H. J. W. M. Hoekstra, K. H. J. Buschow, and G. Stroink, Phys. Rev. B **37**, 6827 (1988). 76

[160] F. Bondino, E. Magnano, M. Malvestuto, F. Parmigiani, M. A. McGuire, A. S. Sefat, B. C. Sales, R. Jin, D. Mandrus, E. W. Plummer, D. J. Singh, and N. Mannella, Phys. Rev. Lett. **101**, 267001 (2008). 76

[161] P. J. Brown, J. Deportes, and B. Ouladdiaf, J. Phys.: Condens. Matter **4**, 10015 (1992). 76, 85

[162] E. Hoffmann, P. Entel, E. Wassermann, K. Schwarz, and P. Mohn, J. Phys. IV **5**, C2 (1995). 76

[163] J. Koble and M. Huth, Phys. Rev. B **66**, 144414 (2002). 76

[164] S. Ishida, S. Asano, and J. Ishida, J. Phys. Soc. Jpn. **54**, 4695 (1985). 77

[165] Y. Yamada, H. Nakamura, Y. Toke, K. Asayama, K. Koga, A. Kati, and T. Murakami, J. Phys. Soc. Jpn. **59**, 2976 (1990). 77

[166] M. Kurisu, Y. Andoh, and Y. Yamada, Physica B **237-238**, 493 (1997). 77

[167] M. R. Crook and R. Cywinski, Hyperfine Interact. **85**, 203 (1994). 77

[168] B. S. Bokshtein, N. P. D'Yakonova, G. S. Nikol'skii, and Y. D. Yagodkin, Russ. J. Phys. Chem. **51**, 1273 (1977). 78

[169] I. Mazin and D. Singh, Phys. Rev. B **69**, 020402(R) (2004). 78, 87

[170] A. Aguayo, I. I. Mazin, and D. J. Singh, Phys. Rev. Lett. **92**, 147201 (2004). 78, 87

[171] S. Ishida, S. Asano, and J. Ishida, J. Phys. Soc. Jpn. **54**, 3925 (1985). 81, 82

[172] K. Terao and M. Shimizu, Phys. Status Solidi B **139**, 485 (1987). 81

[173] N. Takayama and M. Shimizu, J. Phys. F: Met. Phys. **18**, L83 (1988). 81

[174] J. Inoue and M. Shimizu, J. Magn. Magn. Mater. **79**, 265 (1989). 81

[175] E. C. Stoner, Proc. R. Soc. London **169**, 339 (1939). 81

[176] O. K. Andersen, J. Madsen, U. K. Poulsen, O. Jepsen, and J. Kollar, Physica B & C **86-88**, 249 (1977). 81

[177] U. K. Poulsen, J. Kollar, and O. K. Andersen, J. Phys. F: Met. Phys. **6**, L241 (1976). 81

[178] S. Asano and S. Ishida, J. Phys.: Condens. Matter **1**, 8501 (1989). 82

[179] T. Moriya, *Spin Fluctuations in Itinerant Electron Magnetism* (Springer, Berlin, 1985). 87

[180] A. Z. Solontsov and D. Wagner, Phys. Rev. B **51**, 12410 (1995). 87

[181] A. Ishigaki and T. Moriya, J. Phys. Soc. Jpn. **67**, 3924 (1998). 87

[182] P. Larson, I. I. Mazin, and D. J. Singh, Phys. Rev. B **69**, 064429 (2004). 87

[183] G. F. Chen, Z. Li, G. Li, J. Zhou, D. Wu, J. Dong, W. Z. Hu, P. Zheng, Z. J. Chen, H. Q. Yuan, J. Singleton, J. L. Luo, and N. L. Wang, Phys. Rev. Lett. **101**, 057007 (2008). 90

[184] X. Zhu, H. Yang, L. Fang, G. Mu, and H. H. Wen, Supercond. Sci. Technol. **21**, 105001 (2008). 90

[185] X.C.Wang, Q. Liu, Y. Lv, W. Gao, L.X.Yang, R.C.Yu, F.Y.Li, and C. Jin, Solid State Commun. **148**, 538 (2008). 90

[186] Q. Huang, J. Zhao, J. W. Lynn, G. F. Chen, J. L. Luo, N. L. Wang, and P. Dai, Phys. Rev. B **78**, 054529 (2008). 90

[187] I. I. Mazin and M. D. Johannes, Nat. Phys. **5**, 141 (2009). 90, 92

[188] H. Chen, Y. Ren, Y. Qiu, W. Bao, R. H. Liu, G. Wu, T. Wu, Y. L. Xie, X. F. Wang, Q. Huang, and X. H. Chen, Europhys. Lett. **85**, 17006 (2009). 90

[189] A. J. Drew, C. Niedermayer, P. J. Baker, F. L. Pratt, S. J. Blundell, R. H. Lancaster, R. H. Liu, G. Wu, X. H. Chen, I. Watanabe, V. K. Malik, A. Dubroka, M. Roessle, K. W. Kim, C. Baines, and C. Bernhard, Nat. Mat. **8**, 310 (2009). 90

[190] J. Q. Yan, A. Kreyssig, S. Nandi, N. Ni, S. L. Budko, A. Kracher, R. J. McQueeney, R. W. McCallum, T. A. Lograsso, A. I. Goldman, and P. C. Canfield, Phys. Rev. B **78**, 024516 (2008). 90

[191] M. Tegel, D. Bichler, and D. Jorendt, Solid State Sciences **10**, 193 (2008). 90, 91, 97

[192] Z. Li, G. F. Chen, J. Dong, G. Li, W. Z. Hu, D. Wu, S. K. Su, P. Zheng, T. Xiang, N. L. Wang, and J. L. Luo, Phys. Rev. B **78**, 060504(R) (2008). 90

[193] L. Fang, H. Yang, P. Cheng, X. Zhu, G. Mu, and H. H. Wen, Phys. Rev. B **78**, 104528 (2008). 90

[194] V. L. Kozhevnikov, O. N. Leonidova, A. L. Ivanovskii, I. R. Shein, B. N. Goshchitskii, and A. E. Karkin(2008), cond-mat/0804.4546. 90

[195] F. Ronning, N. Kurita, E. D. Bauer, B. L. Scott, T. Park, T. Klimczuk, R. Movshovich, and J. D. Thompson, J. Phys.: Condens. Matter **20**, 342203 (2008). 90, 92, 102

[196] W. B. Zhang, X. B. Xiao, W. Li, W. Y. Yu, N. Wang, and B. Y. Tang, Phys. Rev. B **77**, 214513 (2008). 91

[197] I. A. Nekrasov, Z. V. Pchelkina, and M. V. Sadovskii, JETP Lett. **88**, 144 (2008). 91, 101

[198] F. Ma, Z. Y. Lu, and T. Xiang, Front. Phys. China **5**, 150 (2010). 91, 101

[199] D. J. Singh, Phys. Rev. B **78**, 094511 (2008). 91, 92, 101

[200] A. Subedi, D. J. Singh, and M. H. Du, Phys. Rev. B **78**, 060506 (2008). 102

[201] P. Kotsanidis and J. K. Yakinthos, J. Less-Common Met. **152**, 287 (1989). 103

[202] H. Onodera, Y. Koshikawa, M. Kosaka, M. Ohashi, H. Yamauchi, and Y. Yamaguchi, J. Magn. Magn. Mater. **182**, 161 (1998). 103

[203] J. Bardeen, L. N. Cooper, and J. R. Schrieffer, Phys. Rev. **108**, 1175 (1957). 104

[204] M. Sigrist and K. Ueda, Rev. Mod. Phys. **63**, 239 (1991). 104

[205] A. D. Hillier, J. Quintanilla, and R. Cywinski, Phys. Rev. Lett. **102**, 117007 (2009). 104

[206] E. Bauer, G. Hilscher, H. Michor, C. Paul, E. W. Scheidt, A. Gribanov, Y. Seropegin, H. Noel, M. Sigrist, and P. Rogl, Phys. Rev. Lett. **92**, 027003 (2004). 104, 105

[207] N. Kimura, K. Ito, K. Saitoh, Y. Umeda, H. Aoki, and T. Terashima, Phys. Rev. Lett. **95**, 247004 (2005). 104

[208] I. Sugitani, Y. Okuda, H. Shishido, T. Yamada, A. Thamizhavel, E. Yamamoto, T. D. Matsuda, Y. Haga, T. Takeuchi, R. Settai, and Y. Onuki, J. Phys. Soc. Jpn. **75**, 043703 (2006). 104

[209] K. Togano, P. Badica, Y. Nakamori, S. Orimo, H. Takeya, and K. Hirata, Phys. Rev. Lett. **93**, 247004 (2004). 104

[210] T. Akazawa, H. Hidaka, T. Fujiwara, T. C. Kobayashi, E. Yamamoto, Y. Haga, R. Settai, and Y. Onuki, J. Phys.: Condens. Matter **16**, L29 (2004). 104

[211] R. D. Blaugher and J. K. Hulm, J. Phys. Chem. Solids **19**, 134 (1961). 104

[212] G. Amano, S. Akutagawa, T. Muranaka, Y. Zenitani, and J. Akimitsu, J. Phys. Soc. Jpn. **73**, 530 (2004). 104, 105

[213] Y. Yanase and M. Sigrist, J. Phys. Soc. Jpn. **76**, 043712 (2007). 104

[214] D. J. Singh and I. I. Mazin, Phys. Rev. B **70**, 052504 (2004). 105, 106

[215] Y. L. Zuev, V. A. Kuznetsova, R. Prozorov, M. D. Vannette, M. V. Lobanov, D. K. Christen, and J. R. Thompson, Phys. Rev. B **76**, 132508 (2007). 105

[216] H. Mukuda, S. Nishide, A. Harada, K. Iwasaki, M. Yogi, M. Yashima, Y. Kitaoka, M. Tsujino, T. Takeuchi, R. Settai, Y. Onuki, E. Bauer, K. M. Itoh, and E. E. Haller, J. Phys. Soc. Jpn. **78**, 014705 (2009). 105

[217] S. Lee, W. Jeitschko, and R.-D. Hoffmann, Inorg. Chem. **28**, 4094 (1989). 106

[218] T. Gulden, R. W. Henn, O. Jepsen, R. K. Kremer, W. Schnelle, A. Simon, and C. Felser, Phys. Rev. B **56**, 9021 (1997). 106

[219] J. Laverock, T. D. Haynes, C. Utfeld, and S. B. Dugdale, Phys. Rev. B **80**, 125111 (2009). 107

[220] W. E. Pickett and D. J. Singh, Phys. Rev. Lett. **72**, 3702 (1994). 109

Appendix

Appendix A

List of Publications

- *Polar behavior of the double perovskite $BiMZnNbO_6$ (M=Pb and Sr) from density-functional calculations*, S. Takagi, A. Subedi, D.J. Singh, and V.R. Cooper, Phys. Rev. B **81**, 134106 (2010).

- *Temperature and pressure dependence of the Fe-specific phonon density of states in $Ba(Fe_{1-x}Co_x)_2As_2$*, O. Delaire, M.S. Lucas, A.M. dos Santos, A. Subedi, A.S. Sefat, M.A. McGuire, L. Mauger, J.A. Munoz, C.A. Tulk, Y. Xiao, M. Somayazulu, J.Y. Zhao, W. Sturhahn, E.E. Alp, D.J. Singh, B.C. Sales, D. Mandrus, and T. Egami, Phys. Rev. B **81**, 094504 (2010).

- *Band structure and itinerant magnetism in quantum critical $NbFe_2$*, A. Subedi and D.J. Singh, Phys. Rev. B. **81**, 024422 (2010). Erratum: Phys. Rev. B **81**, 059902(E) (2010).

- *Phonons in doped and undoped $BaFe_2As_2$ investigated by inelastic x-ray scattering*, M.S. Lucas, A.M. dos Santos, A. Subedi, A.S. Sefat, M.A. McGuire, L. Mauger, J.A. Munoz, C.A. Tulk, Y. Xiao, M. Somayazulu, J.Y. Zhao, W. Sturhahn, E.E. Alp, D.J. Singh, B.C. Sales, D. Mandrus, and T. Egami, Phys. Rev. B **80**, 214534 (2009).

- *Electron-phonon superconductivity in noncentrosymmetric $LaNiC_2$: first principles study*, A. Subedi and D.J. Singh, Phys. Rev B **80**, 092506 (2009).

- *Low-Temperature Magnetothermal Transport Investigation of a Ni-Based Superconductor $BaNi_2As_2$: Evidence for Fully Gapped Superconductivity*, N. Kurita, F. Ronning, Y. Tokiwa, E.D. Bauer, A. Subedi, D.J. Singh, J.D. Thompson, and R. Movshovich, Phys. Rev. Lett. **102**, 147004 (2009).

- *The performance of in situ grown Schottky-barrier single wall carbon nanotube field-effect transistors*, Z. Zhou, G. Eres, R. Jin, A. Subedi, D. Mandrus, and E.H. Kim, Nanotechnology **20**, 085709 (2009).

- *Possible superconductivity in Fe-Sb based materials: Density functional study of LiFeSb*, L. Zhang, A. Subedi, D.J. Singh, and M.-H. Du, Phys. Rev. B **78**, 174520 (2008).

- *Ab initio phonon dispersions for PbTe*, J. An, A. Subedi, and D.J. Singh, Solid State Communications **148**, 417 (2008).

- *Density functional study of FeS, FeSe, and FeTe: Electronic structure, magnetism, phonons, and superconductivity*, A. Subedi, L. Zhang, D.J. Singh, and M.-H. Du, Phys. Rev. B **78**, 134514 (2008).

- *Density functional study of $BaNi_2As_2$: Electronic structure, phonons and electron-phonon superconductivity*, A. Subedi and D.J. Singh, Phys. Rev. B **78**, 132511 (2008).

- *Electron-phonon superconductivity in LaNiPO*, A. Subedi, D.J. Singh, and M.-H. Du, Phys. Rev. B **78**, 045106 (2008).

- *Bonding in Zintl phase hydrides: Density functional calculations for SrAlSiH, $SrAl_2H_2$, $SrGa_2H_2$, and $BaGa_2H_2$*, A. Subedi and D.J. Singh, Phys. Rev. B **78**, 045106 (2008).

- *Structure and dynamics of perovskite hydrides $AMgH_3$ (A=Na, K, Rb) in relation to the corresponding fluorides: A first-principles study*, M. Fornari, A. Subedi, and D.J. Singh, Phys. Rev. B **76**, 214118 (2007).

- *Control of electron transport related defects in in situ fabricated single wall carbon nanotube devices*, Z. Zhou, R. Jin, G. Eres, A. Subedi, and D. Mandrus, Appl. Phys. Lett. **89**, 133124 (2006).

Vita

I was born in Biratnagar, a small city in the southeastern part of Nepal. My parents moved to Kathmandu when I was three years old and I grew up among the beautiful temples and arresting mountains in this very enchanting city. I came to the United States for undergraduate studies at DePauw University. This was made possible by generous financial aid by DePauw that covered the tuition and my living expenses. In May of 2006, I received Bachelor of Arts degree with majors in mathematics and physics. I then attended the graduate program in physics at the University of Tennessee at Knoxville in August of 2006. I did my research work at Oak Ridge National Laboratory with Dr. David J. Singh, which was supported by funds from the United States taxpayers. I received my Doctor of Philosophy degree in physics in August of 2010.